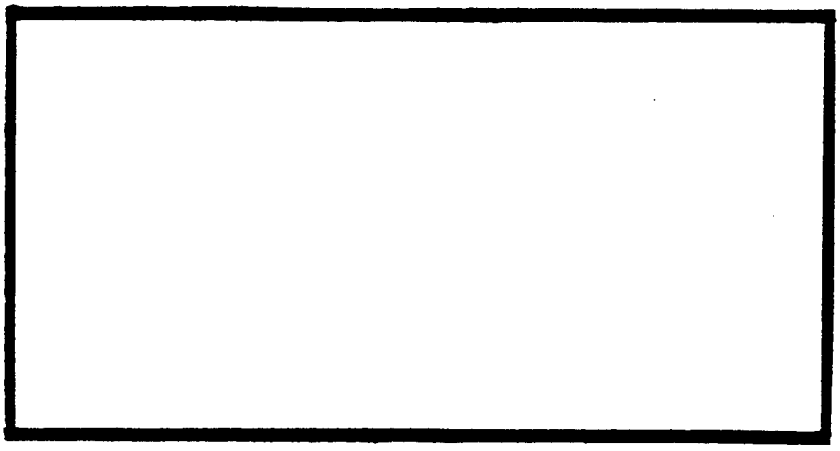

DEPARTMENT OF THE AIR FORCE

AIR UNIVERSITY

AIR FORCE INSTITUTE OF TECHNOLOGY

Wright-Patterson Air Force Base, Ohio

AFIT/GAE/ENY/98S-02.

Electro-Mechanical Fatigue Behavior of a Quasi-Isotropic Laminate with an Embedded Piezoelectric Actuator

Thesis

Tse-Lin Hsu B.S.M.E.
Major, Republic of China Army

AFIT/GAE/ENY/98S-02.

AFIT/GAE/ENY/98S-02

"The views expressed in this thesis are those of the author and do not reflect the official policy or position of the Department of Defense or the U.S. Government."

Approved for public release; distribution unlimited

AFIT/GAE/ENY/98S-02.

Electro-Mechanical Fatigue Behavior of a Quasi-Isotropic Laminate with an Embedded Piezoelectric Actuator

Thesis

Presented to the Faculty of the Graduate School of Engineering of the Air Force Institute of Technology Air University In Partial Fulfillment for the Degree of

Master of Science

Specialization in: Aeronautical Engineering

BY

Tse-Lin Hsu B.S.M.E.

Major, Republic of China Army

Air Force Institute of Technology

Wright-Patterson AFB, Ohio

1 September, 1998

Sponsored by AFOSR and Air Force Research Laboratory, WPAFB, OH

AFIT/GAE/ENY/98S-02.

Electro-Mechanical Fatigue Behavior of a Quasi-Isotropic Laminate with an Embedded Piezoelectric Actuator

Tse-Lin Hsu B.S.M.E.

Major, Republic of China Army

Approved:

Dr. Shankar Mall Committee Chairman	8/30/98 Date
Major Jeffrey S. Turcotte Committee member	9/1/98 Date
Captain Jeffrey Bons Committee member	9/1/98 Date

Acknowledgments

Several people provided expert guidance and support to me throughout this project, and, without their assistance, I could not have done it. First and foremost, I am very much obliged to my advisor, Dr. Shankar Mall for his kind advice and guidance and for pointing out the right direction. Further, I want to thank Maj Turcotte and Capt Bons for taking their precious time to serve on my graduate committee. The AFIT Aeronautical Engineering Laboratory staff was also instrumental in this project. Without the help of Mr. Charlie Mcneely, Mr. Jay Anderson, Mr. Dan Rioux, and Mr. Andy Pitts, this thesis would not have been completed. I also want to give my thanks to Mr. Ron Cornwell and Mr. Brian Rice for offering me excellent support in fabricating the specimens and their general technical expertise. In addition, I want to thank the following people: to Capt Coleman for helping me in understanding experimental methods, to Mr. Joe Henderson for assisting me in part of the testing, and to Mr. and Mrs. Grazier for taking care of me while I was writing this thesis. Further, I would like to thank the Air Force Office of Scientific Research (Major Brian Sanders) and Air Force research Laboratory for the sponsorship of this work.

Finally, I am grateful to my parents, brother, sister and niece in Taiwan, for their continuous spiritual support during thses two years because I could not have succeeded without them.

Table Of Contents

List Of Figures

List Of Tables

List of Symbols

English Symbols

Symbol	Definition
$[A]$	extensional stiffness
$[a]$	extensional compliance
D	electric displacement
E_x	Young's modulus
E	Electric Field
F	capacitance (farads)
G	shear modulus
K_3^T	dielectric constant
N	cycles
$[N]$	force vector
P	polarity
Q	Electric Potential
$[Q]$	Stiffness
$[S]$	Compliance

Greek Symbols

Symbol	Definition
ε	strain

ε_0	permittivity of free space
μ	micro
ν	Poisson's Ratio
σ	stress

Subscripts

Symbol	Definition
f	fiber
m	matrix
S	symmetric
3	normal to xy-plane

Superscript

Symbol	Definition
°	degree

Abbreviations/Acronyms

Abbreviation	Definition
ACX	Active Control eXperts
AFIT	Air Force Institute of Technology
AFOSR	Air Force Office of Scientific Research
ATF	Advanced Tactical Flighter

DARPA	Defense Advanced Research Projects Agency
FPF	first ply failure
Hz	Hertz
MPa	megaPascal
PZT	lead zirconate titanate
PLZT	lead lanthanum zirconate titanate
QRMS-II	Questar Remote Measurement System
SMS	Smart Materials Structures Program
SPICES	Synthesis and Processing of Intelligent Cost Effective Structures
Ti	titanium
UDRI	University of Dayton Research Institute

AFIT/GAE/ENY/98S-02.

Abstract

This study primarily investigated the fatigue behavior of the embedded piezoelectric lead zirconate-titanate (PZT) actuators in graphite/epoxy laminate with a lay-up of $[0/+45/-45/90]_S$ under combined mechanical and electrical cycling loading. A secondary focus was the investigation of the mechanical fatigue effects of the $[0/0/+45/-45/0/0/90]_S$ laminate with embedded PZT under tensile loading. The embedded PZT, Active Control eXperts (ACX) QP15N, was inserted into a cutout area in the two middle 90° plies. All the fatigue tests were conducted with a triangular loading waveform which had a frequency of 10 Hz and with $R = 0.1$. In the electro-mechanical testing, specimens were first cycled within the PZT's operating strain range and then the maximum stress was increased in steps up to 100 MPa, which was twice the upper limit suggested by the manufacturer of the actuator. Meanwhile, the embedded actuator was excited by a -10 V to -100 V or a 10 V to 100 V voltage input, which resulted in either in-phase or out-of-phase electrically induced strain waveform with respect to the mechanical loading or strain. The voltage output of actuators was monitored during cycling, and failure was taken to be a reduction of 30 % of the original voltage output. For the mechanical fatigue testing, specimens with and without PZTs were tested at various stress levels and were run until the specimens failed or until two million cycles was reached. Comparison between specimens with and without PZTs was made using several parameters, such as first-ply failure, fatigue life, Young's modulus, and delam-

ination width. The damage sequence and degradation of the mechanical properties of the laminate due to embedding of PZTs was also investigated in this part of testing.

It was found that the PZTs performed very well during the out-of-phase electro-mechanical and low stress fatigue conditions when the applied strain was within the operating range of PZT. Below the PZT's operating range, electrical depolarization caused by negative voltage excitation during the in-phase electro-mechanical fatigue was the only factor to affect the performance of the actuator. Beyond the upper strain limit, the voltage output of the PZT was primarily influenced by the mechanical fatigue loading. As the maximum stress increased, the mechanical loading caused more piezoelectric damage in the actuators. Finally, the actuators failed after only 10,000 cycles at 100 MPa in out-of-phase and low stress loading tests.

At high stress levels, results from the monotonic tests showed that the average ultimate stress and modulus of specimens with or without PZTs were within 2 % of each other, which was not very significant considering the relatively large size of the embedded PZT. The fatigue life of MF (without PZT) and MAF (with PZT) specimens were very comparable as well, and MAF specimens actually had a slightly higher fatigue resistance. The overall range in modulus reduction for MF and MAF specimens were usually within 5-15 % of each other during fatigue loading. The rate of delamination growth of MF and MAF specimens during most of the fatigue life was also very comparable, with no significant variations.

Electro-Mechanical Fatigue Behavior of a Quasi-Isotropic Laminate with an Embedded Piezoelectric Actuator

1. Introduction

1.1 Background

Composite materials are not something exclusive to our era. Thousands of years ago, our ancestors were well aware of the advantage of mixing different materials to achieve specific desired properties, like stiffness or strength. A structural composite is defined as "a material system consisting of two or more phases on a macroscopic scale, whose mechanical performance and properties are designed to be superior to those of the constituent materials acting independently [6]." Nowadays, throughout the world, composite materials are widely applied in the various industries, including the defence industry. In military aerospace structures, composite materials are used to replace the traditional metallic materials such as alloys of aluminum, iron and titanium because of their lower weight and higher strength and stiffness. Clear examples are the B-2 stealth bomber and the F-22 Advanced Tactical Fighter (ATF), both constructed with composite materials in great proportions. Previous studies have demonstrated that the application of composite materials can lead to a substantial decrease in aircraft structural weight.

More specifically, a total aircraft weight reduction of up to 30% can be accomplished by the use of composite materials [8].

The development of composite materials is carried out to fulfill three main purposes. First, the development of these materials leads to more weight savings, especially for aerospace products. Second, a reduction in total cost, compared with that of conventional materials, can be attained because of these new composite materials. Finally, continued research can satisfy the need for quality assurance and predictability of behavior over the lifetime of the structure. Further, at the present time, a strong interest is being placed on the development of "smart materials," which involves a close integration of sensors, actuators and processors into an architecture of structural materials. Smart materials are defined as "a system or material which has built-in or intrinsic sensor/s, actuator/s, and control mechanism/s whereby it is capable of sensing a stimulus, responding to it in a determined manner and extent, in a short appropriate time and reverting to its original state as soon as the stimulus is removed [5]." This advanced technology is revolutionary in the sense that it provides the means to: (1) perform health and load monitoring of composite components within aerospace and industrial products, and (2) enable control systems such as smart skins, shape control, flow control, vibration control and acoustic control, to actively monitor and react to changes to the external environment.

First, health and load monitoring of aerospace structures requires an integrated system capable of monitoring loads and environment, detecting and assessing structural damage and lifetime in a timely manner, and communicating the overall health of the

structure. As an example, in the Smart Metallic Structures Program funded by the Defense Advanced Research Projects Agency (DARPA) and the Air Force, it has been shown that damages in structures can be detected by using a triangulation method. This study estimated that the potential savings of a health monitoring system would be $35 million per year for the F/A-18 and $10 million per year for the T-38. Therefore, it is expected that a significant decrease in maintenance cost will be achieved if this technology is implemented on all aircraft. Next, an example of control systems is vibration control, which is the ability of a structure to detect internal vibration and actively reduce or cancel the vibration. The Air Force funded a research project with the goal of studying the vibration suppression of the tails in the F-15 and the F/A-18. The technology developed in this research will make a contribution towards eliminating dynamic instabilities such as tail buffet or wing flutter and reducing fatigue damage [3].

Among the many candidate materials, piezoelectric materials, such as lead-zirconate-titanate (PZT), have attracted the attention of aerospace and commercial industries because of their specific ability to act as sensors and actuators and to be embedded in composite structures. The fundamental property of a piezoelectric ceramic is that whenever it is subjected to an electrical voltage, a mechanical strain is generated. Conversely, when a mechanical strain is applied to a piezoelectric material, it generates an electrical voltage.

Although it is envisioned that the aerospace industry will greatly benefit from the smart material technology, further research has to be done to gain better knowledge about the potentials and limitations of smart materials both intrinsically and when em-

bedded in a composite structure. Smart structure systems must be tested for accuracy, dynamic range, frequency response, noise rejection, embedding capability, health monitoring capability, and survivability, so that they can satisfy the requirement of being able to perform under harsh internal and external conditions.

Recently, studies about smart materials have been conducted, but a majority of the attention has focused on the actuator/sensor component performance and failure. Other studies have been conducted to analyze the integrity of smart material structures with embedded PZTs, embedded optical fibers, and glass inserts. However, very little work has been done on the response of the embedded actuators under the combined electric field and stress loading. This clearly shows the need for more studies in this area.

1.2 Problem Statement

The main objective of this research was to investigate the fatigue behavior of PZTs embedded in carbon/epoxy laminate with an orientation of $[0/+45/-45/90]_S$ under combined mechanical and electrical cyclic loading. Because Coleman had conducted the preliminary research on the $[0/0/+45/-45/0/0/90]_S$ laminate with embedded PZTs under mechanical cycling only [4], the second part of this study was to continue more research on the $[0/0/+45/-45/0/0/90]_S$ laminate with a focus on the mechanical fatigue effects. Through these experiments, the fatigue response of embedded PZT can be better understood, and it may help engineers and scientists to design and operate smart material systems in better and more efficient ways.

1.3 Approach

The host composite material chosen for this study was a Hercules AS4/3501-6 pre-preg, which has been widely used in military systems. The PZTs were placed in a cut-out area, which had the same size as the PZT, in the center of 90° plies before final curing. A strain gage was attached on the laminate surface, where the PZT was embedded in the laminate, in order to monitor the local region strain change due to any damage of the interface with the PZT and host structure. A Material Test System (MTS) extensometer was also employed to monitor the longitudinal strain during testing.

All tests were conducted at a frequency of 10 Hz and with a R ratio of 0.1. In the electro-mechanical fatigue testing, maximum stress levels were set at either 25,50,75 or 100 MPa, with the maximum stress level of 100 MPa equating to 2000 $\mu\varepsilon$, which was twice the upper limit suggested by manufacturer of the PZT. Meanwhile, the electrical loading was either in-phase or out-of-phase with mechanical loading. Capacitance and voltage output of the PZTs were recorded before cycling and at certain cycles during fatigue tests. Whenever a recorded voltage output fell below 50% of an original voltage, i.e. the voltage measured before a test, the PZT was repoled. After repoling, if the voltage measured was below 70% of an original voltage, the PZT was considered to have failed.

For the mechanical fatigue testing, specimens with and without PZTs were tested at various stress levels and were run until the specimens failed or until two million cycles was reached. Comparison between specimens with and without PZTs was made using several parameters, such as first-ply failure, fatigue life, Young's modulus, and delami-

nation width. The damage sequence and degradation of the mechanical properties due to embedded PZTs was also investigated in this part of the testing.

1.4 Document Layout

The remainder of this document is set in the following manner. Chapter 2 discusses previous research and theory. Chapter 3 is a detailed discussion of the preparation of the specimen and the development of the test set-up. This chapter also discusses the method used to perform the tests and collect the data. The test results are discussed in Chapter 4. Chapter 5 summarizes the conclusion of this study and recommendations for further research.

2. Previous Research and Theory

2.1 Research

2.1.1 Damage Mechanisms of Composite Structures

Since composite materials have been widely applied in various industries for the last several decades, the investigation of the damage progression of different composite structures can be seen in many reports. Among these reports, Talreja [20] first introduced a fatigue life diagram to analyze fatigue damage mechanisms for composite structures. Figure 1 shows a typical diagram for unidirectional composites under loading parallel to the fibers. In this diagram, fatigue damage can be divided into three regions. For angle-plied and cross-plied laminates, fatigue-life diagrams are similar to Figure 1, but fatigue life data falls into distinct regions.

When fatigue life data falls into the fiber breakage band, it indicates that the tested composite material is fiber-dominated and contains nonprogressive fatigue damage. In this type of damage mechanism, fiber breakage usually occurs at the weakest fiber in the composite. Shear stress is concentrated at the interface near the tip of the broken fiber due to fiber breakage and leads to debonding of the fiber from the surrounding matrix. The shear-stress concentration also causes breakage of the fiber adjacent to the previously broken fiber. In general, the locations of the fiber breaks are scattered randomly in the volume of the composite. The number of broken fibers increases with the number of the fatigue cycles. The final fracture occurs when the applied stress is high enough to break the remaining fibers.

The cycle-dependent progressive damage occurs in the region located between the lower bound of the fiber-breakage scatter band and the horizontal line representing the fatigue limit of the matrix. This sloping band represents matrix cracking and interfacial shear failure that may occur simultaneously, especially in the later part of the fatigue life. The fatigue limit of the matrix is a material property and is defined as the lower limit of the progressive matrix damage. When the cyclic maximum strain is below the fatigue limit of the matrix, no cracks can be found in the matrix material.

With sufficient knowledge of damage mechanisms, we still can not predict the fatigue life of composite materials without the knowledge of the growth rates of the mechanisms. Reifsnider et al. [12] introduced a graphical representation of the progressive damage sequence to analyze damage mechanisms. Figure 2 shows the schematics of the damage development in multidirectional composite laminates under fatigue loading. Initially, the primary matrix cracking occurs in off-axis plies. The number of cracks increase with load cycles, until eventually a crack saturation state is reached. As the primary matrix cracks form, shear-stress concentration initiates cracking in the adjacent plies and leads to interfacial debonding. After this point, the next stage may occur in the interior of a laminate and is called delamination, which is caused by highly interlaminar stress at the free edge of the laminate. As the fatigue cycles increase, the width of delamination keeps expanding until ultimate failure.

2.1.2 Electro-Mechanical Behavior of Piezoelectric Ceramics

The constitutive behavior for combined mechanical and electrical loading of various compositions of PZT and 8/65/35 lead lanthanum zirconate titanate (PLZT) was in-

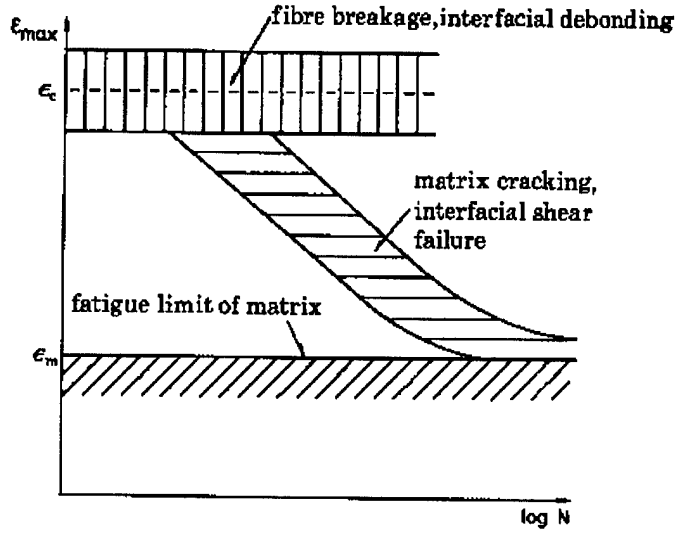

Figure 1. Fatigue-life diagram for Unidirectional Composites [20]

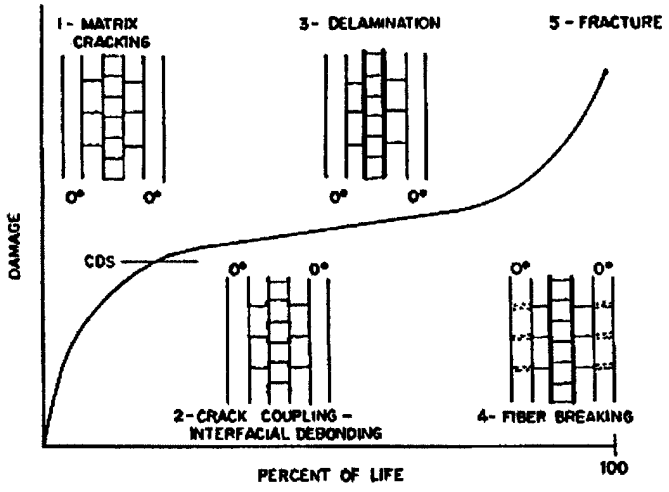

Figure 2. Development of Damage in Composite Laminates under Fatigue [12]

vestigated by Lynch [14,15]. Specimens were put in an oil bath preventing high voltage arcing and underwent compressive stress and high electric field simultaneously. Strains and polarization were monitored with strain gages and a capacitor. Lynch observed that soft piezoelectrics have a higher piezoelectric coefficient than hard piezoelectrics. However, hard PZTs have higher electrical and mechanical yield points that allow hard piezoelectrics to operate over a broader stress and electric field range.

Sun and Jiang [20] studied the fatigue behavior of PZT-4 under combined electrical and mechanical loading. This research was accomplished by using mechanical strain energy release rate as a single parameter to characterize fatigue crack growth in piezoelectrics. Specimens were charged with a constant electric field while the tension-tension cyclic mechanical load or a steady tensile load was applied while a time-varying electric field was applied. They concluded that the crack growth rate was influenced by the poling direction. Specifically, positive electric field loading caused a significantly greater crack growth rate than negative electric field loading.

2.1.3 Hysteresis of Piezoelectric Material

Nonlinear hysteresis is an important property that is present in piezoceramic actuator systems. This nonlinearity makes it difficult to predict the piezoceramic actuator system performance under operating conditions. Recently, Sreeram and Naganathan investigated hysteresis prediction for piezoceramic actuators in a closed loop motion control system [18]. This investigation was accomplished by establishing a reference hysteresis loop, which has positive and negative turning points of +100V and -100V respectively, under a bounding operating condition of a cyclic electric field. Minor

hysteresis loops for various mechanical and electrical loading conditions were then predicted by using a moving Preisach model. The results of this investigation showed that predictions using Preisach models agreed well with the experimental results, especially the turning points close to the bounding points. Besides, it was observed that minor hysteresis loops shifted either towards the positive bounding point or towards the negative bounding points until they arrived at a stable position. This shift is caused by the mechanism of memory formation in the model and is also found in the present study.

2.1.4 Structural Integrity Effects of Embedded Device

Coleman investigated the mechanical fatigue effects of a carbon-epoxy pre-preg composite structure embedded with PZTs under a tension-tension loading condition [4]. This investigation was conducted with an angle-ply lay-up of $[0/\pm 45/90]_S$ with $R = 0.1$ and a frequency of 10 Hz. Two types of specimens having the same dimensions were used in this study. The only difference between these two types of specimens was one group of specimens had a 50.8 $mm \times 24.5\ mm \times 0.254\ mm$ actuator embedded in the central, cut-out area. The result of monotonic tests indicated that the average ultimate stress and Young's modulus of two groups of specimens were within 4 % of each other. During the fatigue test, the modulus for the two types of specimens were usually within 5-15 % of each other. Coleman also observed that specimens with embedded PZTs had a longer fatigue life than specimens without PZTs. Overall, he concluded that it is feasible to embed PZTs inside composite laminates without significantly affecting the mechanical properties of the host structure.

Dosedel studied the effects of embedded optical fibers in an advanced composite material under compressive loading [7]. A 30-ply lay-up laminate which contains 40 percent 0° plies, 20 percent 90° plies, and 40 percent $\pm 45°$ plies was employed in this study, with a varying number of optical fibers of 125 μm or 240 μm outer diameter embedded either parallel or perpendicular to the composite fibers. Among a total of sixteen groups of specimens, the specimens that had two 240 μm optical fibers placed across the width of the specimen and perpendicular to surrounding structural fibers were found to result in the largest compressive strength reduction of 27 %. No modulus degradation was found in any of the other groups.

A series of tests were conducted by Vizzini to investigate applying an interlacing technology to improve the performance of laminates with embedded devices [9,16,17]. The results showed that using interlacing technology can increase the strength of composite structures and exhibit a better global performance than those using typical cutting-out technology.

2.2 Theory

In order to better understand the scope of this research, a brief background of composite materials and piezoelectric materials is provided in this section. The composite theory is taken from the text, "Engineering Mechanics of Composite Materials", written by Daniel and Ishai [6]. The piezoelectric theory is partly taken from the book, "Smart Structures and Materials", written by Culshaw, and partly from Brei's instructional papers [2,5].

2.2.1 Composite Materials

In classical lamination theory, the overall behavior of a multidirectional laminate is given by the combination of the properties and the stacking sequence of the individual layers. This theory predicts the overall properties of the laminate based on the following assumptions :

—Individual layers are assumed to be quasihomogeneous and orthotropic
—Individual layers are assumed to be in a state of plane stress
—Displacements are small compared with the thickness of the laminate and continuous through the laminate
—Straight lines normal to the middle surface remain straight and normal to that surface after deformation
—Strain-displacement and stress-strain relations are linear
—The transverse normal strain is negligible

In general, the stress-strain relations for most materials are given by the generalized Hooke's law as follows:

$$\{\sigma\} = [Q] * \{\varepsilon\} \tag{1}$$

$$\{\varepsilon\} = [S] * \{\sigma\} \tag{2}$$

where $\{\sigma\}$ is the stress vector, $\{\varepsilon\}$ is the strain vector, $[Q]$ is the stiffness matrix, and the compliance matrix $[S]$ is the inverse of the stiffness matrix. For a unidirectional lamina, the number of the components in each matrix is determined by conservation of energy, geometry and physical properties of the material. For example, like a general orthotropic material, the number of the independent elastic constants in both stiffness and compliance matrices can be reduced from 81 to 9 to characterize a material com-

pletely. When a state of plane stress is taken into consideration, the number of the independent elastic constants can be further reduced to 4. Thus, the above two equations can be expressed in a more specific form as follows:

$$\begin{pmatrix} \sigma_1 \\ \sigma_2 \\ \tau_6 \end{pmatrix} = \begin{bmatrix} Q_{11} & Q_{12} & 0 \\ Q_{12} & Q_{22} & 0 \\ 0 & 0 & Q_{66} \end{bmatrix} * \begin{pmatrix} \varepsilon_1 \\ \varepsilon_2 \\ \gamma_6 \end{pmatrix} \tag{3}$$

$$\begin{pmatrix} \varepsilon_1 \\ \varepsilon_2 \\ \gamma_6 \end{pmatrix} = \begin{bmatrix} S_{11} & S_{12} & 0 \\ S_{12} & S_{22} & 0 \\ 0 & 0 & S_{66} \end{bmatrix} * \begin{pmatrix} \sigma_1 \\ \sigma_2 \\ \tau_6 \end{pmatrix} \tag{4}$$

When the stress-strain relations are expressed in terms of engineering constants, we can get more physical meaning from stress-strain relations than that expressed in terms of mathematical constants. Relations between mathematical and engineering constants are shown in equation (5).

$$\begin{aligned} Q_{11} &= \frac{E_1}{1-\nu_{12}\times\nu_{21}} \\ Q_{22} &= \frac{E_2}{1-\nu_{12}\times\nu_{21}} \\ Q_{12} &= \frac{\nu_{12}\times E_2}{1-\nu_{12}\times\nu_{21}} = \frac{\nu_{12}\times E_2}{1-\nu_{12}\times\nu_{21}} \\ Q_{12} &= \frac{\nu_{12}\times E_2}{1-\nu_{12}\times\nu_{21}} \end{aligned} \tag{5}$$

where E is Young's modulus, and ν is Poisson's ratio.

The elements in the compliance matrix can be expressed in terms of these same properties by converting the stiffness matrix. For any arbitrary coordinate system related to an angle between fiber orientation and loading axes, the stress-strain relation is expressed in the form

$$\{\sigma\} = [\overline{Q}] * \{\varepsilon\} \tag{6}$$

To transform from the $[Q]$ to $[\overline{Q}]$ matrix, the transformation matrix [T] is used :

$$[\overline{Q}] = [T]^{-1} * [Q] * [T] \tag{7}$$

$$[T] = \begin{bmatrix} \cos^2\theta & \sin^2\theta & 2\cos\theta\sin\theta \\ \sin^2\theta & \cos^2\theta & -2\cos\theta\sin\theta \\ -\cos\theta\sin\theta & \cos\theta\sin\theta & (\cos^2\theta - \sin^2\theta) \end{bmatrix} \tag{8}$$

When dealing with the stress-strain relations of a multidirectional laminate, the general expression relating in-plane forces and moments to reference plane strains and curvatures are given as follows:

$$\begin{bmatrix} N \\ M \end{bmatrix} = \begin{bmatrix} A & B \\ B & D \end{bmatrix} * \begin{bmatrix} \varepsilon^0 \\ \kappa \end{bmatrix} \tag{9}$$

where N are applied forces per unit length, M are applied moments per unit length, ε^0 are reference plane strains, and κ are reference plane curvatures, and

$$[A] = \sum_{1}^{n} * [\overline{Q}] * (Z_k - Z_{k-1})$$

$$[B] = \frac{1}{2} * \sum_{1}^{n} * [\overline{Q}] * (Z_k^2 - Z_{k-1}^2) \tag{10}$$

$$[D] = \frac{1}{3} * \sum_{1}^{n} * [\overline{Q}] * (Z_k^3 - Z_{k-1}^3)$$

where n is the number of plies in the laminate and Z_k is the thickness of each ply.

Since a symmetrical $[0/\pm 45/90]_s$ quasi-isotropic laminate under plane stress was investigated in this study, the coupling stiffnesses are equal to zero, and no moments are acting on the laminate. Therefore, equation (9) can be simplified and shown as in equation (11).

$$\begin{pmatrix} N_x \\ N_y \\ N_s \end{pmatrix} = \begin{bmatrix} A_{xx} & A_{yx} & A_{xs} \\ A_{yx} & A_{yy} & A_{ys} \\ A_{sx} & A_{sy} & A_{ss} \end{bmatrix} * \begin{pmatrix} \varepsilon_x^0 \\ \varepsilon_y^0 \\ \gamma_s^0 \end{pmatrix} \tag{11}$$

and

$$Q_{xx}(\theta = 0) = Q_{11}$$

$$Q_{xx}(\theta = 90) = Q_{22}$$

$$Q_{xx}(\theta = 45) = \frac{1}{4} * (Q_{11} + Q_{22} + 2 * Q_{12} + 4 * Q_{66})$$

$$A_{xx} = \frac{t}{8} * (3 * Q_{11} + 3 * Q_{22} * 2 * Q_{12} + 4 * Q_{66}) \tag{12}$$

$$A_{yy} = A_{xx}$$

$$A_{xy} = \frac{t}{8} * (6 * Q_{12} + Q_{11} + Q_{22} - 4 * Q_{66})$$

$$\bar{E}_x = \frac{1}{t} * (A_{xx} - \frac{(A_{xy})^2}{A_{xx}})$$

where t is the thickness of the laminate, $\bar{E}_x$ is the Young's modulus for the laminate in the loading direction, and the detailed material properties are provided in appendix A.

2.2.2 Piezoelectric Materials

A material can be defined as piezoelectric if the application of an external mechanical strain causes the development of an internal dielectric displacement. This displacement is linearly proportional to the applied strain. On the other hand, the application of an external electric field causes a mechanical strain of the material. In general, the piezoelectric nature is caused by the change of position of the Ti^{+4} ion in the center of a perovskite crystal structure, while the structure is cooled. Figure 3 shows the crys-

tal structures at above or below the Curie temperature. When the structure is cooled through the Curie temperature, it transforms from a cubic lattice to a tetragonal lattice in which the negative and positive charge sites no longer coincide and result in a net dipole moment. This net dipole moment causes a net polarization when a high electric field is applied, which makes the dipole align with the poling direction in the crystal structure.

The polarization of a piezoelectric crystal varies with the applied strain or electric field and is direction-dependent. Equations (13) and (14) show the coupled linear constitutive laws derived using energy considerations. These equations are formulated with electric field (E) and stress (X) as independent variables.

$$D = dX + \varepsilon^x \varepsilon_0 E \tag{13}$$

$$x = s^E X + dE \tag{14}$$

where D is the electric displacement vector, d is the piezoelectric strain coefficient, x is the strain, ε^x is the relative dielectric constant, ε_0 is the permittivity of free space , and s^E is the mechanical compliance.

When piezoelectric materials are loaded by a large stress, they exhibit a non-linear relation between electric field and stress. Hence, the above two equations no longer can be used to describe non-linear constitutive behavior. Figure 14 shows dielectric hysteresis loops which are employed to explain the relation between electric displacement and the electric field. As mentioned earlier, a net polarization occurs when the mater-

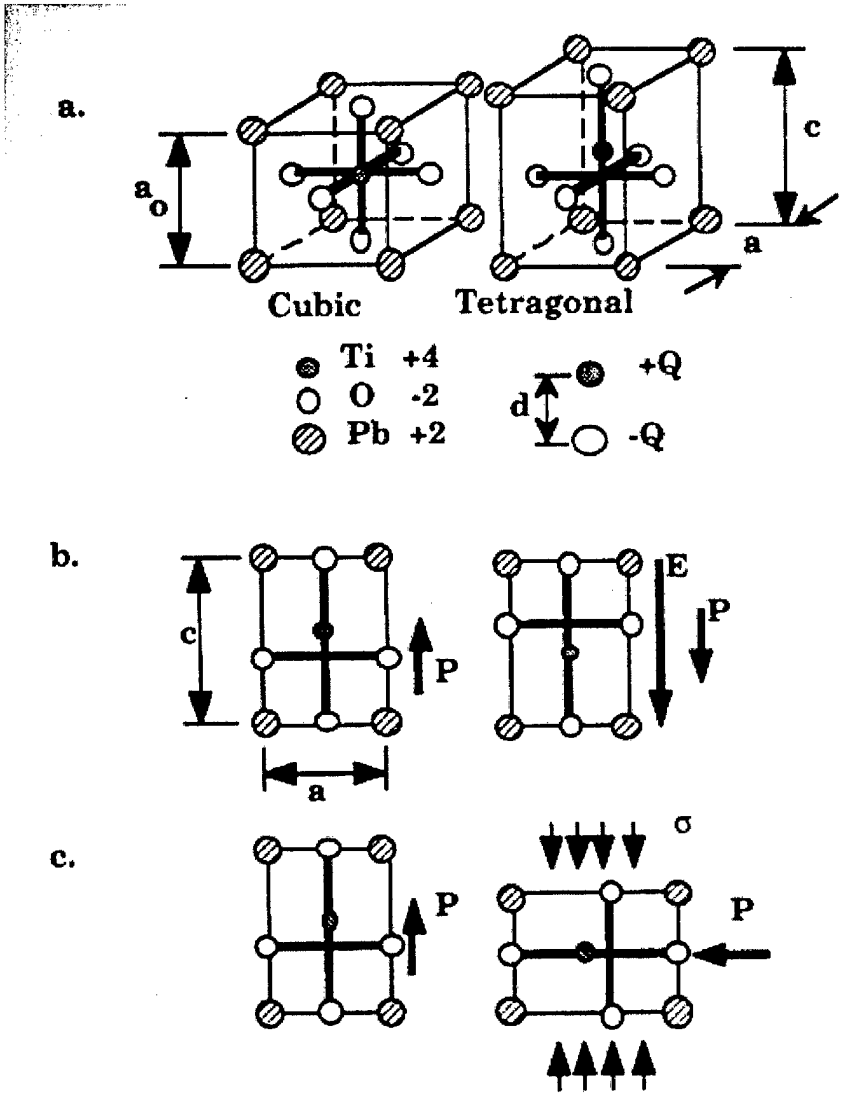

Figure 3. Crystal Structure of Piezoelectric Material

ial is kept at a temperature below the Curie temperature and an electric field is applied. The polarization increases with increasing applied electric field until a value E_c known as the coercive field is reached, where the polarization begins to switch directions. If an opposite electric field is applied, polarization initially falls to remanent polarization P_r, where the field is reduced to zero, and then increases in the negative direction until a negative coercive field is reached, where the polarization begins to switch directions again. If a positive field is applied, polarization eventually goes back to the positive direction and makes it a closed loop.

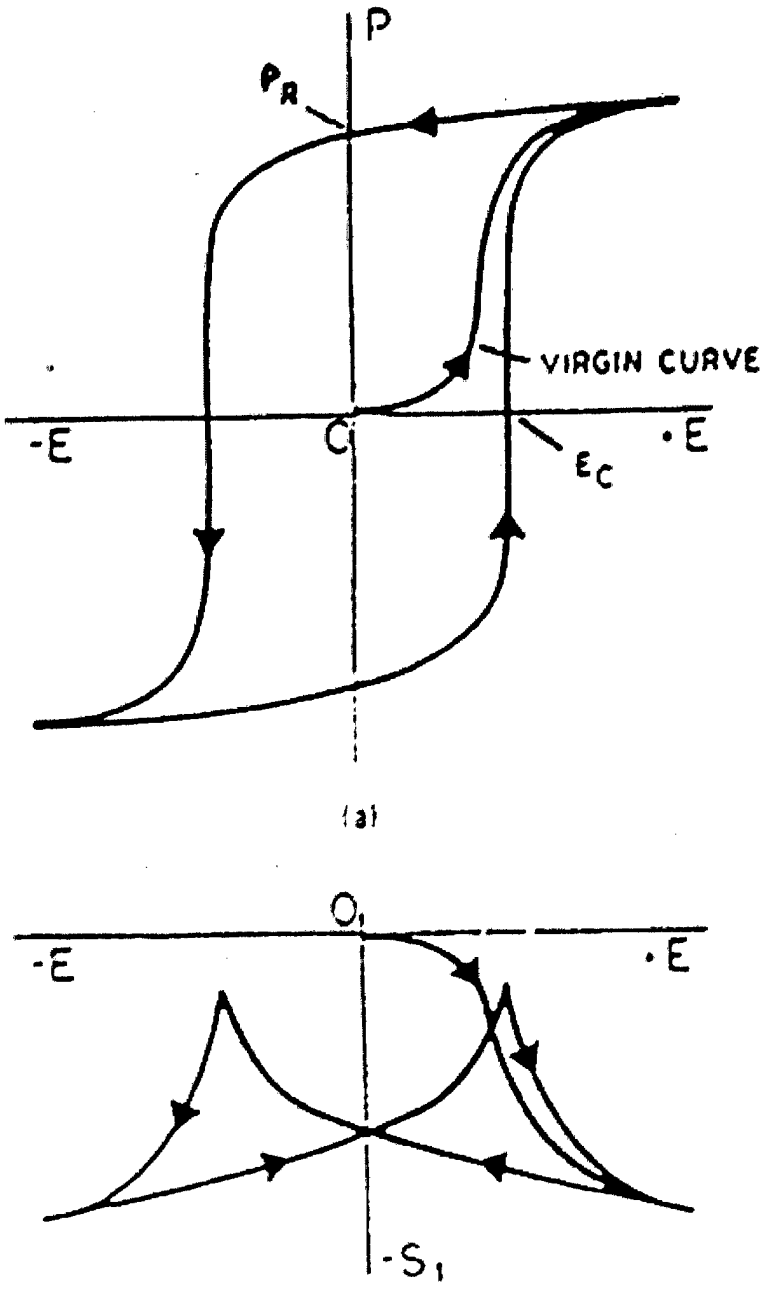

Figure 4. Polarization vs Electric Field Hysteresis Loop

3. Specimen Preparation and Test Procedure

The purpose of this chapter is to provide a detailed description of the material, specimen preparation, test equipment used, and the test procedures followed in this research. The details of the equipment setup are also provided.

3.1 Material Description

3.1.1 Composite Material

The material investigated in this research was a graphite/epoxy (AS4/3501-6) pre-preg composite from Hercules Inc. of Magna, Utah. The thickness of a single ply is approximately 0.13 mm. Each single ply contains thousands of continuous AS4 carbon fibers which can be parallel or oriented at a certain angle to the longitudinal direction. The epoxy matrix surrounds the fibers and plays a role of load transfer and structural integrity. The term "pre-preg" implies that the fibers and matrix have been combined together and are made as rolls of plies by manufacturer. Hence, the pre-preg composite materials can be easily stacked into different lay-up laminates [10].

3.1.2 Piezoelectric Material

The piezoelectric material, used as a embedded device within the AS4/3501-6 composite material, was a pre-packaged Active Control eXperts (ACX) QP15N. The dimensions of the QP15N were approximately 50.8 $mm \times 25.4\ mm \times 0.254\ mm$, and with a 25.4 $mm \times 12.7\ mm \times 0.254\ mm$ extended lead section starting at the base of the PZT. This device can be considered as a sensor or an actuator, depending upon the application for which it is used. As a sensor, a cyclic voltage approximately linearly

proportional to the applied stress is measured if a cyclic load is applied. As a actuator, a positive or a negative strain is generated when a cyclic voltage is applied. In a normal operating condition, the expected life of QP15N is above 10 million cycles or an infinite life when the applied loading results in a maximum strain of 1000 $\mu\varepsilon$ or 200 $\mu\varepsilon$, respectively [1]. Figure 5 is a photograph of this device.

3.2 Specimen Preparation

3.2.1 Specimen Lay-up and Dimensions

Two different lay-ups were constructed for the two objectives of this research. For the first objective, involving investigation of the electro-mechanical behavior of embedded PZT actuators, the "EAF" specimens were fabricated with a fiber orientation of $[0/+45/-45/90]_S$. The "EAF" specimens had a dimension of 305 mm in length and 50.8 mm in width, while a PZT was placed inside a cut-out area of the two middle 90° plies of the laminate. The second type of specimens were fabricated with a fiber orientation of $[0/0/+45/-45/0/0/90]_S$ for the investigation of mechanical fatigue response of the laminate with an embedded PZT. These "MAF" specimens, which had an embedded PZT within the cut-out area of two central 90° plies, had the same size as the "EAF" specimens, and one of these specimens was labeled with the "MA" prefix for the monotonic testing. The "MF" specimens, which were without sensor embedded inside the laminate, had the dimension of 305 $mm \times 25.4\ mm$, and one of these specimens was labeled with the "MM" prefix in order to compare the response with the "MA" specimen when subjected to the monotonic loading.

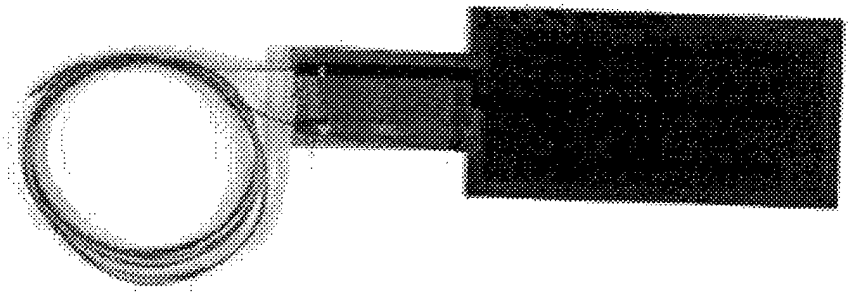

Figure 5. Active Control eXperts (ACX) QP15N PZT

3.2.2 Manufacturing Method

Before fabricating the specimens, the first problem we had to face was how to put the PZTs into the composite laminate. Two methods, the cut-out method and simply inserting the PZTs between the plies of the laminate, were taken into consideration. The cut-out method was chosen in order to prevent a change of the thickness and surface properties of the laminate induced by simply inserting sensor/actuator into the laminate, even though the cut-out method might cause a strength reduction of the laminate.

After the cut-out method was selected, all of the specimens were constructed by the University of Dayton Research Institute (UDRI). Four specimens were made from each panel, which had an approximate size of 30.5 $mm\times$ 30.5 mm. An area approximately 50.8 $mm\times$ 25.4 mm was cut-out from two 90° plies at the center of the laminate in order to meet the size of every embedded sensor. Before the other plies were stacked up to form the final lay-up, based on previous experience [4], Kapton tape was used to hold the wires of the PZTs in place and prevent the lead wires from snapping off at the edge of the panel during the manufacturing process.. After the panel had been prepared, the composite was heated and cooled in a autoclave for several hours. This procedure ensures the removal of volatiles, joining of the plies, and the final curing of the epoxy. Figure 6 shows an actuator placed in the lower 90° ply and the Kapton tape employed to keep the wires in place at the edge. Figure 7 shows the upper 90° ply of the laminate.

During the thermal curing cycle, the panel was heated up to 176.6° C, which was close to the Curie temperature of the PZTs and could cause depoling of the PZTs. Also, the residual stress might cause cracking in the actuators during the thermal curing cy-

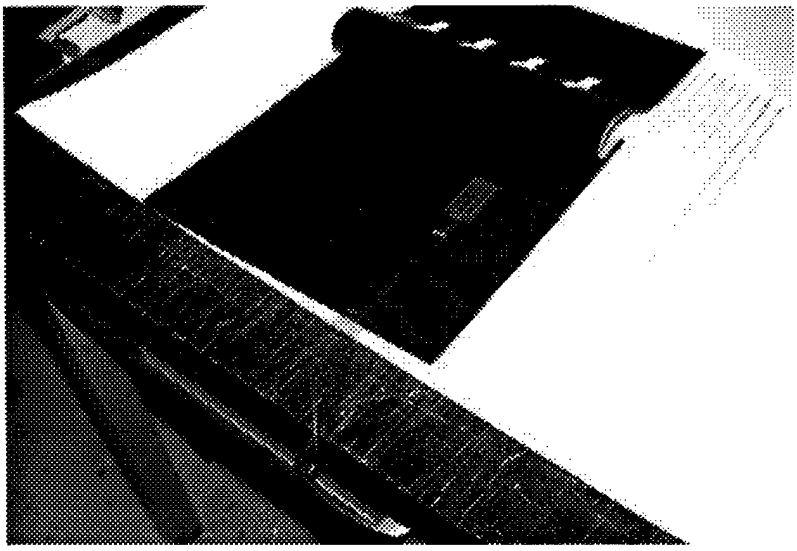

Figure 6. An Actuator Placed in the Lower 90° Ply

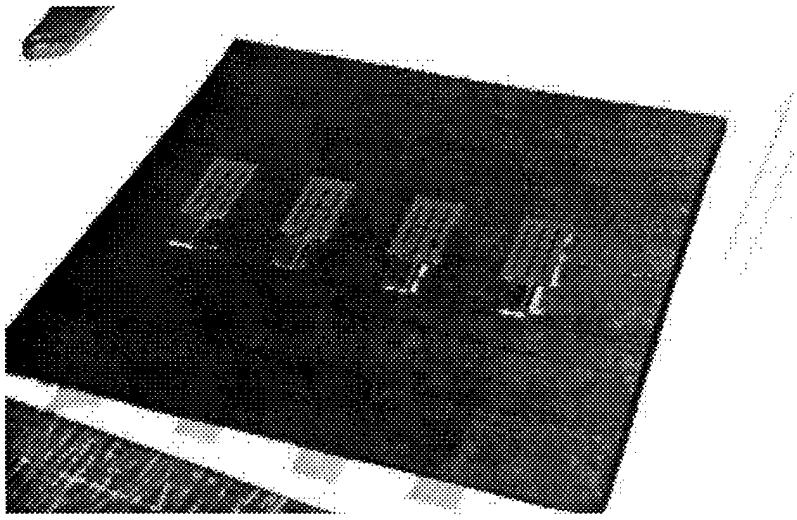

Figure 7. The Upper 90° Ply of The Laminate

cle. After discussing with ACX and adopting the method studied by the Synthesis and Processing of Intelligent Cost Effective Structures (SPICES) program, a few steps were used to ensure depoling, cracking and flaws would not occur during the manufacturing process [11]. First, during the thermal cycling, the lead wires were connected together to avoid cracking in the actuator. The capacitance of the actuators were measured to compare with the design specification of 100 nF after the specimens were made. The C-scan technique was used to ensure that no defects or broken wires were inside the specimens.

The final step in the specimen fabrication procedure was to affix tabs to the ends of each specimen. The tabs were used to protect the composite material from damage as the specimen was gripped in the test machine. The tabs were 38.1 mm long, 2.54 mm thick, and cut to the same width as the individual specimens. The ends of the tabs were beveled 30° to try to minimize any stress concentrations in the grip. Four tabs per specimen were then glued onto the specimens using a 50/50 mixture of a V-40 curing agent and an epoxy resin. The tabs were held in place while curing in a 170° C oven for about an hour with binder clips. After removal from the oven, the specimens were ready for polishing. Figure 8 shows the configuration and dimensions of the EAF specimens.

3.2.3 Polishing

The specimens were polished on one edge in order to be able to take photographs for documentation of the damage. A Struers Transpol-2 variable grinder-polisher was used for this operation. A series of Buehler Metadi waterbase diamond suspensions was

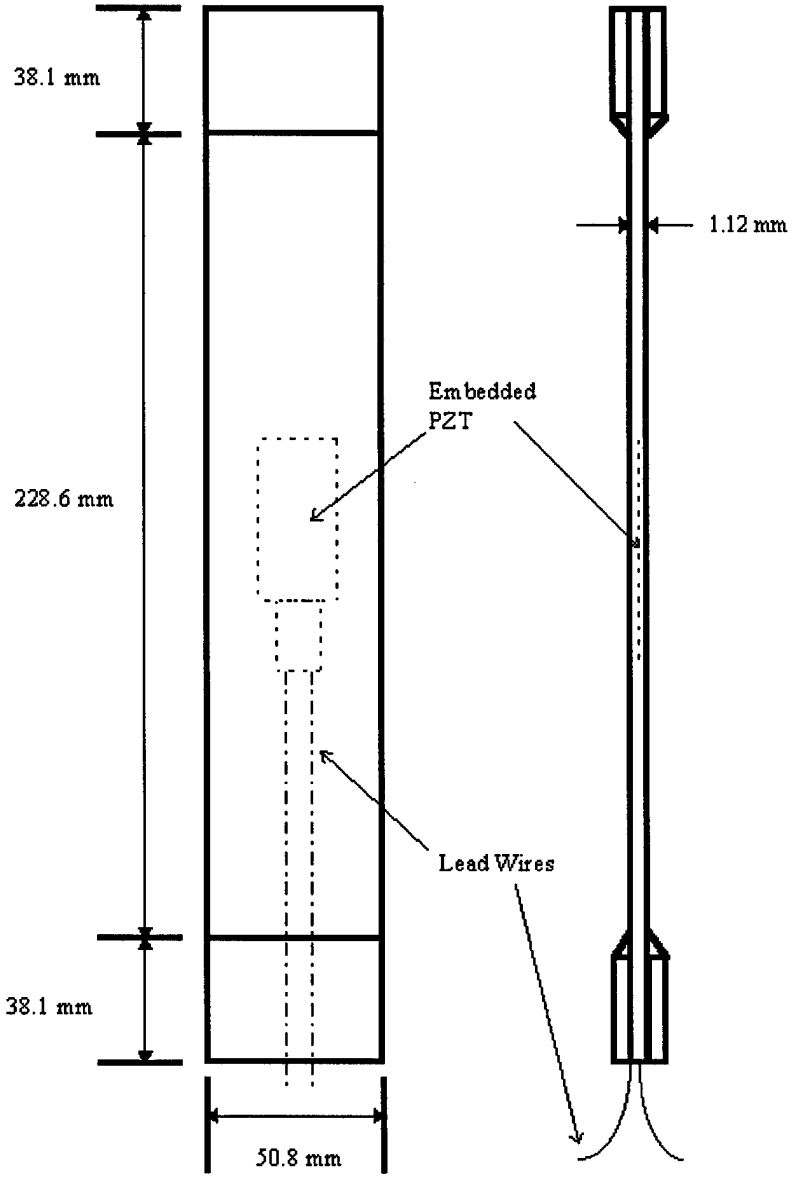

Figure 8. Specimen with Embedded PZT

employed to produce the necessary finish on the specimen. The first step consisted of ten minutes using a rough grind diamond wheel to ensure a flat, perpendicular surface. Next a fine grind diamond wheel was used for ten minutes to prepare the specimen for final polishing. Final processing was accomplished by polishing with a three micron suspension on the DP-Mol cloth for 20 minutes.

3.3 Test Equipment

3.3.1 Strain Measurement

In order to monitor the embedded PZT's local strain change, 120 ohm precision strain gages were used. A strain gage was attached with M-Bond 610 cement on the surface of the specimen where an actuator was placed in the center of the laminate. Thereby, any damage occuring in the interface of the PZT and host structure could be detected when the specimen was subjected a combined electric field and stress loading. A 101.6 mm extensometer was chosen to measure the longitudinal strain across the specimens with embedded sensors in the mechanical fatigue tests. The MTS Model 632.11B-20, GL 4.00 extensometer was mounted to the edge of the specimen, and epoxy was used to prevent the extensometer from slipping during cycling.

3.3.2 Damage Assessment

The Questar QM100 Remote Measurement System II (QRMS-II) was used for the objective of detecting transverse cracks. The QRMS-II optical system had an encoder resolution of one micron and a system resolution of 5 micron. Magnification of the digital image to the computer monitor was approximately 500X. Once the edges of the specimens were polished, a strobe light and optical system could accurately detect

transverse cracking when the specimen was put under a load. In addition, the QRMS-II system was also used to measure the initiation and width of the delamination at the edges.

3.3.3 Actuator Health Monitoring

When the electric field and mechanical loading was applied to the specimens, the embedded actuators might be cracked or depoled. Therefore, after a certain number of cycles, the voltage output of the actuators was measured via a voltage divider, MTS voltage meter, and computer software developed by Mr. Charlie Mcneely of AFIT. If a recorded voltage output fell below 50% of an original voltage, i.e. the voltage measured before a test, the PZT would be repoled. The Hewlet Packard 3466A Digital Multimeter and a Bertan Associates Incorporated High Voltage Power Supply, Series 230, were used for this purpose. As the tests were halted for measuring the voltage output of the PZTs, a capacitance check was also conducted to monitor the health of the actuators with a B+K Precision Dynascan Corporation 810B capacitance meter. If capacitance fell below the specification standard of 100 nF, then the PZT was also repoled.

3.3.4 Material Test System

The MTS 810 Material Test System consisted of a test frame with a 100 kN MTS 647.10 Hydraulic Wedge Grip, a MTS 464.80 Data Display Module, and a MTS 458 Microconsole. Additional equipment used for these tests included a 586 DAEWOO Pentium computer , an ACX 1224/5 QuickPack Power Amplifier, and a Tektronix TDS 420A Digitizing oscilloscope. The fatigue testing was controlled by the personal computer with the software developed by Mr Charlie Mcneely. As the specimen was sub-

jected to mechanical loading by MTS system, the PZT was excited by the ACX power amplifier. The Tektronix oscilloscope was used to monitor the wave form of the cyclic load input. The test equipment setup is shown in Figure 9.

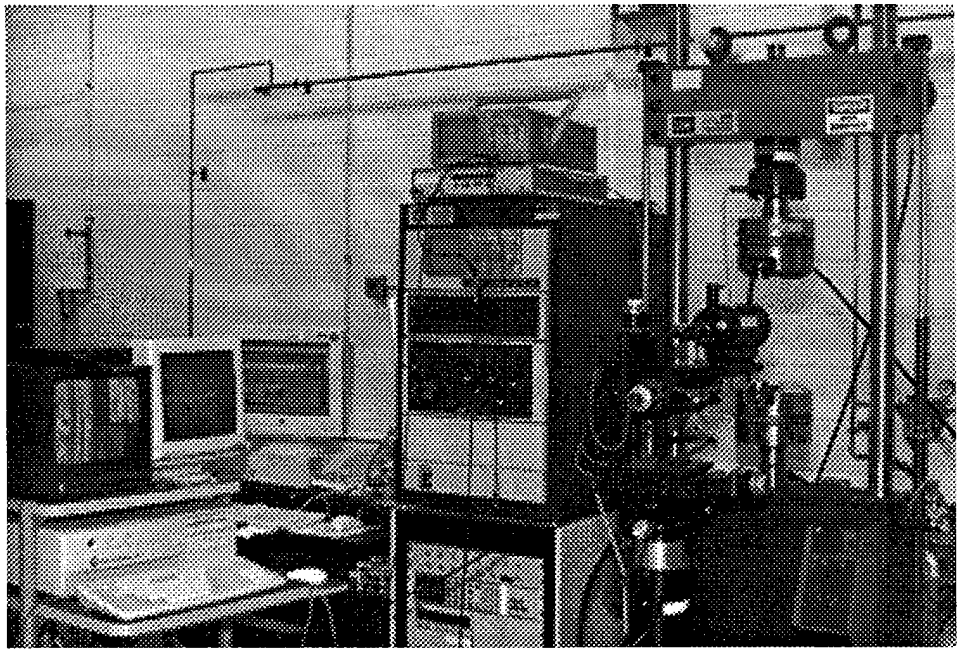

Figure 9. Test Setup with Telemicroscope QRMS-II

3.4 Test procedure

Three different types of tests were performed on the MTS 810 system for this study: electro-mechanical fatigue tests, monotonic mechanical tests, and mechanical fatigue tests. All fatigue tests were accomplished under tension-tension loading with $R = 0.1$ (constant amplitude) and at a frequency of 10 Hz. An electric field was applied on the embedded PZT for electro-mechanical fatigue tests. In general, test procedures were very similar for all three tests, but EAF specimens needed additional preparation prior to testing.

First, a strain gage was mounted on the center of the laminate surface and care was taken to assure alignment of the gage with the zero degree fibers on the specimens. According to the specifications of the QP15-N, when a tensile loading is applied on the PZT, a negative voltage output should be obtained. Hence, the polarity of the PZTs were determined using the Tektronix TDS 420A oscilloscope to monitor the in-phase or out-of-phase waveforms generated by the electric field and tensile stress. After determining the polarity of the PZT, the PZT was repoled for 15 minutes. This was accomplished by applying a 250 V positive voltage to pin one (positive polarity) of the actuator and with pin four (negative polarity) connected to ground.

Before the specimen was installed for testing, the correct loading card was inserted into the microconsole of the test machine so that the maximum load necessary for each test would be provided for by the card. After this, Hydraulic pressure was turned up from "Low" to "High" to actuate the grips. The grips were raised and lowered for specimen installation using displacement control. The specimen was first placed into the top grip and then aligned with an alignment tool before the grip pressure was actuated. After the top end of the specimen was secured, the microconsole controller was switched to load control before the bottom of the specimen was gripped. This ensured that no load would be on the specimen during the application of the bottom grip pressure.

An extensometer was then attached to the edge at the middle portion of the specimen. Springs were used to secure the extensometer, and epoxy was also employed on the edge to ensure that the extensometer would not slip during testing. The exten-

someter was connected to the signal amplifier, the restraining pin was removed, and the displacement reading was zeroed.

The software, DUAL-SMT, was used to control the fatigue testing. After the required testing conditions and specimen dimensions were entered , the program provided load and displacement measurements at many intervals during cycling. Transverse cracking, delamination width, and modulus degradation were measured at 500,1000, 5000, 10000, ... cycles until failure. For EAF specimens, the capacitance and voltage output of the PZT was also recorded at the same time intervals. Failure for EAF specimens was declared when the voltage output of PZT dropped below 70 % of the original voltage output of the PZT before cycling. A summary of all tests conducted in this study is provided in Table 1.

Table 1. Specimen Dimensions and Testing Conditions

Test Types	**Specimens**	**Dimensions (mm)**	**Testing Conditions**	**Remark**
Monotonic Test	MM1	$305 \times 25.4 \times 2.16$	$\sigma = 960\ MPa$	Without PZT
	MA1	$305 \times 50.8 \times 2.16$	$\sigma = 942\ MPa$	With PZT
Fatigue Test Eelctro-Mechanical Loading $R = 0.1, 10Hz$	EAF1	$305 \times 50.8 \times 2.16$	$\sigma = 25, 50\ MPa$, O-P	With PZT
	EAF2		$\sigma = 25, 50\ MPa$, I-P	
	EAF3		$\sigma = 75\ MPa$, I-P	
	EAF4		$\sigma = 75$, $100\ MPa$, O-P	
	EAF5		$\sigma = 87.5\ MPa$, O-P	
	EAF6		$\sigma = 87.5\ MPa$, I-P	
Fatigue Test Mechanical Loading $R = 0.1, 10Hz$ (High Stress)	MF1	$305 \times 25.4 \times 2.16$	$\sigma = 760\ MPa$	Without PZT
	MF2		$\sigma = 700\ MPa$	
	MF3		$\sigma = 660\ MPa$	
	MF4		$\sigma = 600\ MPa$	
	MAF1	$305 \times 50.8 \times 2.16$	$\sigma = 700\ MPa$	With PZT
	MAF2		$\sigma = 740\ MPa$	
	MAF3		$\sigma = 550\ MPa$	
Fatigue Test Mechanical Loading $R = 0.1, 10Hz$ (Low Stress)	EAF7	$305 \times 50.8 \times 2.16$	$\sigma = 50\ MPa$	With PZT
	EAF8		$\sigma = 75\ MPa$	
	EAF9		$\sigma = 87.5\ MPa$	
	EAF10		$\sigma = 100\ MPa$	
'O-P' indicates out-of- phase ,' I-P' indicates in-phase				

4. Results & Discussion

The purpose of this study was to investigate the fatigue behavior of PZTs embedded in carbon/epoxy laminate with an orientation of $[0/+45/-45/90]_S$ under combined mechanical and electrical cyclic loading. In addition, the investigation of the mechanical fatigue effects of the $[0/0/+45/-45/0/0/90]_S$ laminate with embedded PZTs is also provided in this chapter. All the fatigue tests were conducted with a triangular loading waveform which has a frequency of 10 Hz, and with a R ($\sigma_{\min}/\sigma_{\max}$) of 0.1.

In the electro-mechanical fatigue testing, the first maximum stress was chosen at 25 MPa, which corresponded to approximately 500 $\mu\varepsilon$ for the embedded actuator, and then increased in steps up to 100 MPa, which was twice the upper limit suggested by the manufacturer of the actuator. Meanwhile, the embedded actuator was excited by a -10 V to -100 V or a 10 V to 100 V voltage input, which resulted in either in-phase or out-of-phase electrically induced strain waveform with mechanical loading or strain, respectively. Capacitance and voltage output of the actuator was recorded before cycling and at certain cycles during testing. Data recorded from the strain gage was used to analyses any damage of the interface between the PZT and the laminate.

For the mechanical fatigue testing, specimens with and without PZTs were tested at various stress levels and were run until the specimens failed or until two million cycles was reached. Comparison between specimens with and without PZTs was made using several parameters, such as first-ply failure, fatigue life, Young's modulus, and delamination width. The damage sequence and degradation of the mechanical properties due

to embedding of PZTs was also investigated in this part of the testing. Table 2 shows the tests conducted for the purpose of this study.

4.1 Electro-Mechanical Fatigue Testing

Six specimens were tested with the goal of determining the effects of electro-mechanical fatigue loading on a quasi-isotropic laminate with embedded piezoelectric actuators. In order to compare with the results from electro-mechanical loadings on embedded PZT, four specimens were tested under mechanical loading only. Each specimens was inspected before and after cycling for cracking or delamination by the QRMS-II. Since EAF specimens were tested at low-strain levels, no cracking was found by microscope throughout all testing. Ultrasonic inspection was also used on two specimens and showed no damage. Strain gage data also showed no unusual signals during testing.

4.1.1 Degradation of Voltage Output

As mentioned in Chapter two, in a small strain range, when piezoelectric materials are strained, the voltage output increases almost linearly with increasing strain. The converse is also true; the strain of the piezoelectric material increases linearly with applied voltage. Hence, when the tensile stress and positive electric field are applied on the embedded actuator simultaneously, the strains generated by the mechanical and electrical loading are out-of-phase. When the embedded actuators are subjected to tensile stress and negative electric field at the same time, the strains generated by the mechanical and electrical loading are in-phase. Figure 10 shows the electrical and mechanical

Table 2. Summary of Tests

Test Types	**Specimens**	**Testing Conditions**	**Fatigue Cycles**	**Remark**
Monotonic Test	MM1	$\sigma = 960\ MPa$		Without PZT
	MA1	$\sigma = 942\ MPa$		With PZT
Fatigue Test Electro-Mechanical Loading $R = 0.1, 10Hz$	EAF1	$\sigma = 25\ MPa$, O-P	1,000,000*	With PZT
	EAF1	$\sigma = 50\ MPa$, O-P	1,000,000*	
	EAF2	$\sigma = 25\ MPa$, I-P	1,000,000*	
	EAF2	$\sigma = 50\ MPa$, I-P	850,000	
	EAF3	$\sigma = 75\ MPa$, I-P	150,000	
	EAF4	$\sigma = 75\ MPa$, O-P	1,000,000*	
	EAF4	$\sigma = 100\ MPa$, O-P	10,000	
	EAF5	$\sigma = 87.5\ MPa$, O-P	800,000	
	EAF6	$\sigma = 87.5\ MPa$, I-P	120,000	
Fatigue Test Mechanical Loading $R = 0.1, 10Hz$ (High Stress)	MF1	$\sigma = 760\ MPa$	16,383	Without PZT
	MF2	$\sigma = 700\ MPa$	302,794	
	MF3	$\sigma = 660\ MPa$	729,760	
	MF4	$\sigma = 600\ MPa$	2,000,000*	
	MAF1	$\sigma = 700\ MPa$	1,472,029	With PZT
	MAF2	$\sigma = 740\ MPa$	180,881	
	MAF3	$\sigma = 550\ MPa$	2,000,000*	
Fatigue Test Mechanical Loading $R = 0.1, 10Hz$ (Low Stress)	EAF7	$\sigma = 50\ MPa$	1,000,000*	With PZT
	EAF8	$\sigma = 75\ MPa$	1,000,000*	
	EAF9	$\sigma = 87.5\ MPa$	1,000,000*	
	EAF10	$\sigma = 100\ MPa$	10,000	
'$*$' indicates no failure				
'O-P' indicates out-of- phase , 'I-P' indicates in-phase				

loadings and the corresponding strains relationships of out-of-phase and in-phase conditions.

Before testing, every specimens was calibrated under tension loading to obtain a reference strain versus voltage output curve, which was also used to check the health of the actuators. All of the EAF specimens had voltage outputs which originally fell on this curve. Therefore, the embedded specimens demonstrated a consistent output with applied mechanical loads, until some damage occurred. Figure 11 shows the linear response of the embedded PZT to the increasing levels of applied stress. The top line is the maximum positive voltage, while the bottom line corresponds to the minimum voltage output of the PZT under cyclic tensile loading up to 50 MPa.

4.1.1.1 Out-of-Phase Tests

Specimen EAF1 was first cycled from 2.5 MPa to 25 MPa combined with a 10 V to 100 V electric field. The voltage output was first checked at every 5,000 cycles, while the specimen was cycled only in tension-tension loading. Capacitance measurements were also taken at the zero stress level. At this time, the QRMS-II was used to inspect any cracking if occurred at the edge. Since no degradation of voltage output was measured at 25,000 cycles, the check point intervals were reset to 10000, 50000, 100000, ... Specimen EAF1 survived up to one million cycles with almost no drop in the voltage output. The voltage output only dropped by 3 %. Figure 12 shows the voltage output versus cycles curve.

The same specimen was then repoled using the HP digital multimeter and the Bertan high voltage power supply. A value of 15.53 V voltage output was measured af-

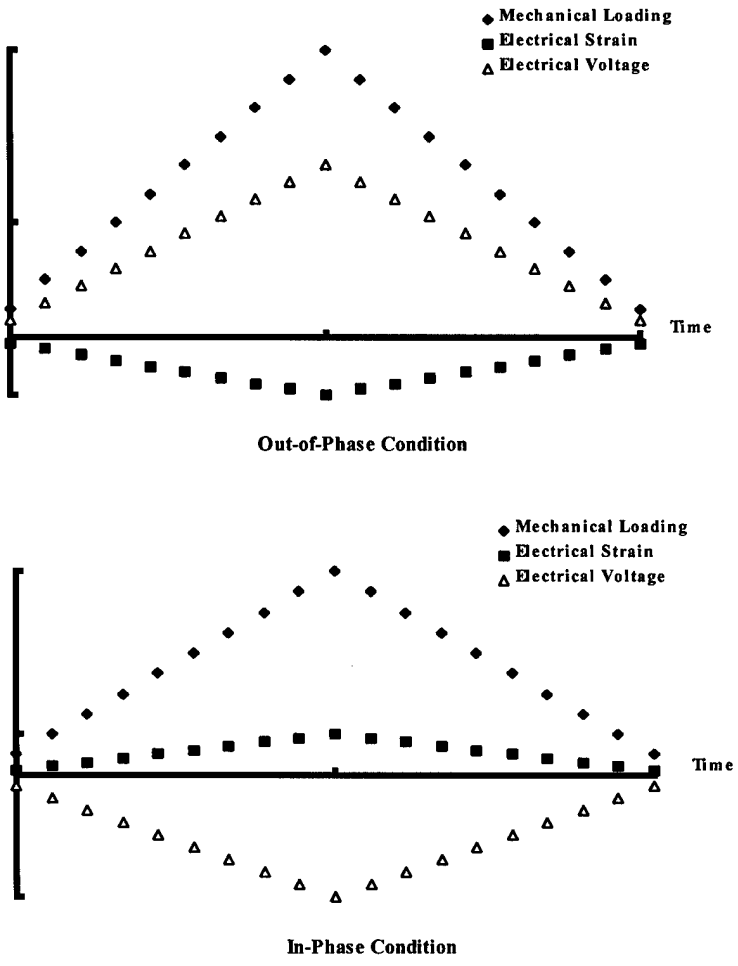

Figure 10. In-Phase and Out-of-Phase Electromechanical Fatigue Loading

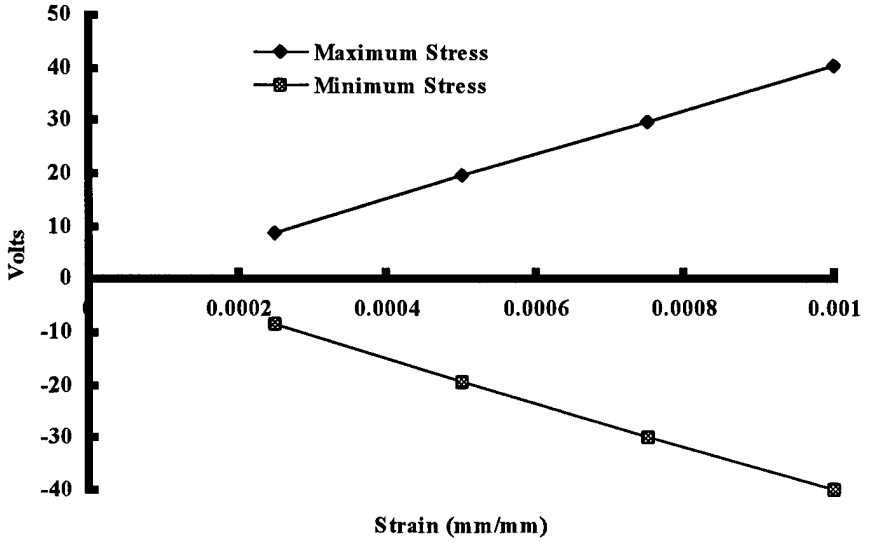

Figure 11. Voltage Output vs Strain - Calibration

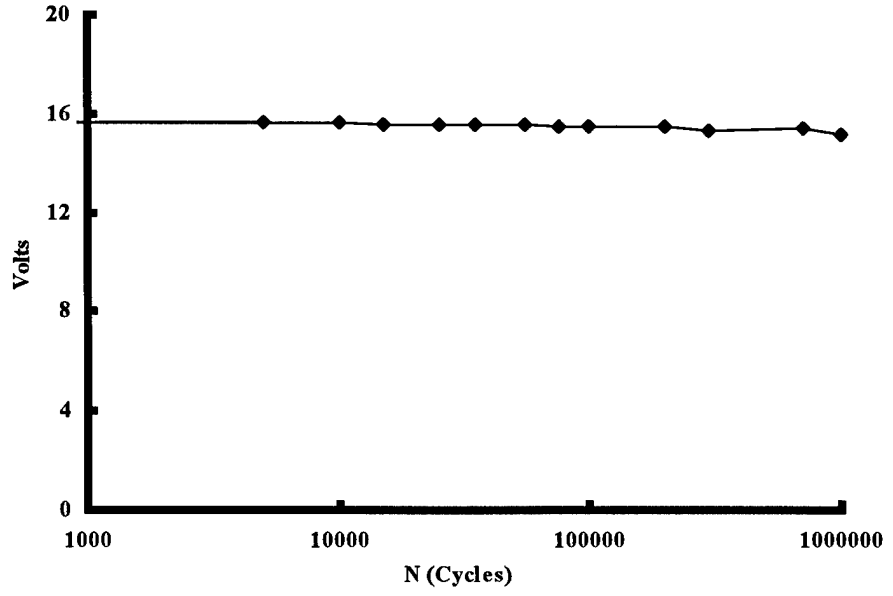

Figure 12. Voltage Output vs Cycles Curve , $\sigma = 25MPa$ and $E = 10V$ to $100V$

ter repoling and before testing. The maximum stress was increased to 50 MPa, while the electric field was kept at 10 V to 100 V. After one million cycles was reached, the voltage output only degraded by 4 %. Figure 13 shows the voltage-cycles relationship for this test. Figure 14 shows how the voltage output remained relatively constant up to one million cycles.

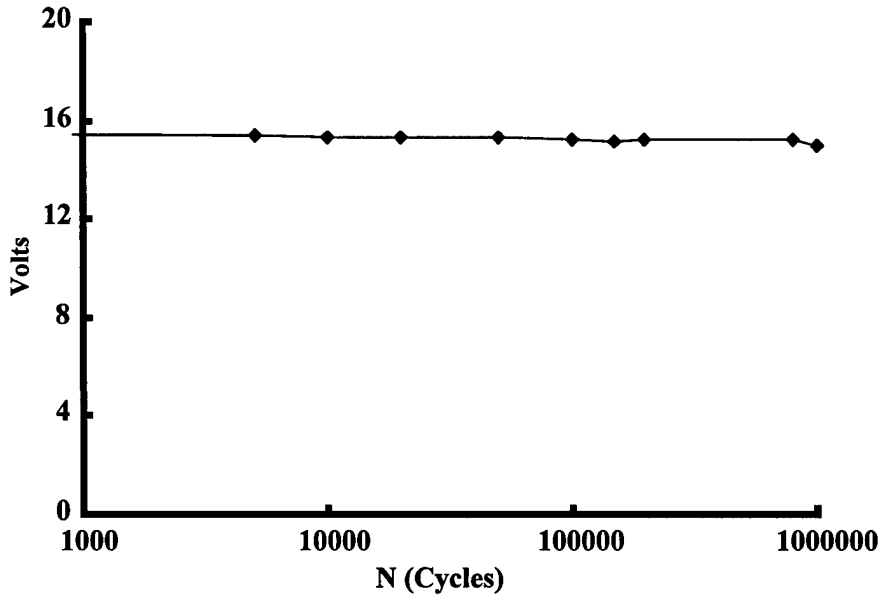

Figure 13. Voltage Output vs Cycles Curve, $\sigma = 50MPa$ and $E = 10V$ to $100V$

Specimen EAF4 was then tested at 75 MPa and an electric field of 10 V to 100 V. The voltage generated by the actuator at this maximum stress level exceeded the MTS console's upper limit, and the specimen was tested above the design strain value suggested by the manufacturer. Therefore, the voltage outputs were taken at 25 MPa before and during cycling. The original voltage output was 19.59 V before testing. A voltage degradation of 10 % was found after only 5,000 cycles. This would indi-

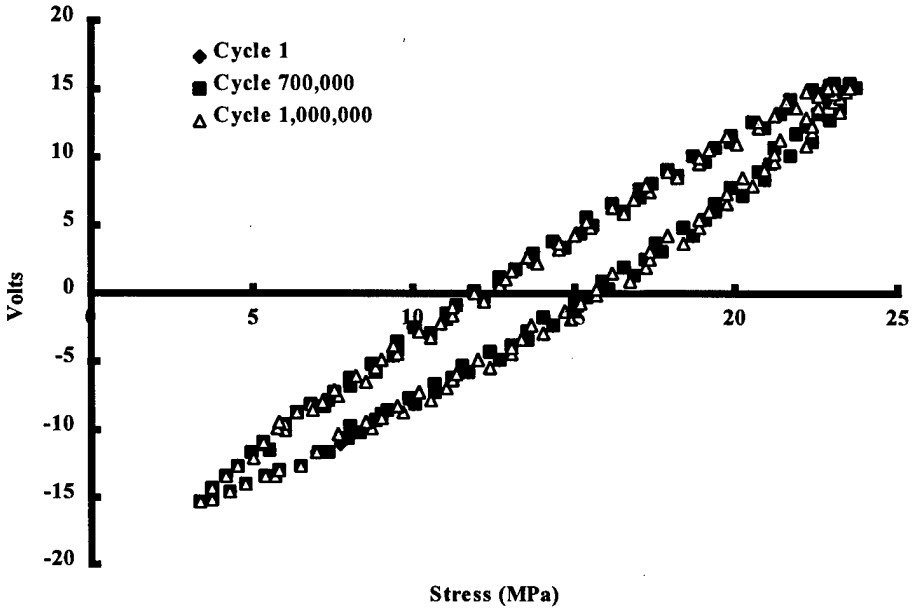

Figure 14. Voltage vs Stress Loops - Specimen EAF1

cate depolarization occurred in the PZT. Since positive voltage input always repoles the embedded PZT, this noticeable degradation might be caused by the mechanical depolarization. The QRMS-II was used to inspect any crack at the edge, but no cracking was found. The capacitance was also found to remain at the same level. As seen in the Figure 15, the voltage degraded with the cycles until one million cycles was reached. The final voltage output was 14.69 V, which was 75 % of the original voltage. Since a value of 15.58 V was measured after repoling, the specimen was considered as undamaged by the failure criterion used in this study. Appendix B shows how the hysteresis formed a closed loop and the change in voltage output before and after repoling.

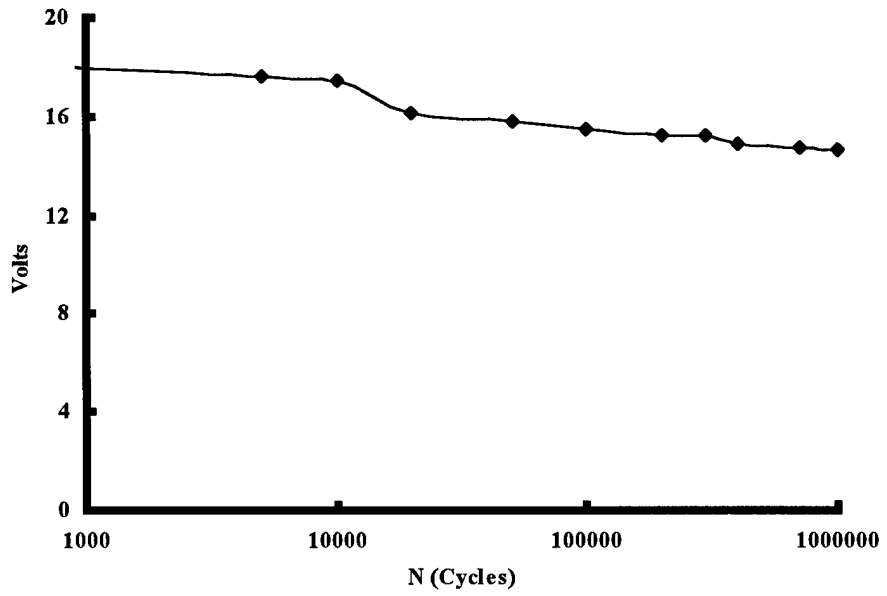

Figure 15. Voltage Output vs Cycles Curve, $\sigma = 75MPa$ and $E = 10V$ to $100V$

Specimen EAF5 was tested at 87.5 MPa and an electric field of 10 V to 100 V. The original voltage output was 19.08 V before testing and dropped by 24 % after 5,000

cycles. After this point, the voltage output degradation continued at a slower rate until 500,000 cycles, where the actuator was repoled according to the repoling criterion, which was applied when the voltage dropped by 50 % of original output. A 74 % voltage recovery was achieved by repoling. However, the PZT voltage dropped by over 50 % after further cycling, indicating permanent damage to the actuator. This specimen failed at 800,000 cycles. The voltage outputs at this instant were 8.47 V and 13.27 V measured before and after repoling , which corresponded to 44 % and 69 % of the original voltage, respectively. Figure 16 shows the voltage output versus cycles curve for this test.

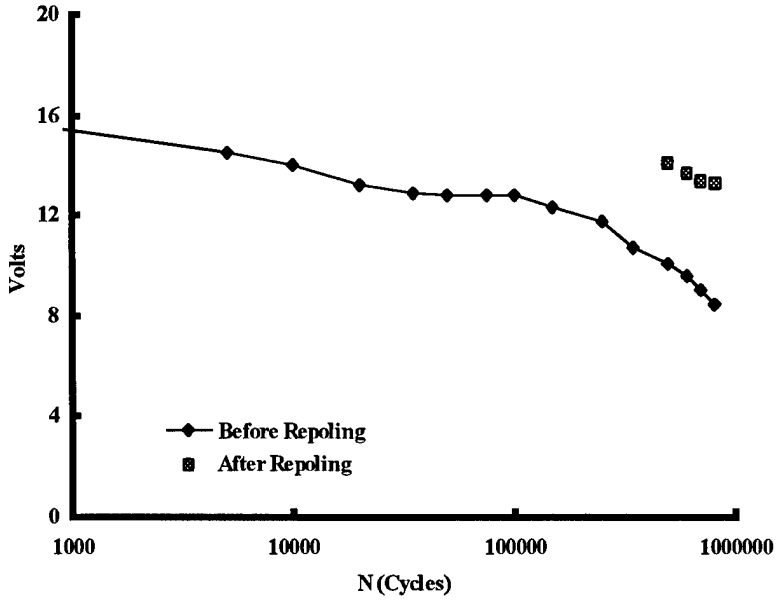

Figure 16. Voltage Output vs Cycles Curve, $\sigma = 87.5MPa$ and $E = 10V$ to $100V$

The maximum stress of the last test in the out-of-phase condition was 100 MPa. Specimen EA4 had a voltage output of 15.13 V before testing. The output dropped by

41 % and 52 % after 5,000 and 10,000 cycles respectively, where the latter resulted in actuator failure by the failure criterion used in this study. The test continued for several thousand cycles beyond actuator failure in order to monitor the voltage degradation after failure. Figure 17 shows the voltage-cycles relationship for this test. This is shown on a linear scale. It can be seen that repoling did not restore the PZT electric response. This would indicate severe damage occurred in the PZT, since it could not be repoled. No cracking was found in this specimen.

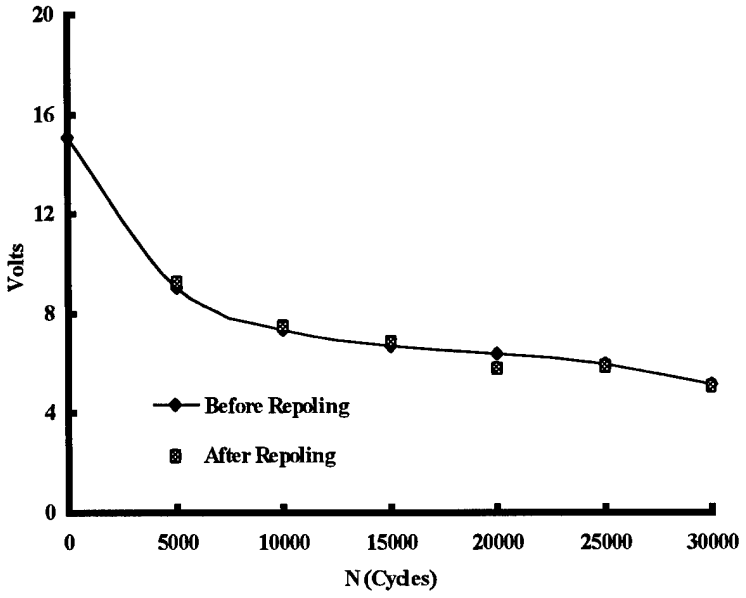

Figure 17. Voltage Output vs Cycles Curve, $\sigma = 100MPa$ and $E = 10V$ to $100V$

Figure 18 shows the voltage output versus cycles curves for all tests conducted under the out-of-phase situation plotted together. The maximum stress level was started with 25 MPa and then gradually increased to 100 MPa, which resulted in a maximum strain of approximately 2000 $\mu\varepsilon$. This strain level was twice the upper limit given by

the manufacturer of the PZT, ACX. At the same time, the applied electric field was kept at 10 V to 100 V, which was repoling the PZT all the time during cycling.

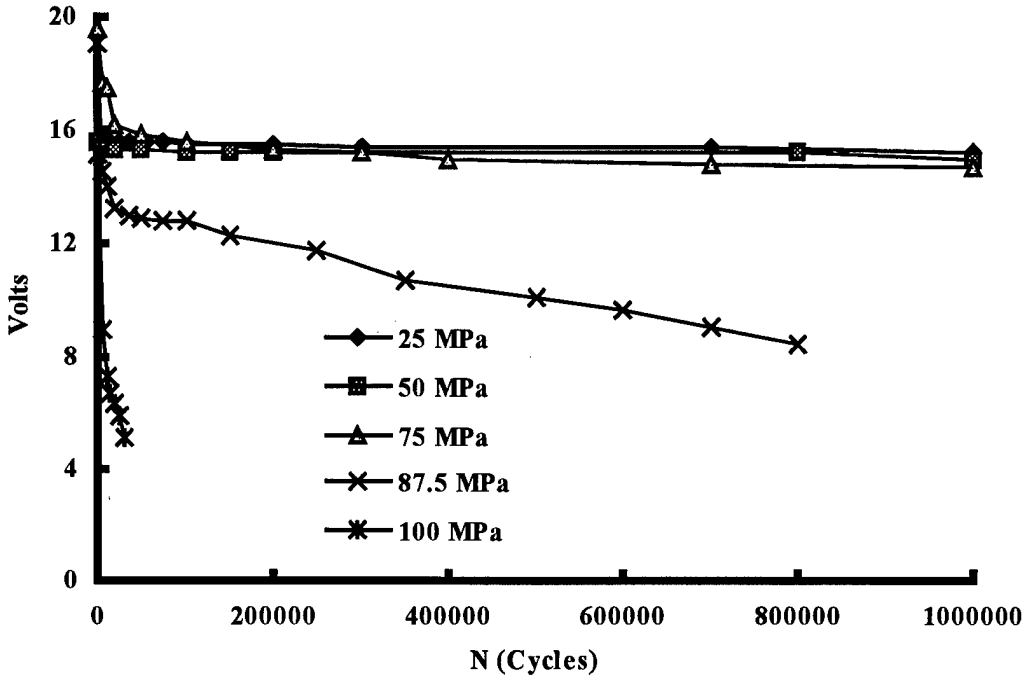

Figure 18. Voltage Output vs Cycles Curves - Out-of-Phase Condition

The voltage-cycles curves in Figure 18 clearly illustrate the dependance of fatigue life on the maximum applied stress level. When the applied stress levels corresponded to the operating strain range of the PZT (up to 50 MPa), the mechanical loading did not cause the depolarization of the actuator. This was expected. Although mechanical loading depolarized actuators at 75 MPa, the positive electric field had a repoling effect on the actuator, that allowed the specimen to survive one million cycles and only caused a voltage drop of 21 % after repoling. After this point, it is clearly seen in fig 18 that the voltage degradation rate of the actuators increased with the maximum applied stress.

Specimens EAF5 and EAF4 were cycled at 87.5 MPa and 100 MPa, which resulted in 24 % and 41 % voltage reduction after 5,000 cycles and caused specimen failure at 800,000 and 10,000 cycles, respectively.

Table 3 shows the results of all tests for the out-of-phase condition. This table includes maximum stress, fatigue life, and voltage output before, during , and after testing. Figure 19 shows the S-N curve of the out-of-phase electro-mechanical fatigue testing.

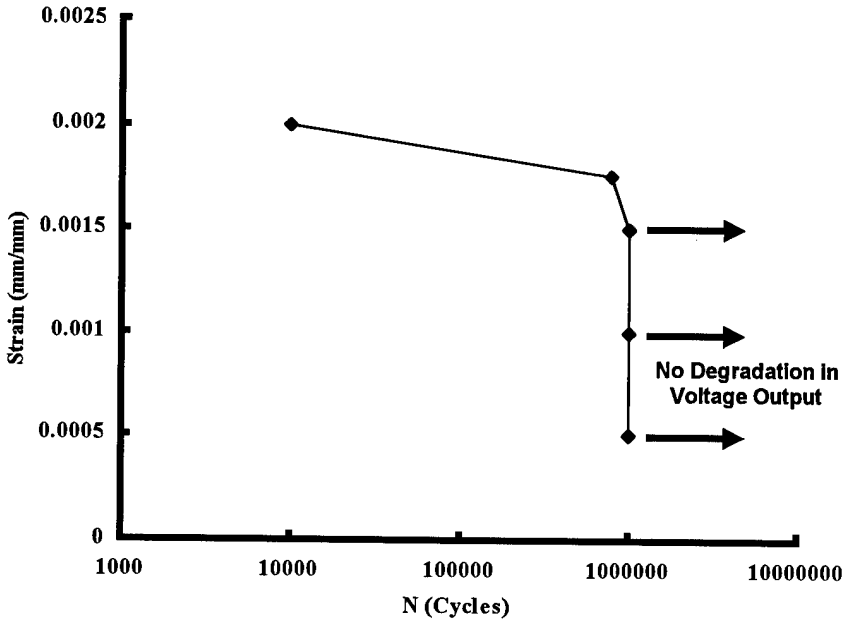

Figure 19. Strain vs Cycles to Failure - Out-of-Phase Condition

4.1.1.2 In-Phase Tests

Specimen EAF2 was first tested at 25 MPa and with a -10 V to -100 V electric field in order to assess the in-phase electrical effect on the actuators. Initially, the volt-

Table 3. Test Summary for Out-of-Phase Condition

Maximum Stress	**Fatigue Life**	**Voltage Output (V)**				
		0 Cycle	**5,000 Cycles**		**Final Cycles**	
			Value	**Reduction**	**Value**	**Reduction**
$\sigma = 25\ MPa$	1,000,000*	15.66	15.66	0	15.18	3 %
$\sigma = 50\ MPa$	1,000,000*	15.53	15.41	1 %	14.98	4 %
$\sigma = 75\ MPa$	1,000,000*	19.59	17.63	10 %	14.69	25 %
$\sigma = 87.5\ MPa$	800,000	19.08	14.53	24 %	8.47	56 %
$\sigma = 100\ MPa$	10,000	15.13	8.98	41 %	7.31	52 %
'$*$' indicates no failure						

age output and capacitance were 17.36 V and 102.8 nF. At the first check point of 5000 cycles, the voltage dropped by 13 % and capacitance fell to 100 nF. Since the mechanical loading was within the operating range of the PZT, the degradation might be primary due to the electrical depolarization. No cracking was found at this time. As cycles increased, the degradation of voltage and capacitance increased as well. Specimen EAF2 survived up to one million cycles with a measured output of 13.81V, which was 80 % of the original voltage. Figure 20 shows the voltage output versus cycles curve.

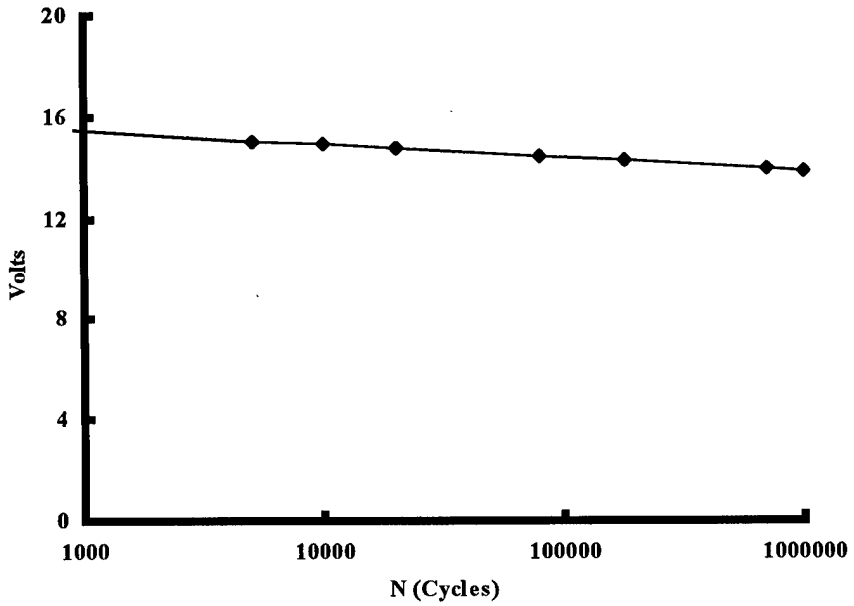

Figure 20. Voltage Output vs Cycles Curve, $\sigma = 25MPa$ and $E = -10V$ to $-100V$

The same specimen was then repoled and a value of 16.62 V voltage output was measured after repoling. The maximum stress was increased to 50 MPa, while the electric field remained at -10 V to -100 V. Electrical depolarization was clearly seen at the first check interval of 5000 cycles, where the voltage and capacitance dropped by 19

% and 4 % respectively. After 100,000 cycles, the specimen was repoled by the repoling criterion. As previously seen in the out-of-phase condition, repolarization did not help in the health recovery of the PZT, since voltage dropped by 50 % after further cycling. The number of cycles to failure for this specimen was 850,000. Figure 21 shows the voltage output-cycles relationship for this test. Figures 22 and 23 show pictures near the PZT location at specimen edge taken at 100,000 and 850,000 cycles. No cracking or delamination was found at the specimen edge.

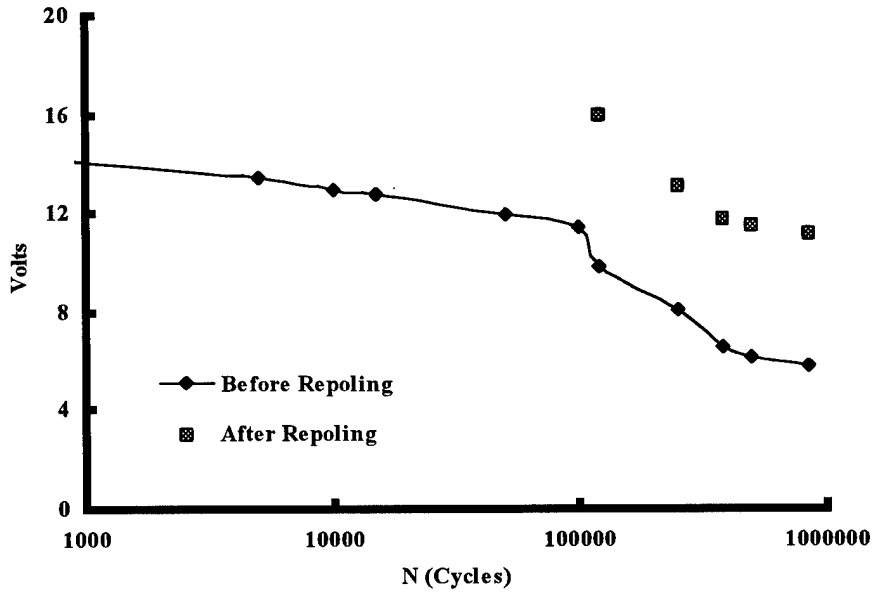

Figure 21. Voltage Output vs Cycles Curve, $\sigma = 50MPa$ and $E = -10V$ to $-100V$

Specimen EAF3 and EAF6 were cycled at 75 and 87.5 MPa respectively, which resulted in a 30 % voltage drop failure after 150,000 and 120,000 cycles. The trends in voltage degradation were very similar for these two specimens. A dramatic voltage reduction occurred after only 5,000 cycles, which was primary caused by mechanical

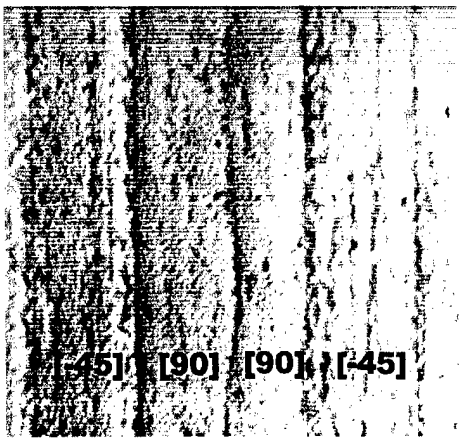

Figure 22. Photomicrograph at PZT Location - 100,000 Cycles, $\sigma = 50MPa$ and $E = -10V$ to $-100V$

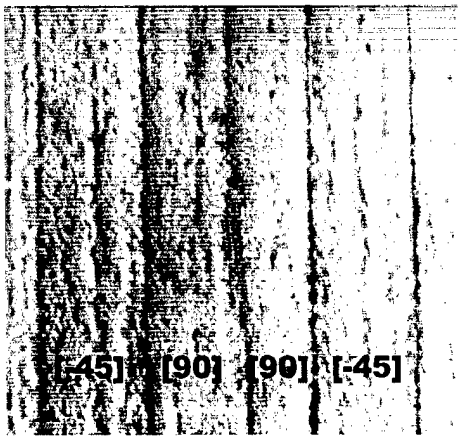

Figure 23. Photomicrograph at PZT Location - 850,000 Cycles, $\sigma = 50MPa$ and $E = -10V$ to $-100V$

depolarization. After this point, the degradation continued gradually until failure. Figures 24 and 25 show the voltage output versus cycles curve for these two specimens.

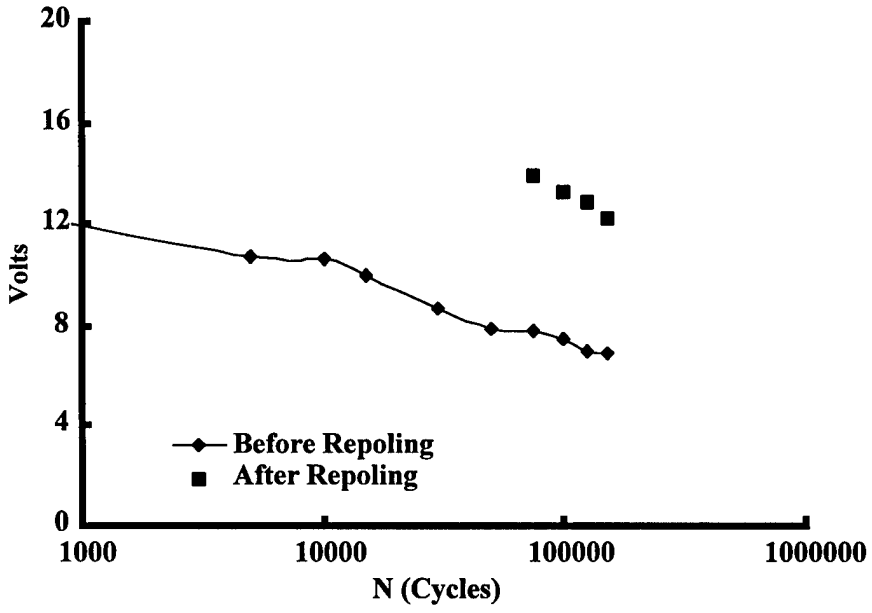

Figure 24. Voltage Output vs Cycles Curve, $\sigma = 75MPa$ and $E = -10V$ to $-100V$

Figure 26 shows the voltage output versus cycles curves for all of in-phase cases plotted together. It can be seen that all voltage output-cycles curves have a sharp voltage reduction after 5,000 cycles. As the applied stress increases, the voltage reduction increases as well. This voltage reduction indicates that piezoelectric damage may have occurred in the actuators. Within the PZT's strain operating range, voltage drop may be caused by the negative electric field excitation which depoled the actuators in the testing. In this operating region, the reductions were within 13 - 19 % of each other after 5,000 cycles and actuators also had longer life. Beyond the recommended strain operating range, voltage reduction saturated approximately at 38 %. At the constant

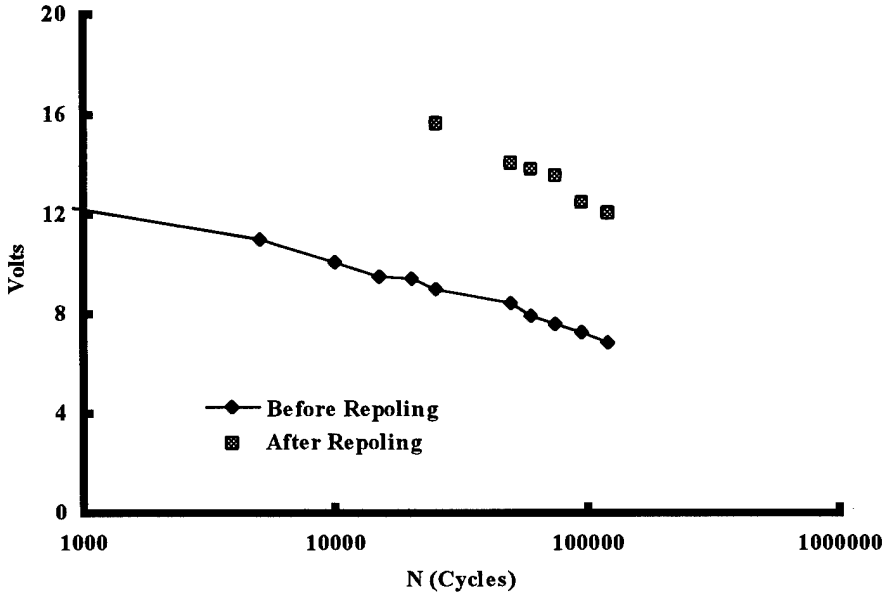

Figure 25. Voltage Output vs Cycles Curve, $\sigma = 87.5MPa$ and $E = -10V$ to $-100V$

electric testing condition, the increasing mechanical loading caused more piezoelectric damage than electrical loading, and actuators had a relatively shorter life than those tested in the recommended strain operating range.

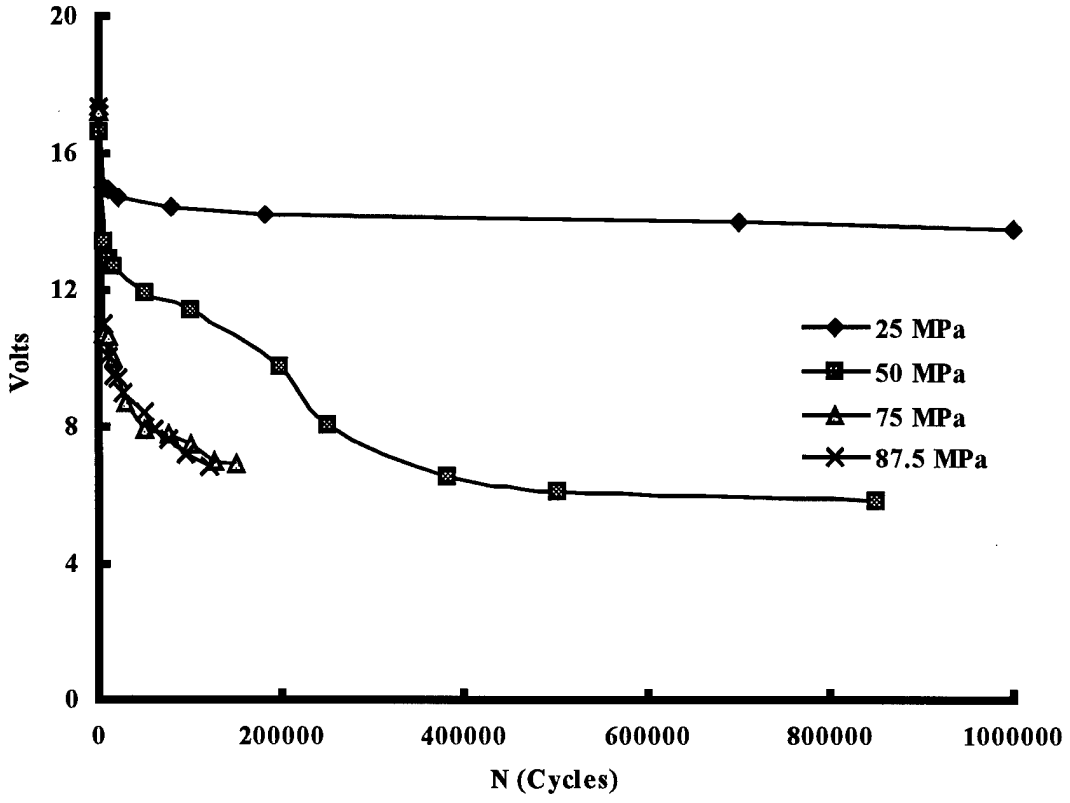

Figure 26. Voltage Output vs Cycles Curves - In-Phase Condition

Table 4 shows the results of all tests for the in-phase condition. This table includes maximum stress, fatigue life, and voltage output before, during, and after fatigue testing. Figure 27 shows the S-N curve of the in-phase electro-mechanical fatigue testing.

Table 4. Test Summary for In-Phase Condition

Maximum Stress	Fatigue Life	Voltage Output (V)				
		0 Cycle	5,000 Cycles		Final Cycles	
			Value	Reduction	Value	Reduction
$\sigma = 25\ MPa$	1,000,000*	17.36	15.03	13 %	13.81	20 %
$\sigma = 50\ MPa$	850,000	16.62	13.42	19 %	5.84	65 %
$\sigma = 75\ MPa$	150,000	17.23	10.73	38 %	6.91	60 %
$\sigma = 87.5\ MPa$	120,000	17.34	11.00	37 %	6.82	61 %
'$*$' indicates no failure						

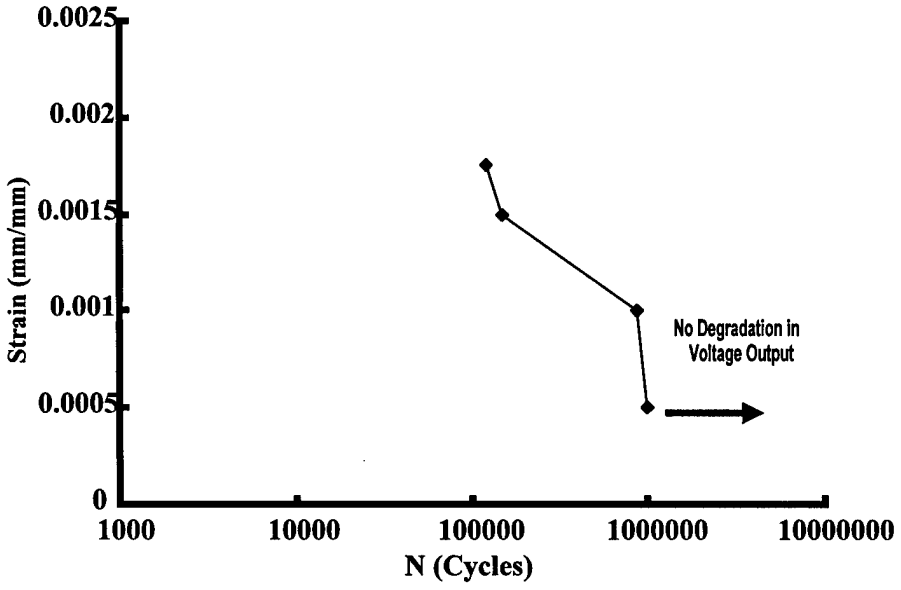

Figure 27. Strain vs Cycles to Failure - In-Phase Condition

4.1.1.3 Low Stress Loading

In order to compare with the results from electro-mechanical loadings on specimens with embedded PZT, four specimens were tested under mechanical loading only. The maximum stress levels for these specimens were 50, 75, 87.5 and 100 MPa. In general, the voltage degradation trends of actuators under mechanical loading were very similar to those in the out-of-phase condition. At 50 and 75 MPa, the actuator's voltage output degraded 6 % and 37 % after one million cycles, respectively, which were only higher by 2 - 12 % than the actuators tested at the same stress levels in the out-of-phase condition. When the maximum stress was increased to 87.5 MPa, specimen EAF9 survived up to one million cycles, and the voltage output dropped by 39 % and 25 % before and after repoling. However, this result was slightly different than expected, since the specimen tested at the same level in the out-of-phase condition had to be repoled after 500,000 cycles and finally failed at 800,000 cycles. One explanation would be due to the natural variation in each actuator's material properties. At the highest maximum stress tested in this part of testing, 100 MPa, an immediate sharp drop of voltage output was seen after only 5000 cycles, and the actuator was considered failed at 10,000 cycles by the failure criterion used in this study. As seen also in the out-of-phase condition, at this stress level repoling did not restore the voltage output after the PZT failed. Figures 28, 29, 30, and 31 show the voltage output versus cycle curves at 25, 50, 75, and 100 MPa, respectively. Figure 32 shows the voltage output versus cycles curves for all tests of low stress case plotted together

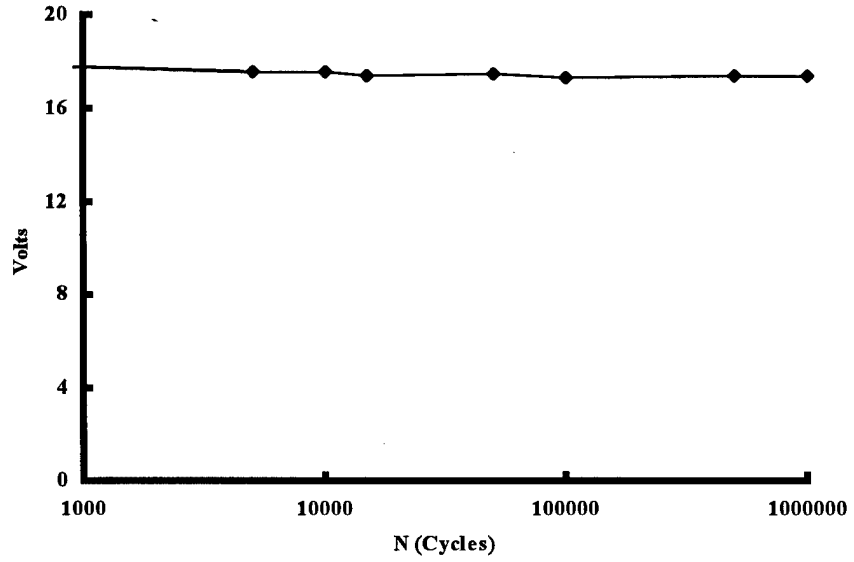

Figure 28. Voltage Output vs Cycles Curve, $\sigma = 50MPa$

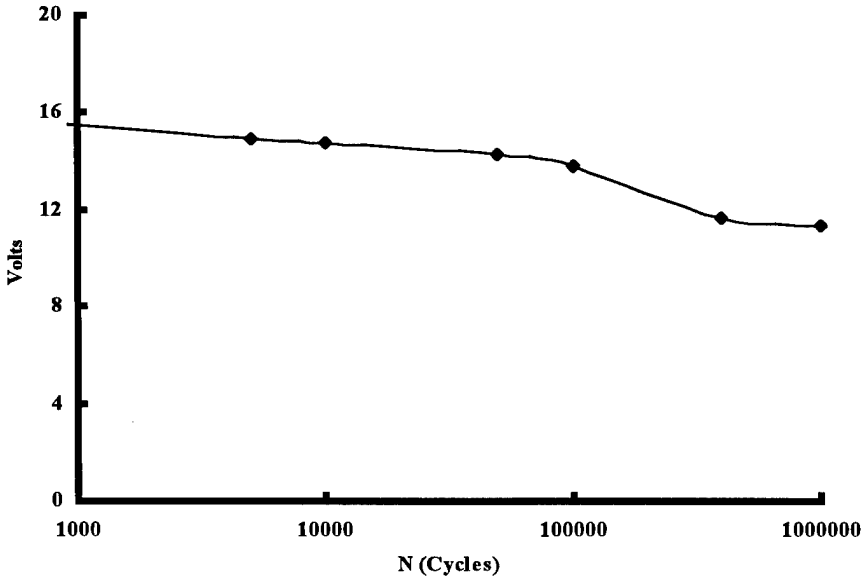

Figure 29. Voltage Output vs Cycles Curve, $\sigma = 75MPa$

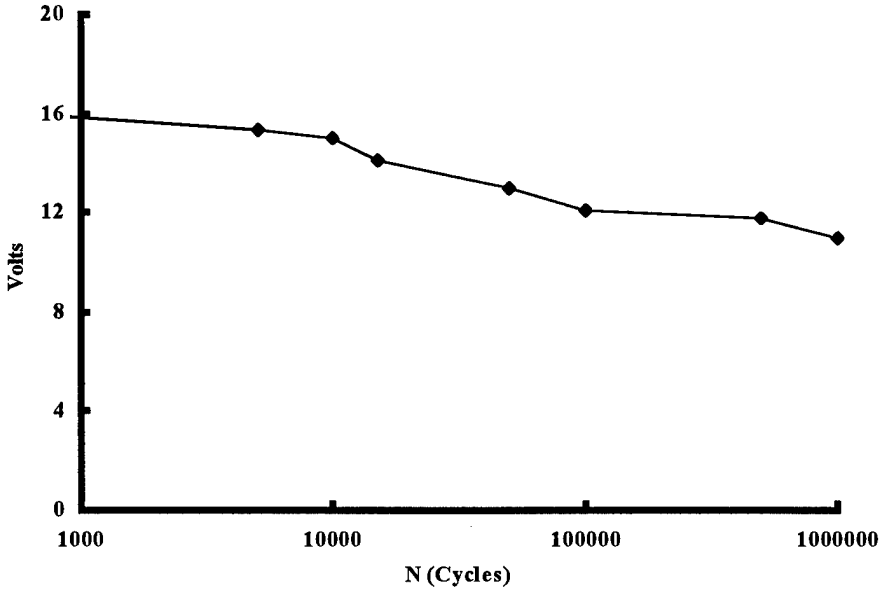

Figure 30. Voltage Output vs Cycles Curve, $\sigma = 87.5MPa$

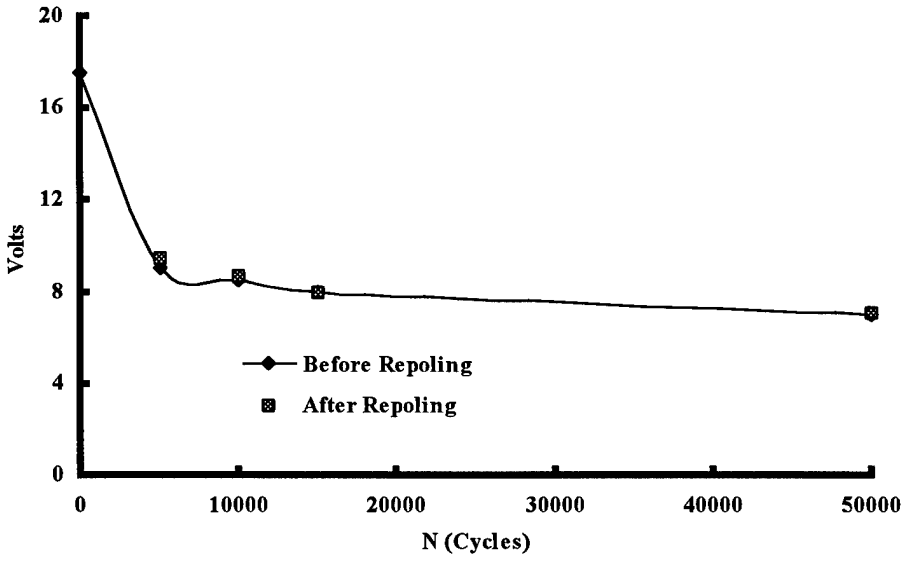

Figure 31. Voltage Output vs Cycles Curve, $\sigma = 100MPa$

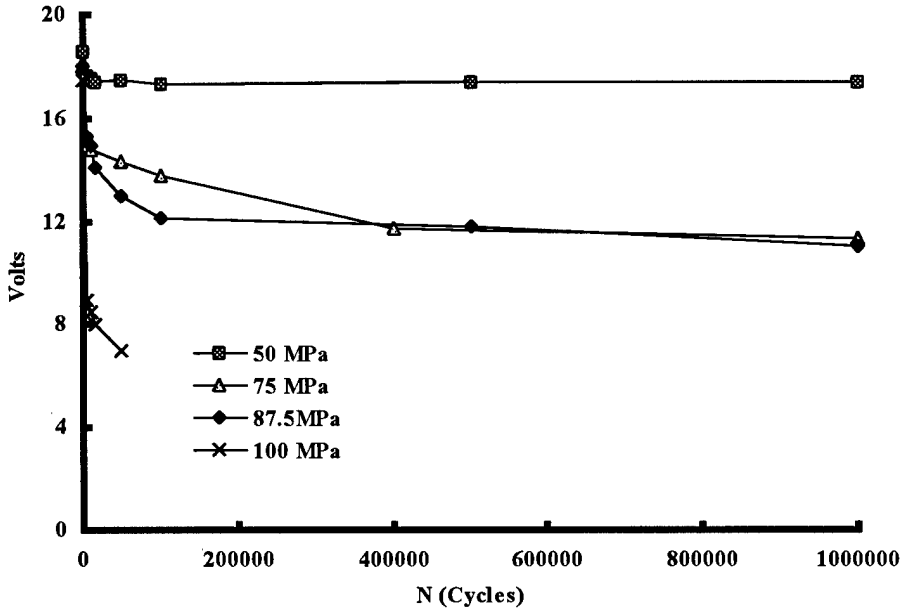

Figure 32. Voltage Output vs Cycles Curves - Low Stress Condition

Table 5 shows the results of all tests under the low stress condition. This table includes maximum stress, fatigue life, and voltage output before, during, and after fatigue testing. Figure 33 shows the S-N curve of the low stress fatigue testing.

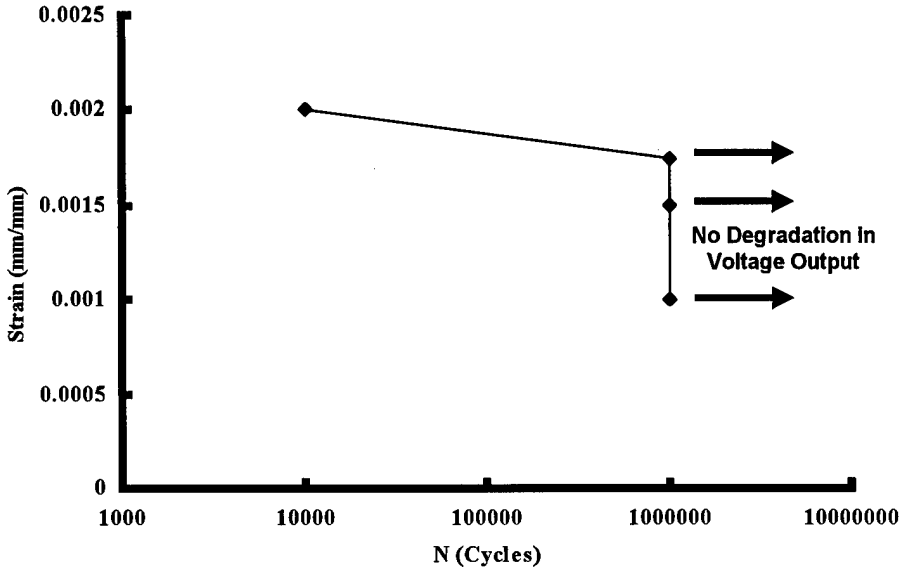

Figure 33. Strain vs Cycles to Failure - Low Stress Condition

4.1.2 Comparison

4.1.2.1 Voltage Output

In order to compare the response of PZTs under out-of-phase and in-phase excitation condition, results of voltage degradation for these two conditions are compared at the same stress level. Figures 34, 35, 36, and 37 show the voltage output-cycles relationship for out-of-phase and in-phase conditions at 25, 50, 75, and 87.5 MPa, respectively. The voltage degradation curves for low stress condition were also shown in some figures for comparison purpose.

Table 5. Test Summary for Low Stress Condition

Maximum Stress	Fatigue Life	Voltage Output (V)				
		0 Cycle	5,000 Cycles		Final Cycles	
			Value	Reduction	Value	Reduction
$\sigma = 50\ MPa$	1,000,000*	18.55	17.61	5 %	17.40	6 %
$\sigma = 75\ MPa$	1,000,000*	18.00	14.94	17 %	11.34	37 %
$\sigma = 87.5\ MPa$	1,000,000*	18.00	15.3	15 %	11.02	39 %
$\sigma = 100\ MPa$	10,000	17.52	9.10	48 %	8.51	52 %
'$*$' indicates no failure						

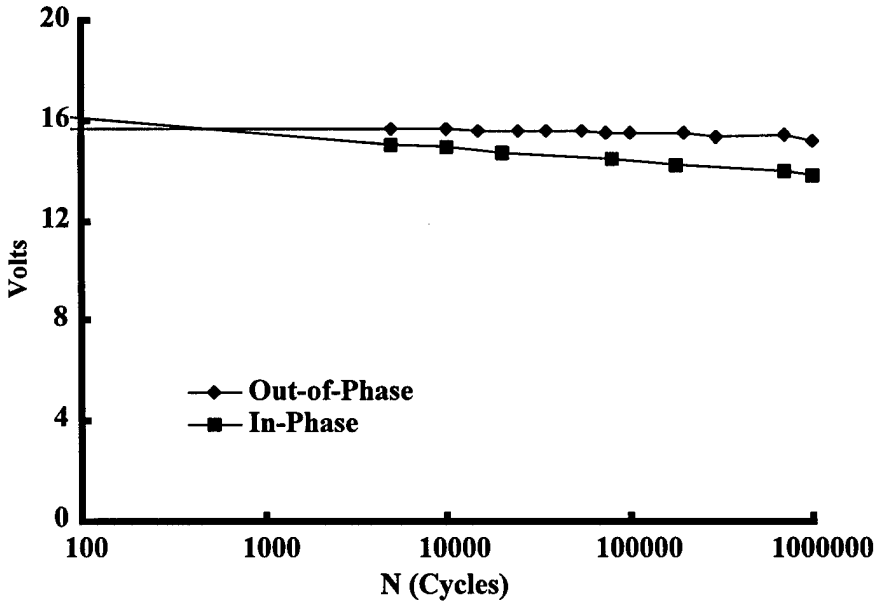

Figure 34. Voltage Output vs Cycles Curves - Out-of-Phase and In-Phase Conditions, $\sigma = 25MPa$

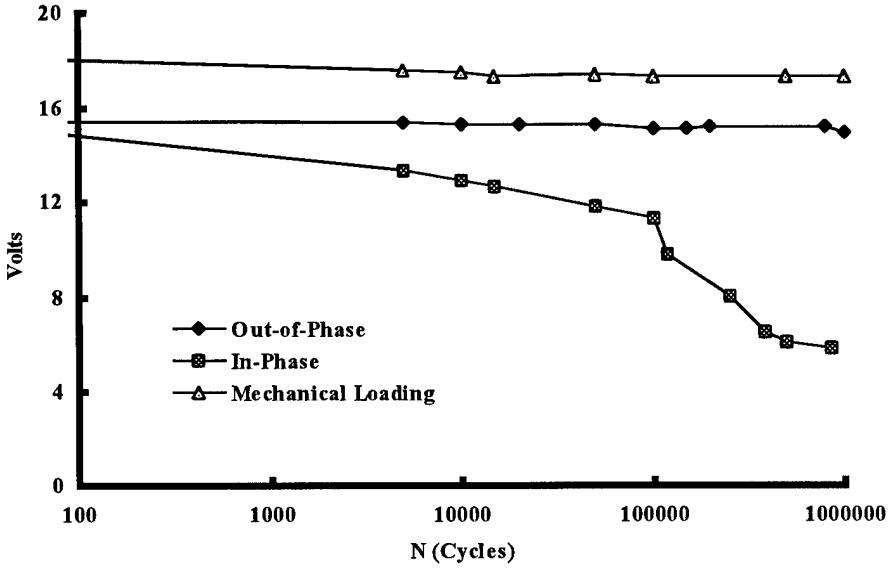

Figure 35. Voltage Output vs Cycles Curves - All Conditions, $\sigma = 50MPa$

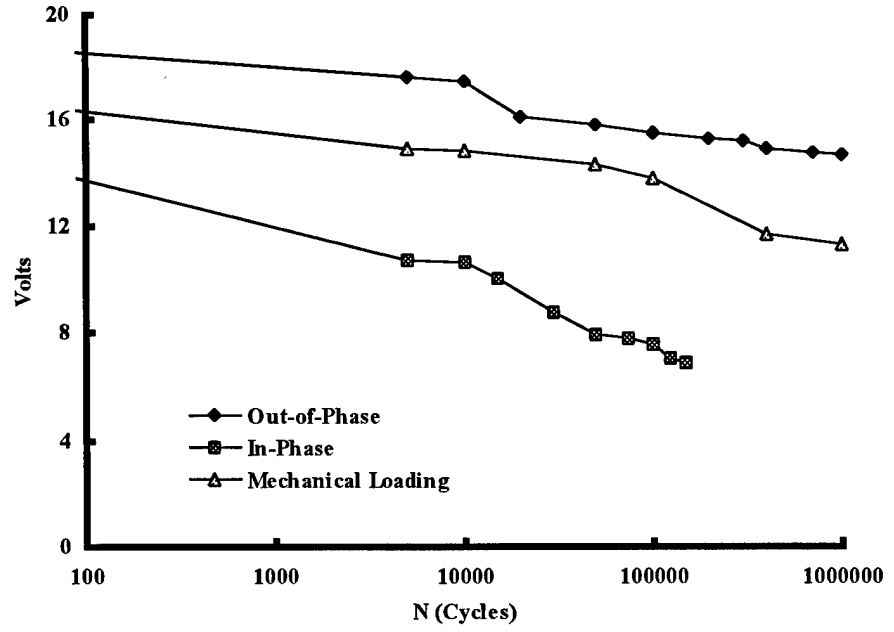

Figure 36. Voltage Output vs Cycles Curves - All Conditions, $\sigma = 75MPa$

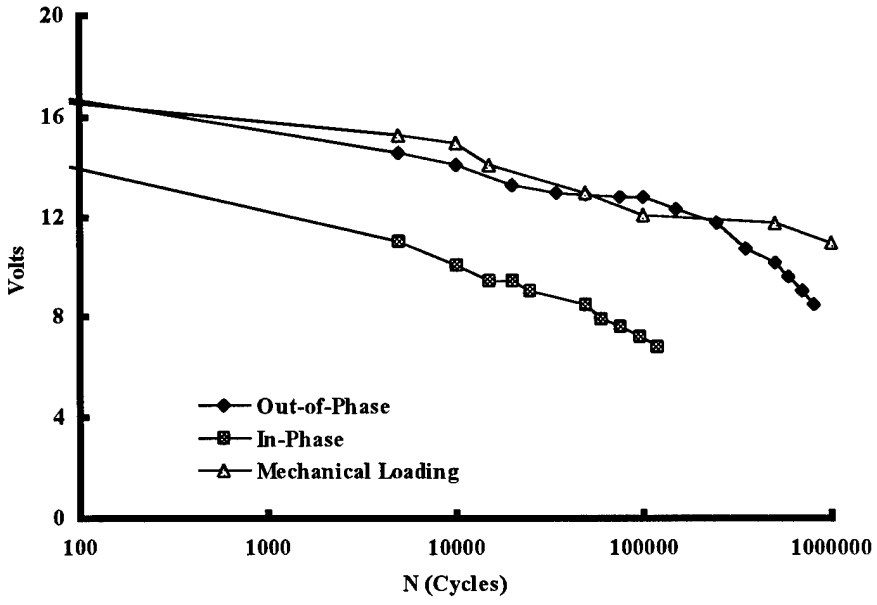

Figure 37. Voltage Output vs Cycles Curves - All Conditions, $\sigma = 87.5MPa$

It can be seen very clearly that at a given maximum stress level, the out-of-phase condition has a flatter curve than the in-phase condition. A flat curve represents a longer fatigue life and less voltage reduction. The in-phase condition had a final voltage reduction of 20 % and 65 % at 25 and 50 MPa, while the voltage reductions were 3 % and 4 % in the out-of-phase condition, respectively. Electrical depolarization is the primary reason to account for the voltage reduction at these stress levels.

When the applied stress was increased to 75 MPa, the voltage output dropped by over 40 % in in-phase condition. At this stress level, the voltage reduction was caused by a combination of mechanical and electrical depolarization. However, the mechanical loading had more influence on the performance of PZTs than electrical loading even in the in-phase condition.

At different stress levels, the voltage output-cycles curves exhibited a different degradation rate for the two conditions. The voltage degradation for out-of-phase condition remained a flat curve at 25 MPa and 50 MPa, while the slope started decreasing at 25 MPa during in-phase testing. The voltage degradation curve for in-phase testing seemed to keep a constant slope at 50 MPa. Finally, the voltage degradation curves had approximately the same slope for both conditions. The change of voltage degradation rate for both conditions showed again that the performance of the PZTs were dominated by the maximum applied stress after specimens were strained beyond the PZT's operating range.

As mentioned earlier, the trends in voltage degradation were very similar for out-of-phase and low stress conditions. Up to the strain limit, the voltage reductions after one

million cycles was 2 % for out-of-phase and low stress conditions, and the difference was 12 % at 75 MPa, which was attributed to the electrical repolarization effect in the out-of-phase condition. However, as the maximum stress increased, the mechanical loading had more influence on the performance of actuators. Figure 38 shows the voltage degradation curves for out-of-phase and low stress conditions at 100 MPa. It can be seen that a sharp voltage output drop occurred after only 5,000 cycles and the embedded actuators failed at 10,000 cycles for both conditions.

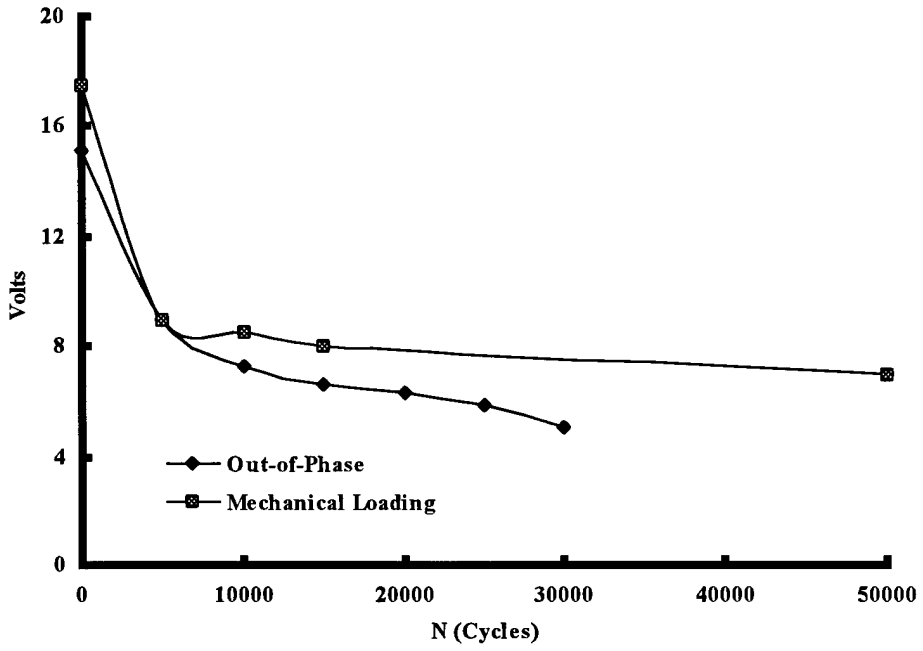

Figure 38. Voltage Output vs Cycles Curves - Out-of-Phase and Low Stress Conditions, $\sigma = 100MPa$

4.1.2.2 S-N Curve

Figure 39 shows the S-N relation for the out-of-phase, in-phase, and low stress conditions. As discussed before, at all stress levels, PZTs had a better performance

in out-of-phase testing than in in-phase testing. Since the actuator was repolarized all the time during cycling in out-of-phase condition, the actuator did perform very well at different stress levels, except at 100 MPa, where it failed after 10,000 cycles. For in-phase testing, the actuator also showed a good performance within the actuator's operating strain range. As the applied stress exceeded the upper strain limit, a sharp drop-off showed in its S-N curve.

In general, the actuators did perform very well during cycling up to the manufacturer's design limit of 1000 $\mu\varepsilon$ for out-of-phase and low stress conditions, while the actuator failed after 850,000 cycles in in-phase testing due to the electrical depolarization effect. Above this limit, a sharp drop-off occurred in the S-N curve of the in-phase condition which was primarily attributed to the mechanical depolarization. As the maximum stress increased, the mechanical loading caused more damage in the actuators. Finally, the actuators failed quickly after only 10,000 cycles at 100 MPa for the low stress and out-of-phase conditions.

4.1.2.3 Capacitance Measurement

All capacitance measurements were taken at zero stress levels at every instant when voltage was measured. The out-of-phase and in-phase fatigue tests showed different trends in capacitance change with cycles. As cycles increased, capacitance measurements steadily increased in the out-of-phase condition. On the other hand, capacitance measurements steadily decreased with increasing cycles in in-phase testing. In all tests, capacitance went back to the original value after repolarization, even though voltage

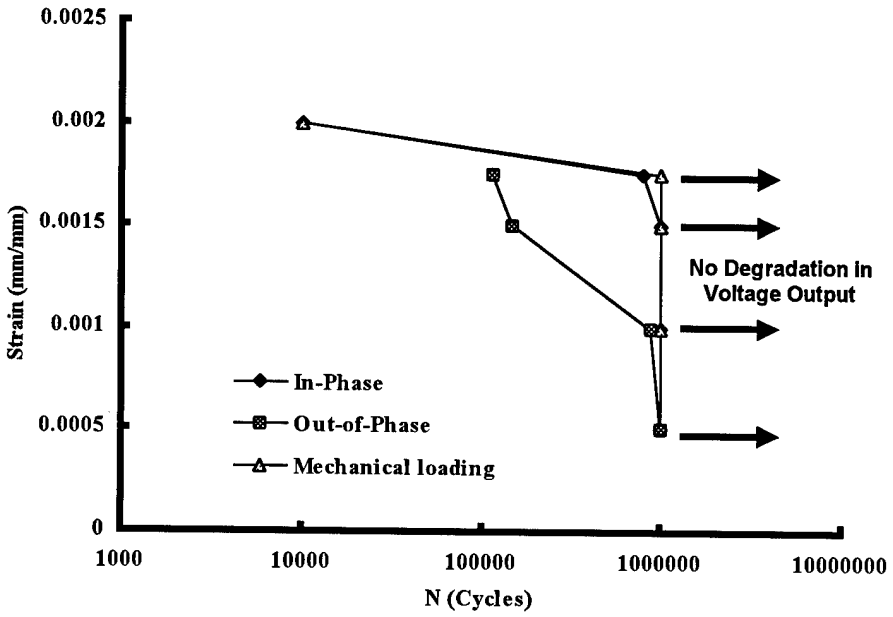

Figure 39. Strain vs Cycles to Failure - All Conditions

output showed damage occurred in the PZTs. Figures 40 and 41 show the capacitance versus cycles curve for out-of-phase and in-phase conditions.

Theoretically, several factors are involved in the change of capacitance measurement. The relations between these factors can be seen in Equation (15). K_3^T is the dielectric constant, ε_0 is the permittivity of the free space, l is the length, w is the width, and t is the thickness of the capacitor.

$$\text{Plate Capacitance } (F) = \frac{K_3^T * \varepsilon_0 * l * w}{t} \tag{15}$$

The applied mechanical loading and electric field will both change the dimensions of the PZTs. However, from the strain gauge data, the electrical strain was much less than the mechanical strain during cycling, especially at higher stress levels. From Figures 40 and 41 it can be seen that, at the same stress level, capacitance measurements exhibited the opposite trends in out-of-phase and in-phase conditions. Hence, capacitance was influenced by a change of the $K_3^T * \varepsilon_0$ in Equation (15), which is related to the direction of the electric field. Positive electric field excitation caused increasing capacitance measurement during cycling. Negative electric field excitation caused decreasing capacitance measurement during cycling. The relation between $K_3^T * \varepsilon_0$ and electric field is not fully understood and is beyond the scope of this study.

4.1.2.4 Damage Assessment

Ultrasonics and strain gages were used to analyze damage if it occurred at the interface between the PZTs and the laminates. Two specimens, EAF3 and EAF4, were sent to UDRI for ultrasonic inspection after testing. Specimen EAF3 was tested at 75

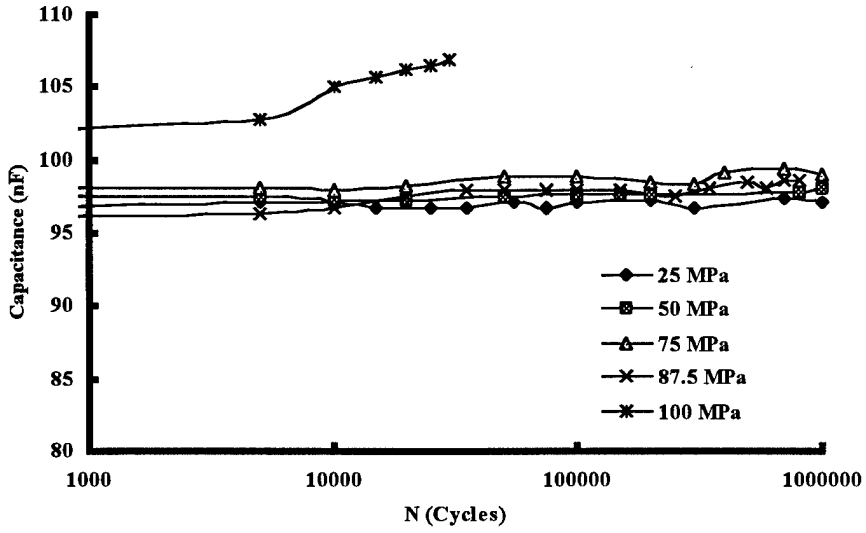

Figure 40. Capacitance vs Cycles Curves - Out-of-Phase Condition

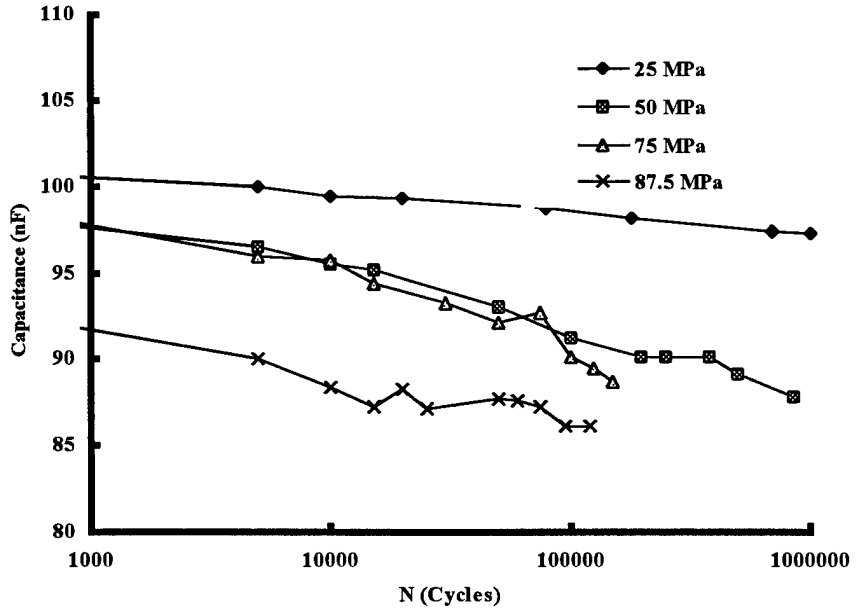

Figure 41. Capacitance vs Cycles Curves - In-Phase Condition

MPa under the in-phase condition, and the embedded PZT failed after 150,000 cycles, while specimen EAF4 survived up to one million cycles at the same stress level under the out-of-phase condition. The results of ultrasonic inspection showed no damage in these two specimens, as seen in Figure 42. On looking at the data recorded from the strain gage of specimen EAF3 in Figure 43, there is no noticeable change in strain data to indicate the health of the PZT and laminate. Table 6 provides the maximum and minimum strains for all out-of-phase and in-phase testing. It is also shown that electrical strain is much less than mechanical strain by comparing strain data at the same stress level in two conditions.

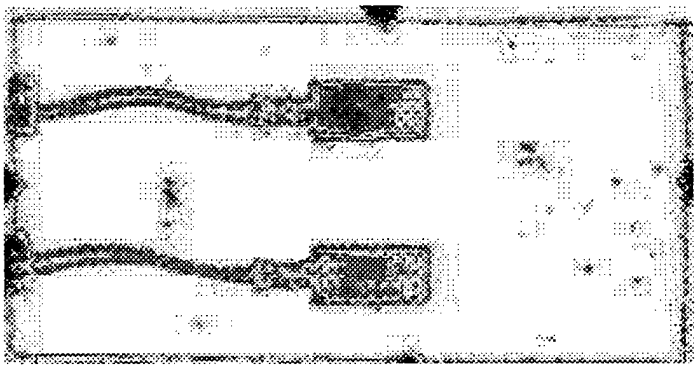

Figure 42. C-Scan Photograph of Specimens EAF3 and EAF4

Table 6. Strain Data for Out-of-Phase and In-Phase Conditions

Test Types	Maximum Stress	Maximum Strain	Minimum Strain
Out-of-Phase	25 MPa	525 $\mu\varepsilon$	98 $\mu\varepsilon$
	50 MPa	1075 $\mu\varepsilon$	209 $\mu\varepsilon$
	75 MPa	1604 $\mu\varepsilon$	269 $\mu\varepsilon$
	87.5 MPa	1848 $\mu\varepsilon$	322 $\mu\varepsilon$
	100 MPa	2112 $\mu\varepsilon$	409 $\mu\varepsilon$
In-Phase	25 MPa	585 $\mu\varepsilon$	110 $\mu\varepsilon$
	50 MPa	1181 $\mu\varepsilon$	254 $\mu\varepsilon$
	75 MPa	1698 $\mu\varepsilon$	302 $\mu\varepsilon$
	87.5 MPa	1952 $\mu\varepsilon$	346 $\mu\varepsilon$

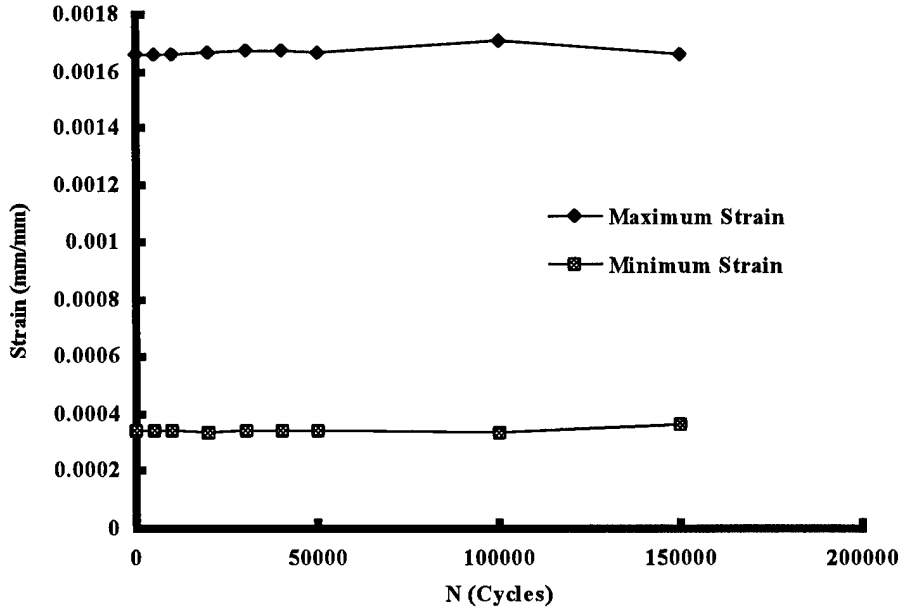

Figure 43. Strain vs Cycles Curve - Specimen EAF3

4.2 High Stress Loading

The second objective of this study was to investigate the monotonic and fatigue loading behavior of $[0/0/+45/-45/0/0/90]_S$ laminate with an embedded PZT. Coleman has shown that "It is possible to embed PZT inside $[0/+45/-45/90]_S$ laminate without significantly affecting the tensile strength and fatigue life of the composite [4]", and he also did preliminary study on the $[0/0/+45/-45/0/0/90]_S$ laminate. The study of this chapter will continue the research on the $[0/0/+45/-45/0/0/90]_S$ laminate and focus on the mechanical fatigue effects, such as Young's modulus, delamination, transverse crack density, and fatigue life.

The result of the monotonic and fatigue loading, including crack density, the degradation of modulus and delamination are discussed in this section. Furthermore, comparisons of the S-N curve between present work with $[0/0/+45/-45/0/0/90]_S$ and previous work with $[0/+45/-45/90]_S$ are presented in the last part of this chapter.

4.2.1 Monotonic Loading

The objective of the monotonic load test was to characterize the static behavior of the $[0/0/+45/-45/0/0/90]_S$ laminate and its ultimate strength that was then used to get stress level estimates for the fatigue tests. These tests were completed by calculating loading rate based upon an expected ultimate strength and a maximum testing time limit of 60 seconds. Two specimens, MM1 (without PZT) and MA1 (with PZT), were monotonically loaded in tension to failure. A extensometer was attached to the middle portion of the specimen to measure the average strain across the entire actuator length.

4.2.1.1 Stress-Strain Response

In order to compare the stress-strain response of specimens with and without PZT, Figure 44 shows the stress-strain curves for specimens MM1 and MA1 under uniaxial tensile loading. MM1's stress-strain curve initially has a constant slope, but tends to start curving downward at 500 MPa. After this point, the slope bends more noticeably downward at 700 MPa. These changes in slope represent increasing damage in the specimen. The final failure for MM1 occurred at 960 MPa. The same stress-strain response was then measured for MA1, and its results are overlaid upon MM1 in Figure 44. The MM1 and MA1 curves mimic each other almost exactly in the beginning of the testing, bending downward almost along the same path. The most notable difference between these was the slightly lower ultimate strength of MA1, which was 940 MPa. The ultimate strength and modulus of specimen MM1 and MA1 were within 2 % of each other, which is not significant considering the relatively large embedded PZT.

The noticeable shifts in the stress-strain curves and the corresponding changes in modulus correspond to transverse cracking, FPF, $\pm 45°$ plies failure, and other progressive delamination and axial cracking. Theoretical changes in modulus due to the failure of plies were estimated via Ply-Discount Method. The changes in the experimental modulus after these noticeable shifts were calculated for comparison. Experimentally, FPF occurred at approximately 500 MPa, where the modulus decreased by approximately 2.2 %. The shift at 700 MPa corresponded to increasing damage in the 45° plies, where the modulus decreased by 7.6 %. Theoretically, the decrease in modulus after the -45° plies failed was 5.9 %. Table 7 compares the calculated shifts from the the-

oretical Ply-Discount method versus the experimental shifts in the stress-strain curve. The Ply-Discount method can be somewhat inaccurate, since it does not take into consideration about the complicated laminate damage properties, but it does give a good estimate of damage progression.

4.2.1.2 Damage Mechanism

Specimen MM1 and MA1 had similar transverse failure modes and limited edge delamination. During the monotonic loading test, the specimens were stressed to fail within 60 seconds, so the damage sequence occurred very rapidly. Figures 45 and 46 show the failed specimen and the edge delamination of MA1, respectively. In general, these specimens had a lesser amount of delamination damage than found during fatigue testing, but compared very well with each other. As discussed in the stress-strain response section, FPF and subsequent ply failures were approximated by the change in the stress-strain curve's slope.

4.2.2 Fatigue Behavior

The goal of the fatigue test was to establish a fatigue limit, to establish the S-N curve, and to study the damage and failure mechanisms. As can be seen in Table 8, four MF specimens (without embedded PZT) and three MAF specimens (with PZT) were

Table 7. Theoretical vs Experimental Young's Modulus (MM1)

Remarks	Theoretical (GPa)	Decrease (%)	Experimental (GPa)	Decrease (%)
Before Damage	92.03	-	86.5	-
90° Ply Failure	90.63	1.6	84.65	2.2
-45° Ply Failure	86.61	5.9	79.93	7.6

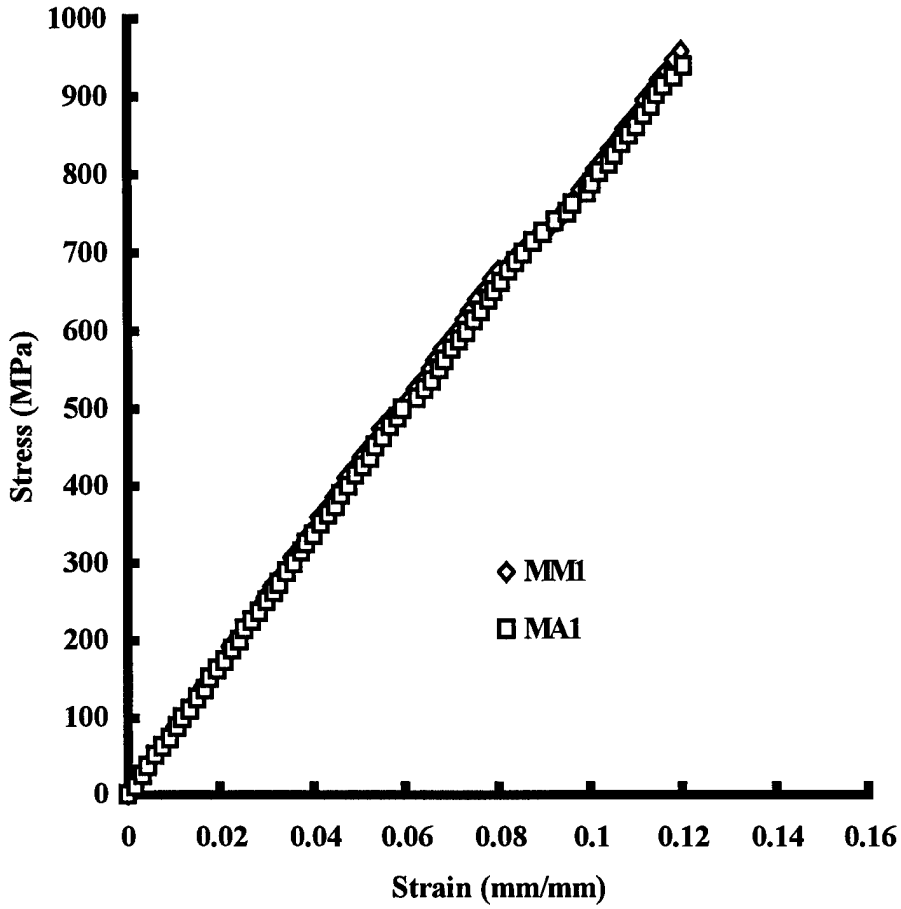

Figure 44. Stress-Strain Curves for Specimens MM1 and MA1

Figure 45. Failure of Specimen MA1 under Monotonic Loading

Figure 46. Specimen MA1 - Edge Delamination under Static Loading

tested under tension-tension cyclic loading with an R value of 0.1 and a frequency of 10 Hz.

Fatigue behavior of composite material is a complex phenomenon. As mentioned in Chapter two, in general, the progressive development of fatigue life can be divided into five stages: matrix cracking, fiber/matrix debonding, delamination initiation, delamination growth, and specimen fracture [12]. Similar behavior was also found in this study. The results of tests can be broken into different subsections discussing S-N curve, damage mechanisms, Young's modulus, and width of delamination. The following subsections will provide the detailed discussion of these results.

4.2.2.1 S-N Curve

The S-N curve is expressed by the maximum applied stress as a function of the number of fatigue cycles causing specimen failure. Several stress levels were chosen so that fatigue life ranged between 10^3 and 10^6 cycles [13]. The MF specimens (without PZT) were tested before MAF (with PZT) specimens in order to establish the basic S-N curve of the laminate without PZT. The first fatigue test was conducted at 760 MPa which was selected to be 75 % of the ultimate strength and corresponded to a fatigue life 16,383 cycles. The next three tests of MF specimens were run at 700,660, and 600 MPa. Only MF4 (600 MPa) survived up to 2 millions cycles; see Table 8. In order to compare the fatigue life between specimens with and without PZT embedded in the laminate, MAF1 was tested at the same stress level as MF2. The result revealed that MAF1 had a better performance in fatigue life than MF2. Specimen MAF2 also followed this trend.

Table 8. Summary of Fatigue Tested Specimens

Specimen Number	**Maximum Stress(MPa)**	**Cycles to Failure**	**Remark**
MF1	760	16383	Without PZT
MF2	700	302794	
MF3	660	729760	
MF4	600	2000000*	
MAF1	700	1472029	With PZT
MAF2	740	180881	
MAF3	552	2000000*	
'*' indicates no failure			

Figure 47 shows the S-N curve with data from all specimens with and without PZT. Figure 48 is a magnified view of a portion of Figure 47 and gives a much clearer picture. In summary, two things were observed from the fatigue life diagram. First, the slope of the S-N curve was rather small. It indicated this lay-up was a fiber-dominated one, because matrix dominated laminates would have a more noticeable drop-off. Another thing is that at same stress levels the PZT embedded specimens sustained slightly longer life under cyclic loading than specimens without embedded PZTs. One explanation may be due to the location of the PZT and damage mechanism differences in these specimens. Another explanation would be statistical variation due to uncertainties. Overall, the differences were not very significant, since the data generally fell on the same S-N curve.

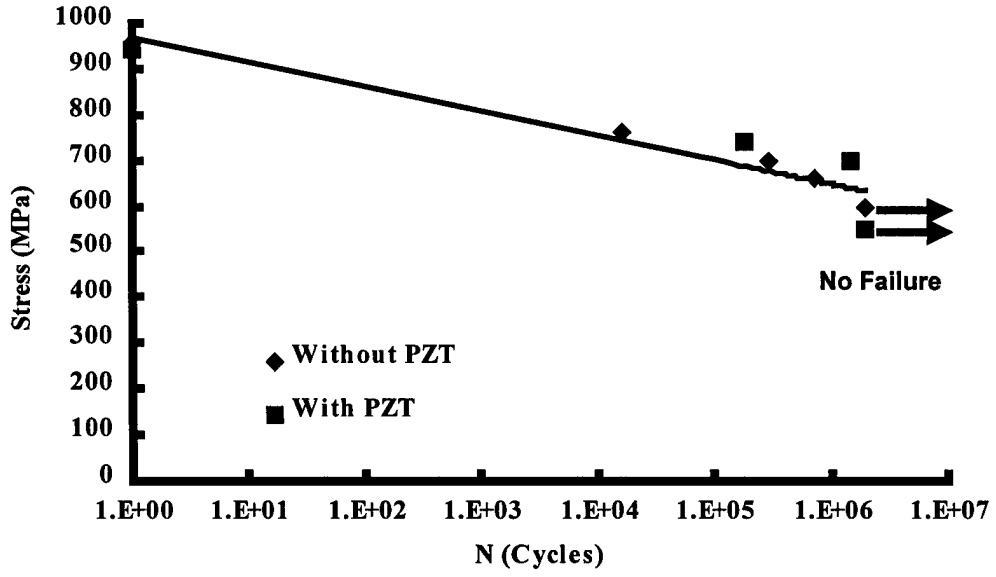

Figure 47. S-N Curve

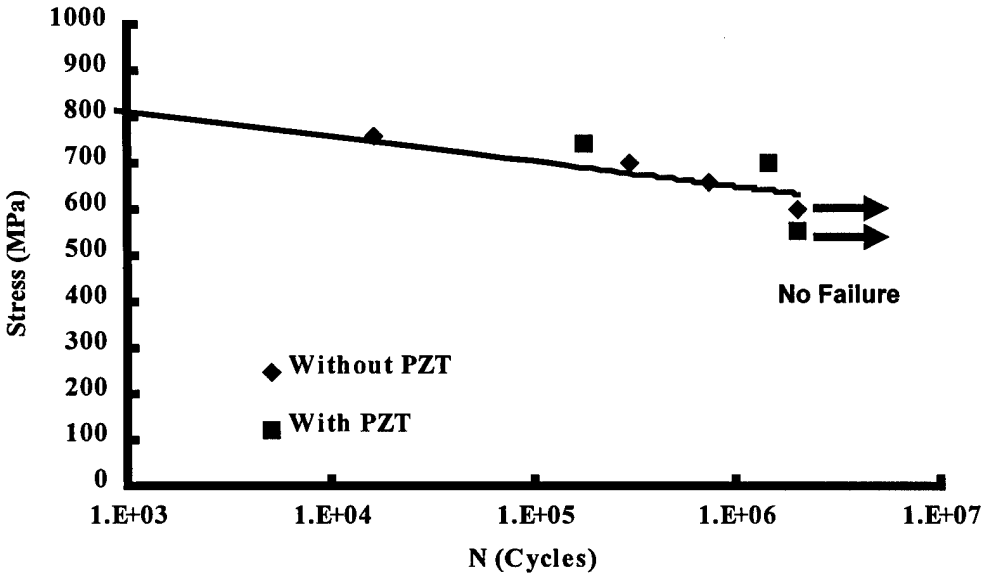

Figure 48. S-N Curve Magnified

4.2.2.2 Damage mechanisms

The damage mechanism for both MF and MAF specimens was similar to the monotonically loaded specimens, but the extent of overall damage was much more during fatigue. In the monotonic tests, the load was constantly increased to failure, so the progression of damage was dependent on the increasing level of applied stress. In the fatigue tests, the progression of damage was dependent on both the applied stress and the number of cycles. Since the applied fatigue stresses were above the measured static delamination stress level, different types of damage occurred almost simultaneously, then steadily increased thereafter.

In general, MF and MAF specimens failed in a similar manner. It was observed that the primary failure mechanism for both MF and MAF specimens under tension-tension fatigue loading were initially a combination of the development of matrix cracks in both the 90° and ±45° plies and then coalescence of these cracks along plies which then caused delamination along the 90/90 and 90/0 plies. This transferred the load to the debonded fibers, which eventually caused fracture due to tensile overload. No cracking was found in the 0° plies before specimen fracture.

The results of the damage analysis of MF (without PZT) and MAF (with PZT) specimens showed similar trends with few differences. The main difference was the extent of delamination. Figures 49 and 50 show the typical failure patterns of MF and MAF specimens. From these figures, it can be seen that specimen MF2 had severe fiber debonding and delamination at the edge, while specimen MAF2 had relatively less delamination. These figures also indicated that extensive delamination, debonding,

and fiber breakage resulted in specimens fracture. Note the fiber failure at the opposite end of the failure region. It looked like compressive loading caused the 0° ply fibers to buckle at this region. This indicates that, as the edge started to fail at the one end of the specimen, the bending moment generated compressive damage at the opposite end. A magnified picture of the fiber breakage area is shown in Figure 51. Specimen MAF2, which was tested at 740 MPa, had clearly more compressive damage and severe fiber breakage area than specimen MAF1, which was tested at 700 MPa. This shows that the extent of the damage region was dependent on the applied stress.

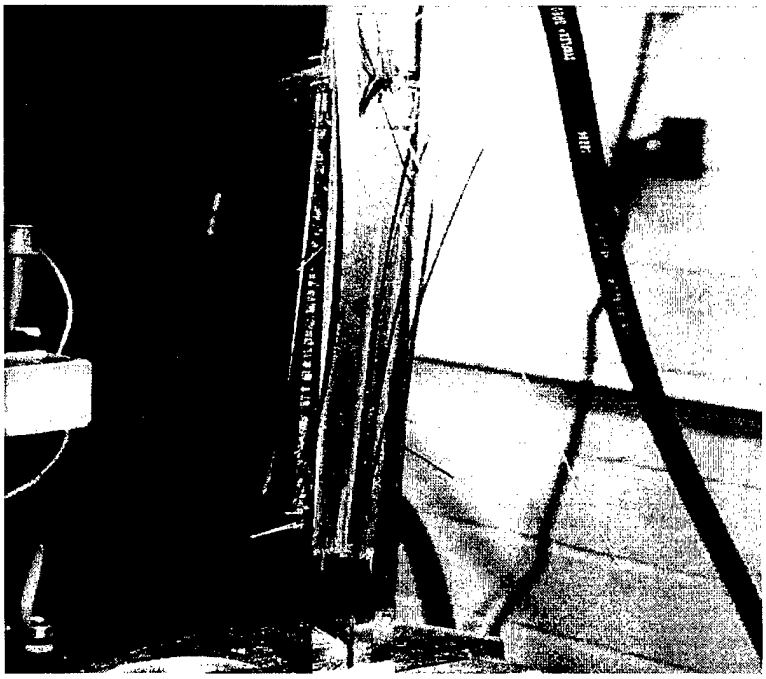

Figure 49. Specimen MF2 Failure under Tension-Tension Loading, $\sigma = 700$ MPa

In some tests, a few slices of 0° lamina peeled from the surface on both sides of the specimen near the grips, as the tests continued for some time. As cycles increased, the extent of sliced area developed along the applied loading direction from one end to the

Figure 50. Specimen MAF2 Failure under Tension-Tension Loading, $\sigma = 740$ MPa

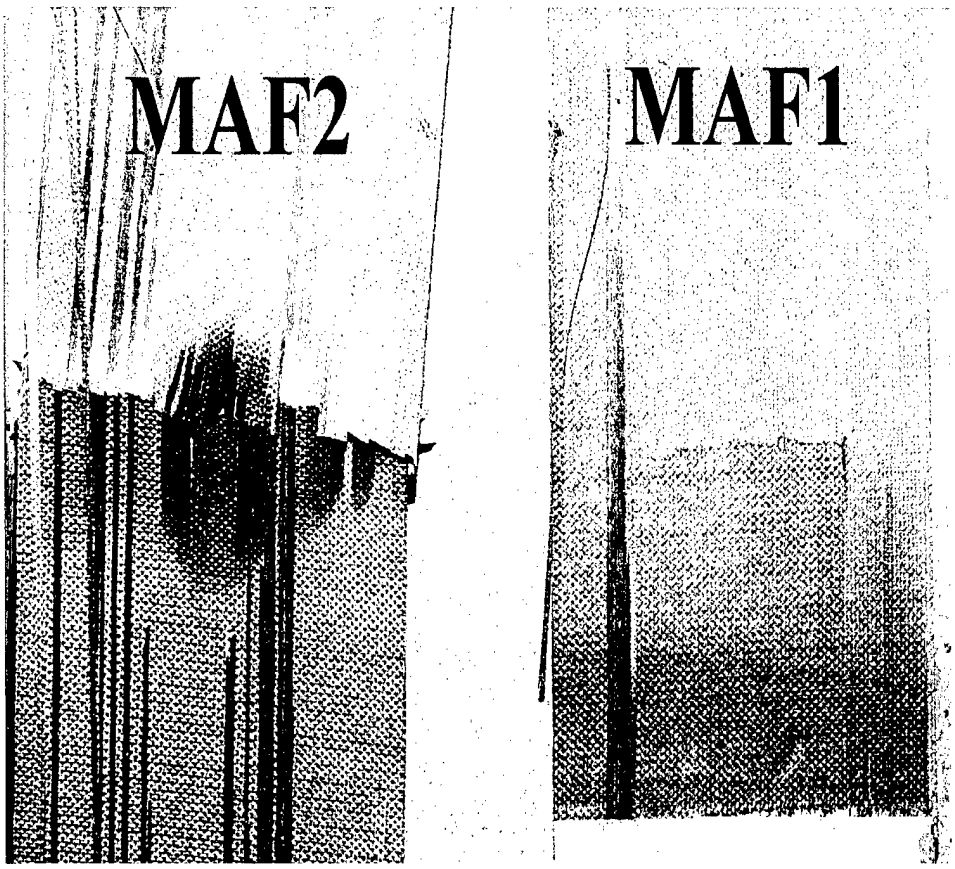

Figure 51. Fiber Breakage Area in MAF Specimens

other end. Finally, some 0° lamina slices peeled from the specimen. Figure 52 shows the side view of specimen MF4 at 500 cycles. Figure 53 shows the slice developed along the loading direction of specimen MF4 at 5,000 cycles.

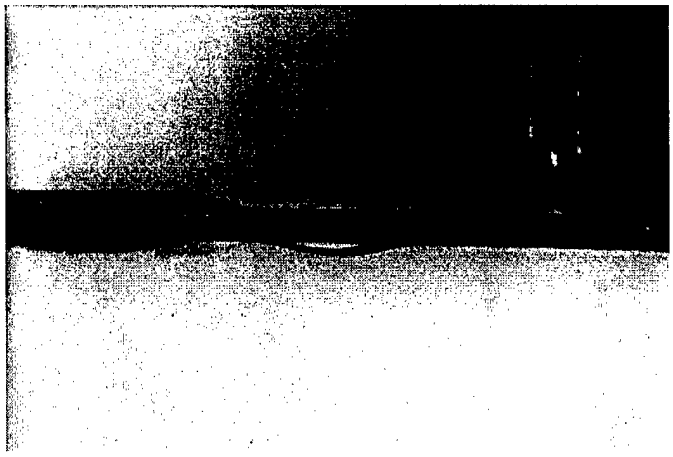

Figure 52. Side View of Specimen MF4 at 500 Cycles

4.2.2.3 Young's Modulus

One of the methods of assessing the damage progression is to look at the effective modulus in the laminate and how this modulus degrades during fatigue cycling. The procedure used for this is based on the relationship between the normalized modulus and fatigue life for MF and MAF specimens. The normalized modulus is defined as the measured modulus during the fatigue test divided by the initial modulus of the fresh specimen. In the same way, the normalized cycle is the instantaneous cycles divided by the fatigue life.

Theoretically, the higher stress test results in a greater reduction in modulus, and,on the other hand, the modulus should degrade more slowly under lower stress levels. These phenomena were seen on both MF and MAF specimens. Figure 54 shows the

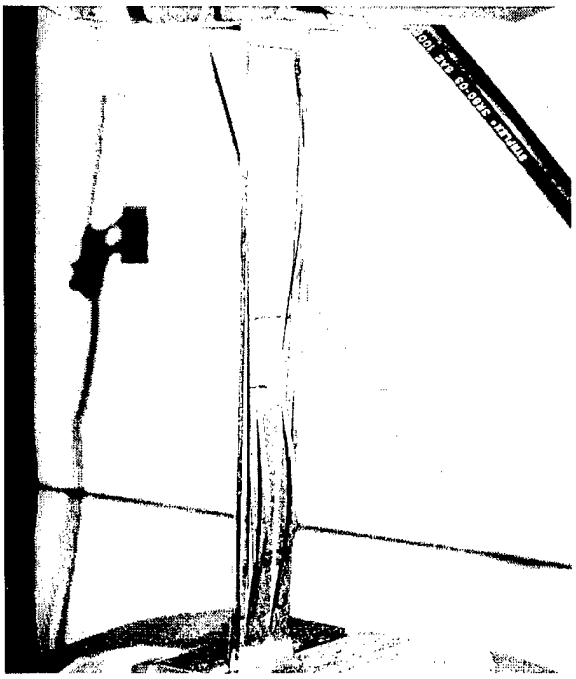

Figure 53. Specimen MF4 at 5,000 cycles

normalized modulus degradation of the MF group. This figure shows that, for most of the tests, the modulus dropped approximately 4 % during the first five thousand cycles, which may indicate 90° plies failure. After ten thousand cycles, the rate of degradation in modulus seems to depend on the stress at which the test was conducted. As expected, higher test stress caused larger drops. Specimen MF1, tested at the highest stress of 760 MPa, had a reduction in modulus of about 40 % after five thousand cycles, and failed after only 16,383 cycles. This would indicate that, after five thousand cycles, a large portion of the load was being supported by the 0° plies, and there was no further fatigue damage before final failure was reached. Figure 55 shows the normalized modulus versus the normalized cycles to failure relationship.

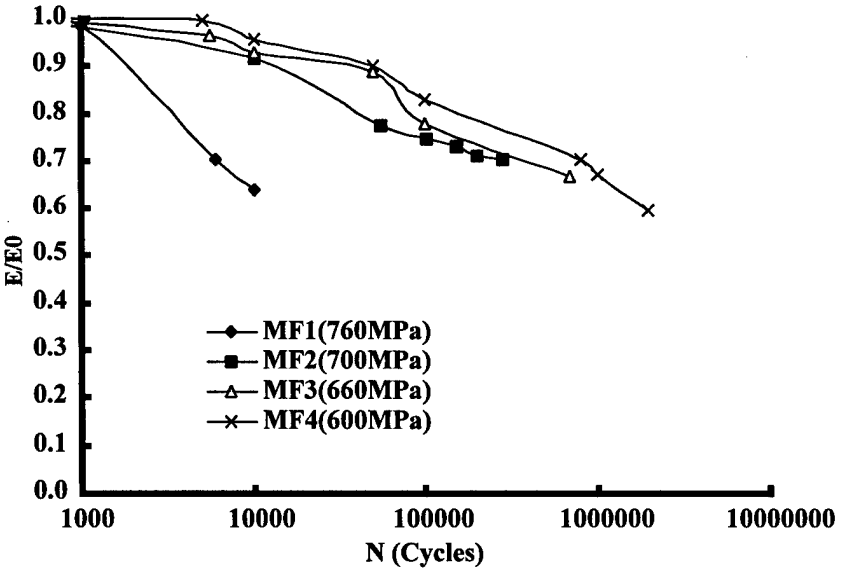

Figure 54. Normalized Modulus vs Cycles - MF Specimens

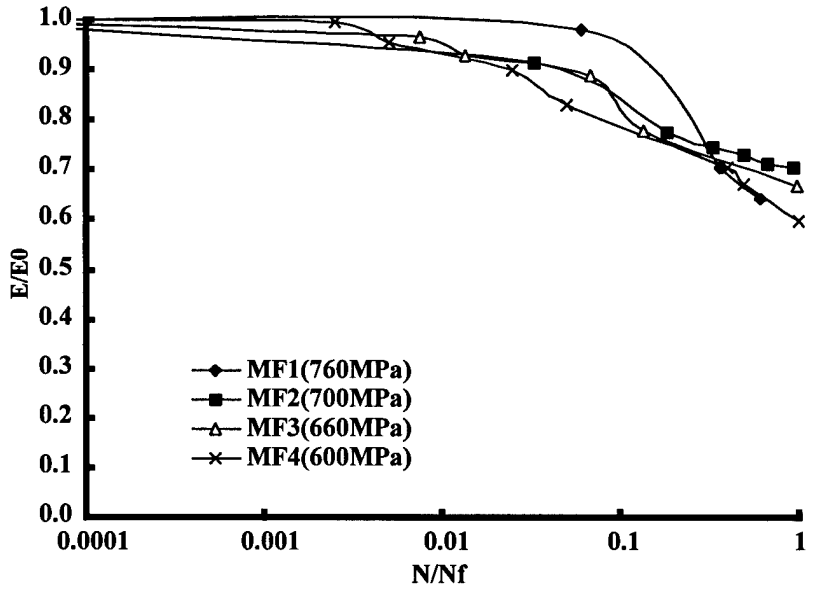

Figure 55. Normalized Modulus vs Normalized Cycles - MF Specimens

The trend of modulus degradation of MAF specimens were similar to MF specimens up to first 5,000 cycles, but dropped sharply during the later part of their fatigue life. Figure 56 shows the modulus degradation of the MAF group. As in MF specimens, the modulus dropped by 4 % when 5,000 cycles was reached, where the 90° plied failed. Figure 57 shows the normalized modulus versus the normalized cycles to failure relationship. Again, it can be seen here that, the higher loaded specimen has a higher rate of fatigue damage. Specimen MAF2 was tested at a maximum stress of 740 MPa and only had a fatigue life of 180,881 cycles, which is much less than MAF1 (tested at 700 MPa).

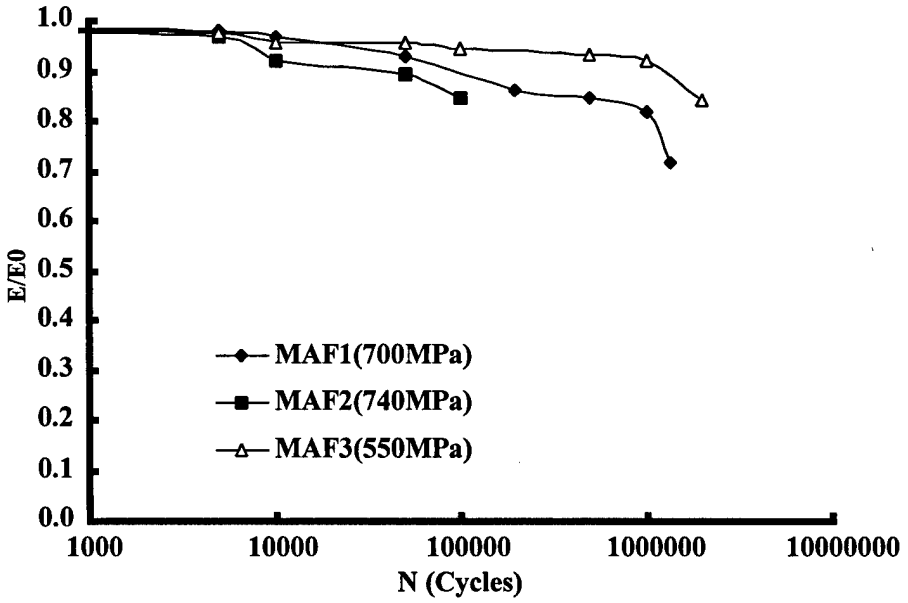

Figure 56. Normalized Modulus vs Cycles - MAF Specimens

Overall, both MF and MAF specimens' modulus degraded with fatigue life, but the shape of the progression curves were different. It can be seen in Figure 58 that,

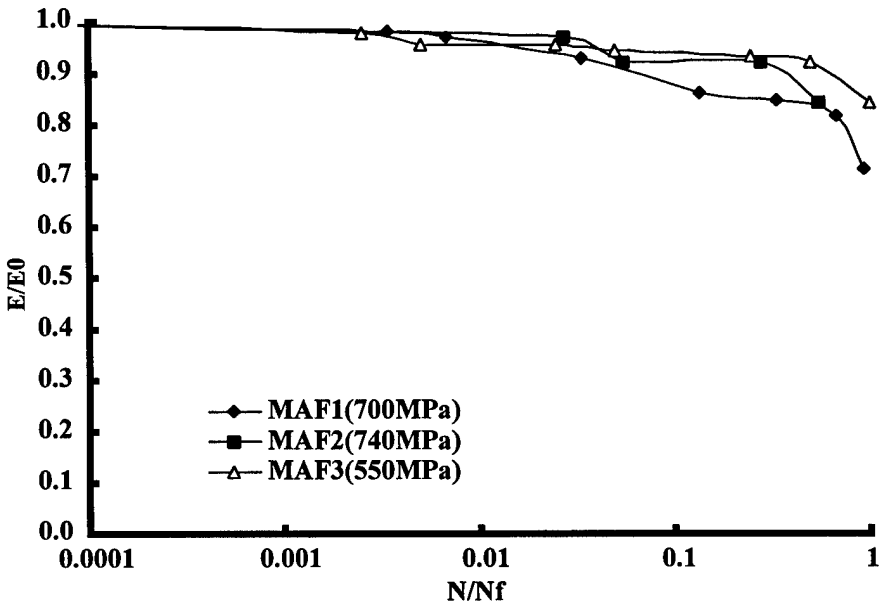

Figure 57. Normalized Modulus vs Normalized Cycles - MAF Specimens

for a given stress level, the specimens without PZT have greater modulus degradation than the specimens embedded with PZT, especially at the later part of their fatigue life. Specimen MF2 and MAF1, whose data are connected by solid lines, conducted at the same stress level 700 MPa, were within 5 % of modulus degradation of each other at the beginning of the test. But the range increased to 15 % at the later part of their fatigue life.

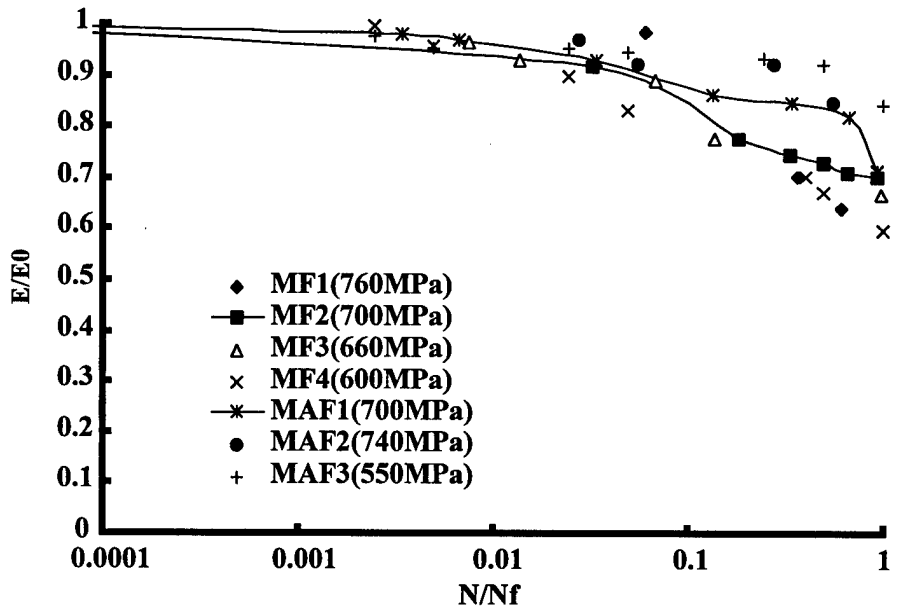

Figure 58. Normalized Modulus vs Normalized Cycles - All Specimens

4.2.2.4 Width of Delamination

The width of delamination was measured to monitor the progression of the edge effects in both MF and MAF specimens. The delamination growth rate was very similar for these two groups. Before 500 cycles was reached for every specimen, delamination occurred at the edge and extended almost instantly over the entire length of the speci-

men. Cracks could also be found at this time. As the cycles increased, the delamination grew continuously towards the center of the specimen from both free edges, and the width of the delamination also steadily increased. Since delamination may result from discontinuities in the laminate, it was found that delamination occurred between 90/90 and 90/0 interfaces. The change of the delamination interfaces usually happened at the transverse crack tips. Figures 59, 60, and 61 show the progression of delamination in MAF1.

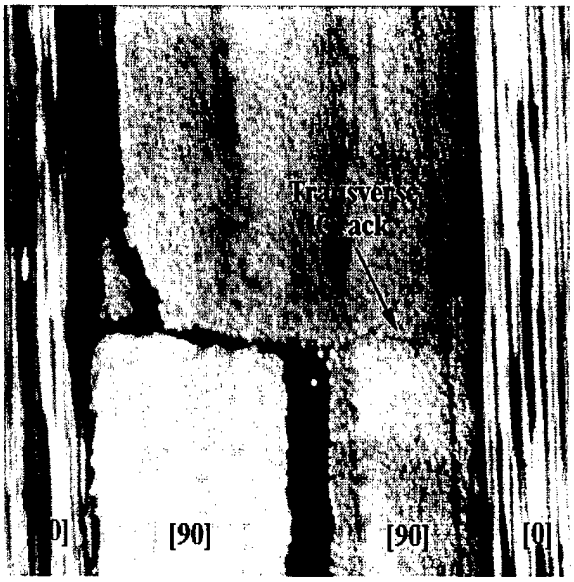

Figure 59. Delamination at Cycle 500 - Specimen MAF1

Figure 62 shows the delamination width of MF specimens versus fatigue life at different stress levels. As expected, the higher applied stress resulted in a higher rate of delamination. At the beginning of the tests, specimen MF3, which was loaded at 660 MPa, had a smaller rate of delamination than specimen MF2, which was loaded at 700 MPa. However, after 8,000 cycles, delamination of MF3 exceeded that of MF2.

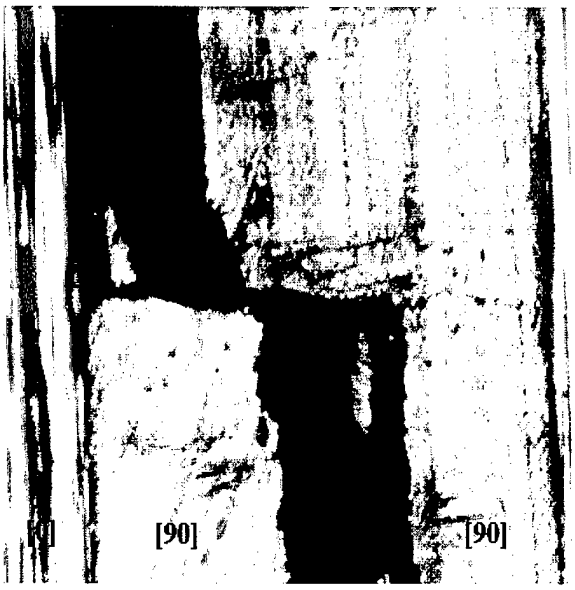

Figure 60. Delamination at Cycle 1K - Specimen MAF1

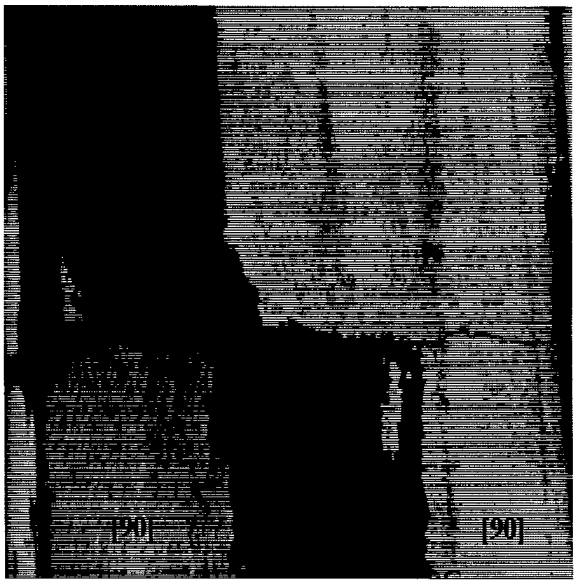

Figure 61. Delamination at Cycle 1000k - Specimen MAF1

This might be attributed to the natural variation in each specimen's material properties. The width of delamination trends found in the MAF specimens were similar to MF specimens. Figure 63 shows the delamination width of MAF specimens versus fatigue life at different stress levels. Again, it can be seen here that higher applied stress resulted in a larger rate of delamination. Specimens MAF1 and MAF2 both has almost the same width of delamination at the beginning of the tests, but the sizes increased to 23 mm and 27 mm, respectively, in the later part of their fatigue life.

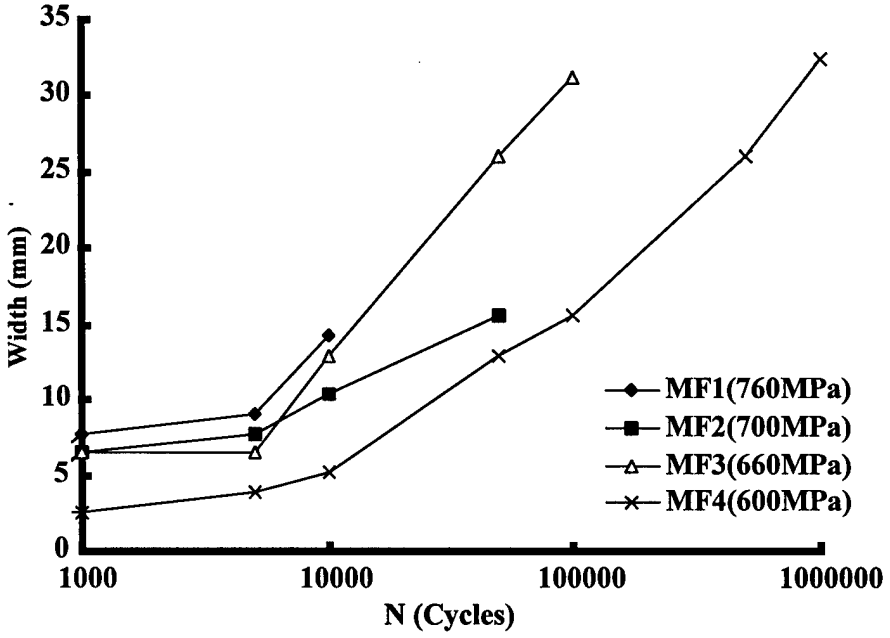

Figure 62. Width of Delamination vs Cycles - MF Specimens

Overall, the result of the delamination analysis of MF and MAF specimens showed similar trends with no significant difference, as depicted in Figure 64. However, MAF specimens have a smaller rate of delamination growth than MF specimens. For instance,

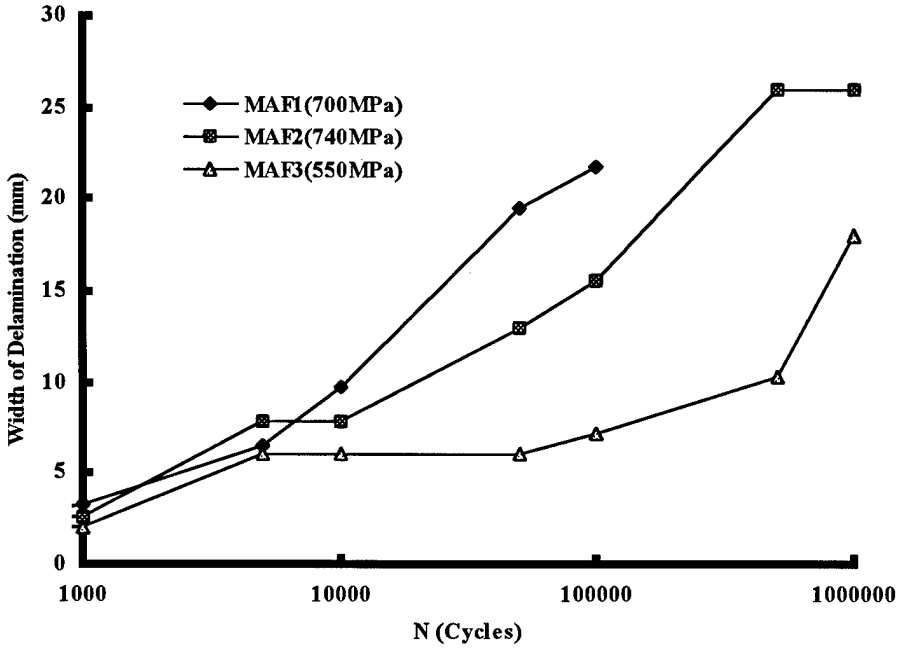

Figure 63. Width of Delamination vs Cycles - MAF Specimens

specimens MF1 and MAF2 were loaded at 760 and 740 MPa respectively, but MF1 exhibited a higher rate of delamination than MAF2. Although the total extent of delamination of MAF2 was somewhat higher than MF1, it was attributed the longer fatigue life of MAF2. These all indicate that the embedded PZTs seemed to decrease the extent of delamination during fatigue tests. Even after specimens fracture, MAF specimens still have less delamination than MF specimens as shown in Figure 65 and 66.

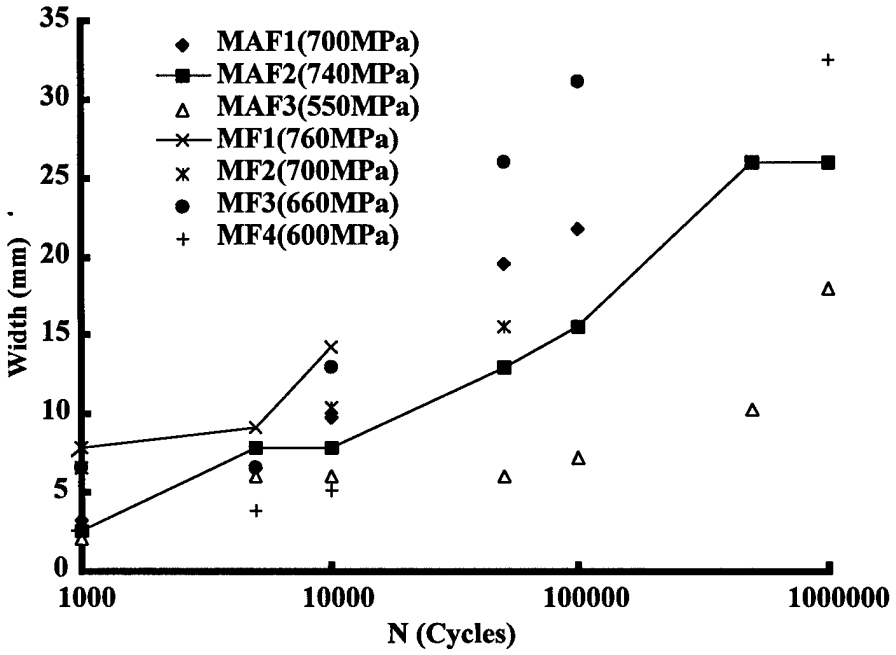

Figure 64. Width of Delamination vs Cycles - All Specimens

4.2.3 Comparison

Coleman studied the fatigue behavior of the same material as conducted in this study; quasi-isotropic, graphite/epoxy laminate, embedded with piezoelectric sensor but with a different lay-up, $[0/+45/-45/90]_S$ [4]. The results from Coleman's study showed

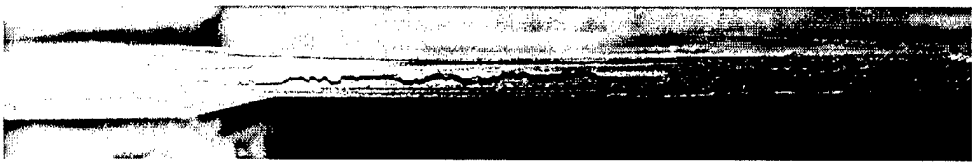

Figure 65. Side View of Failed Specimen MAF1

Figure 66. Side View of Failed Specimen MF3

that the embedded PZT did not reduce the the tensile strength or fatigue life of the host laminate. From the fatigue test results of this study, similar behavior was seen. In fact, at the same applied stress level, specimens with PZT have a longer fatigue life than specimens without PZT. The trends of modulus degradation rate were comparable for these two lay-ups. A sharper drop-off of the modulus occurred at the later part of fatigue life for embedded PZT specimens. While the results of the damage analysis of two laminates showed similar trends, one noticeable difference in failure mode behavior was found. No failed specimens with PZT spilt into two halves in $[0/0/+45/-45/0/0/90]_S$ laminate, but this behavior was seen in the $[0/+45/-45/90]_S$ laminate. This difference could be attributed to the type of laminate and properties of the structure as well.

Figure 67 shows S-N curves of $[0/0/+45/-45/0/0/90]_S$ and $[0/+45/-45/90]_S$ laminates. Figure 68 shows the relationship between normalized stress and cycles for these two lay-ups. It can be seen that all data points in normalized S-N curve scatter in a narrow band between two closer slope curves for these two laminates. This results also indicate that these two lay-up are fiber dominated.

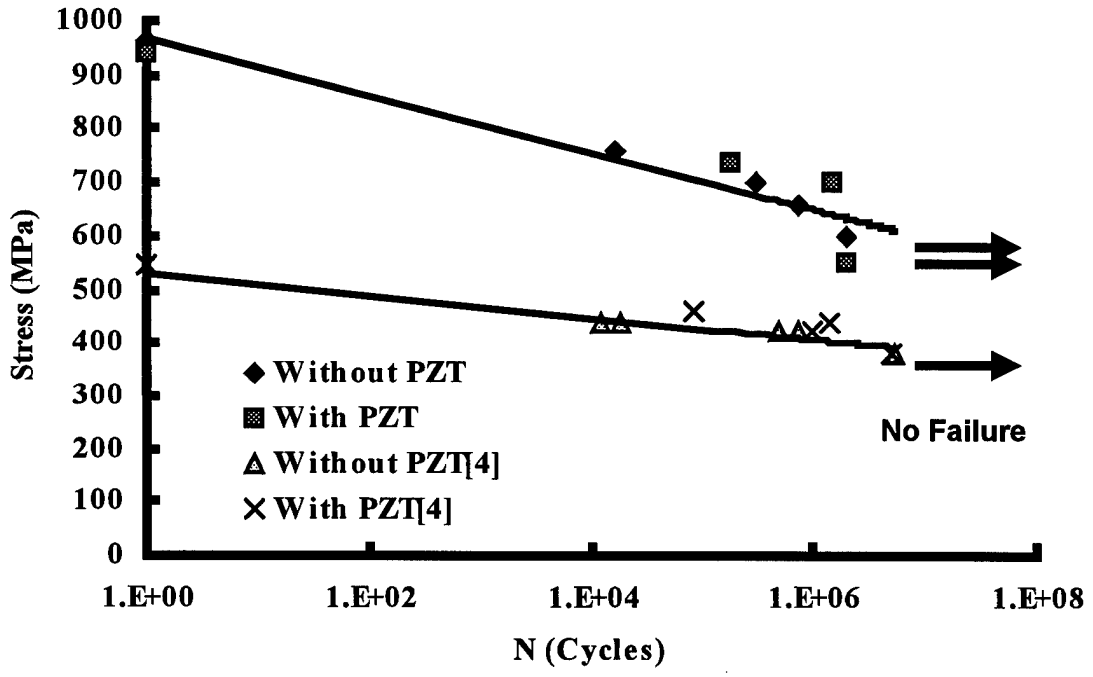

Figure 67. S-N Curves - Current Work and Coleman [4]

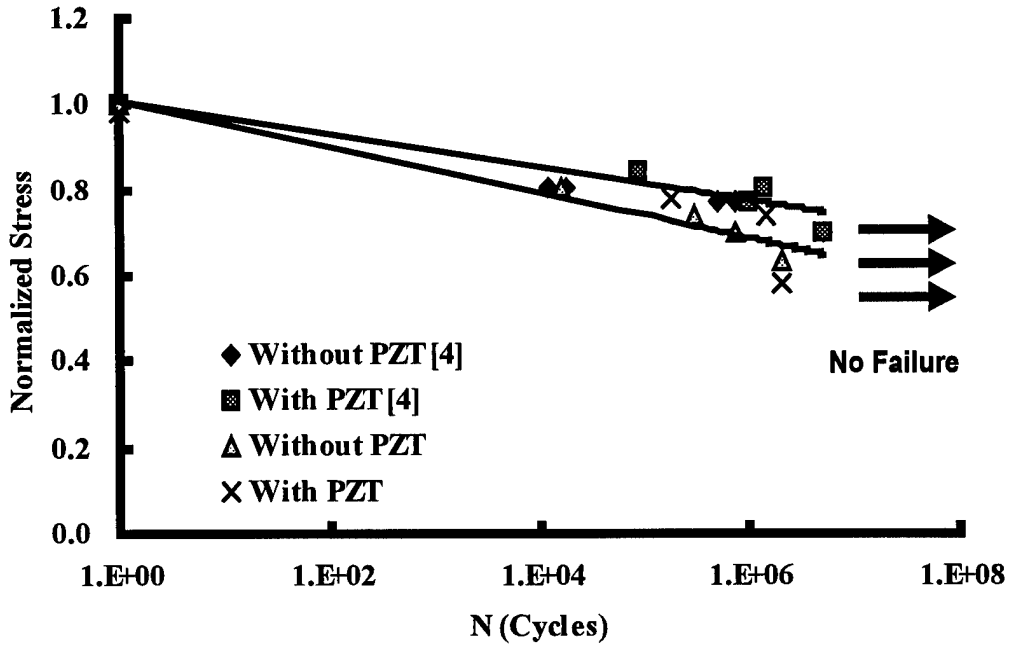

Figure 68. Normalized Stress vs Cycles - Current Work and Coleman [4]

5. Conclusions and Recommendations

Results from the electro-mechanical fatigue tests showed that the PZTs performed very well for out-of-phase and low stress conditions within the strain operating range of the PZT. Below the PZT's operating range, electrical depolarization caused by negative voltage excitation was the only factor to affect the performance of the actuator. Above the upper strain limit of PZT, the voltage output of the PZT was primarily influenced by the mechanical loading. As the maximum stress increased, the mechanical loading caused more piezoelectric damage in the actuators. Finally, the actuators failed after only 10,000 cycles at 100 MPa in the out-of-phase and low stress loading tests. No cracking and any other damage was found throughout all testings. Ultrasonic inspection was also used on two specimens, and it showed no damage. Strain gage data also showed no unusual signals during testing. Capacitance measurements were no help in discerning the health of the PZTs.

Results from the monotonic tests showed that the average ultimate strength and modulus of specimens with or without PZTs were within 2 % of each other, which was not very significant considering the relatively large size of the embedded PZT. Fatigue test results at high stress levels indicated no significant degradation to the laminate due to the embedded PZT. S-N curves for both types of specimens, with and without PZTs, indicated that the fatigue strengths were very similar. Actually, specimens with PZTs embedded inside the laminate had slight better fatigue life. Compared to MF specimens (without PZT), the trend of modulus degradation of MAF specimens (with PZT) had a sharper drop at the later part of the fatigue life, but the overall range in modulus reduction

for MF and MAF specimens were within 5-15 % of each other for fatigue loading. The rate of delamination growth of MF and MAF specimens during most of the fatigue life was also comparable to each other, with no significant variation.

This study investigated fatigue behavior of embedded actuators within and up to twice the operating strain range. Further research should investigate the electro-mechanical response of actuators as the electrical loading increases to $\pm 200\ V$, which is twice the operating voltage range suggested by the manufacturer.

APPENDIX A Material Properties of Laminates

A.1 Material Properties of AS4-3501-6

Property	Value
Longitudinal Modulus of Elasticity (E_1)	137.9 GPa
Transverse Modulus of Elasticity (E_2)	10.3 GPa
Shear Modulus (G_{12})	5.5 GPa
Major Poisson's Ratio (ν_{12})	0.3
Minor Poisson's Ratio (ν_{21})	0.023
Tensile Strength in Longitudinal Direction (σ_{xult})	2,137.9 MPa
Tensile Strength in Transverse Direction (σ_{yult})	65.5 MPa
Shear Strength (τ_{xy})	93.1 MPa
Fiber Volume (V_f)	65 %
Ply Thickness	0.127 mm

A.2 Properties of $[0/\pm 45/90]s$ Laminate

Property	Value
$Q_{11} = \frac{E_1}{1-\nu_{12}*\nu_{21}}$	138.86 GPa
$Q_{22} = \frac{E_2}{1-\nu_{12}*\nu_{21}}$	10.37 GPa
$Q_{12} = \frac{\nu_{12}*E_2}{1-\nu_{12}*\nu_{21}}$	3.11 GPa
$Q_{66} = G_{12}$	5.50 GPa
$Q_{xx}(\theta = 0) = Q_{11}$	138.86 GPa
$Q_{xx}(\theta = 90) = Q_{22}$	10.37 GPa
$Q_{xx}(\theta = 45) = \frac{1}{4} * (Q_{11} + Q_{12} + 2 * Q_{12} + 4 * Q_{66})$	44.36 GPa
$A_{xx} = \frac{t}{8} * (3 * Q_{11} + 3 * Q_{22} * 2 * Q_{12} + 4 * Q_{66})$	60.44 MPa
$A_{yy} = A_{xx}$	60.44 MPa
$A_{xy} = \frac{t}{8} * (6 * Q_{12} + Q_{11} + Q_{22} - 4 * Q_{66})$	18.53 MPa
$\bar{E}_x = \frac{1}{t} * (A_{xx} - \frac{(A_{xy})^2}{A_{xx}})$	53.90 GPa

A.3 Properties of $[0/0/\pm 45/0/0/90]s$ Laminate

Property	Value
$Q_{11} = \frac{E_1}{1-\nu_{12}*\nu_{21}}$	138.86 GPa
$Q_{22} = \frac{E_2}{1-\nu_{12}*\nu_{21}}$	10.37 GPa
$Q_{12} = \frac{\nu_{12}*E_2}{1-\nu_{12}*\nu_{21}}$	3.11 GPa
$Q_{66} = G_{12}$	5.50 GPa
$Q_{xx}(\theta = 0) = Q_{11}$	138.86 GPa
$Q_{xx}(\theta = 90) = Q_{22}$	10.37 GPa
$Q_{xx}(\theta = 45) = \frac{1}{4} * (Q_{11} + Q_{12} + 2 * Q_{12} + 4 * Q_{66})$	44.36 GPa
$A_{xx} = \frac{t}{8} * (3 * Q_{11} + 3 * Q_{22} * 2 * Q_{12} + 4 * Q_{66})$	166.30 MPa
$A_{yy} = A_{xx}$	166.30 MPa
$A_{xy} = \frac{t}{8} * (6 * Q_{12} + Q_{11} + Q_{22} - 4 * Q_{66})$	20.90 MPa
$\bar{E}_x = \frac{1}{t} * (A_{xx} - \frac{(A_{xy})^2}{A_{xx}})$	92.03 GPa

APPENDIX B Hysteresis Loop Formation

This Appendix contains several plots show how the hysteresis loop form a closed loop and the change in voltage before and after repoling.

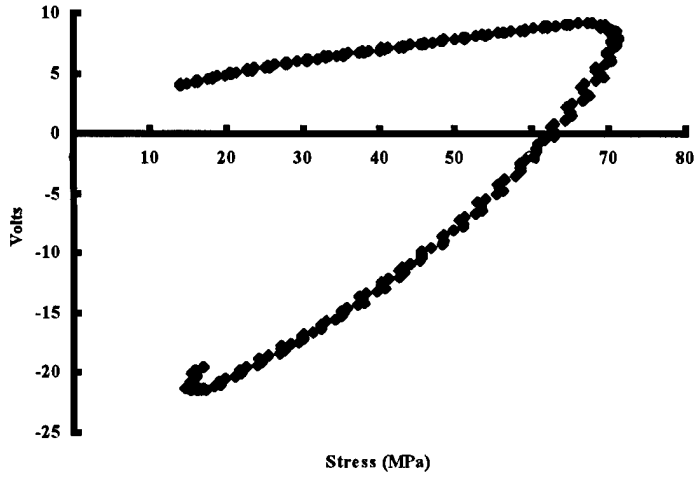

Figure 69. Stress vs Voltage Loop - Cycle 1, $\sigma = 75MPa$ (Before Repoling)

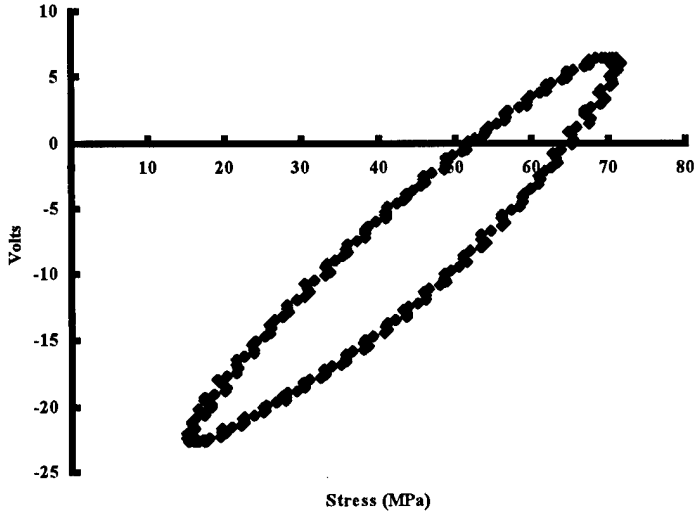

Figure 70. Stress vs Voltage Loop - Cycle 6, $\sigma = 75MPa$ (Before Repoling)

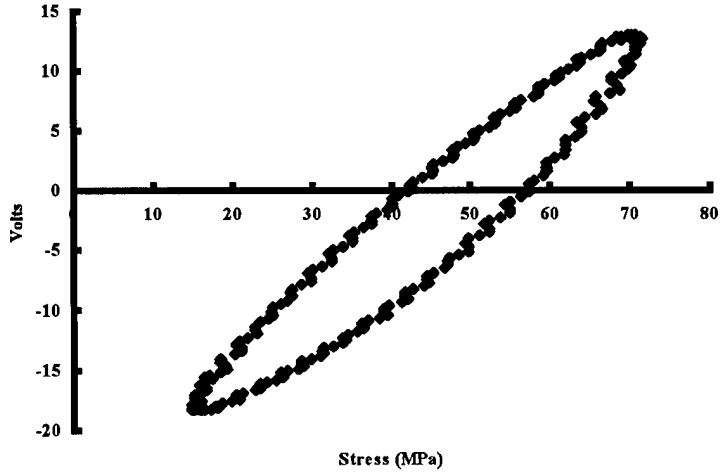

Figure 71. Stress vs Voltage Loop - Cycle 11, $\sigma = 75MPa$ (Before Repoling)

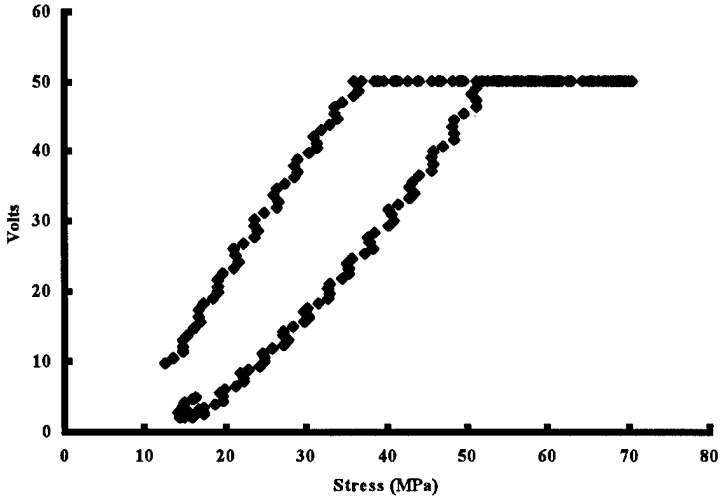

Figure 72. Stress vs Voltage Loop - Cycle 1, $\sigma = 75MPa$ (After Repoling)

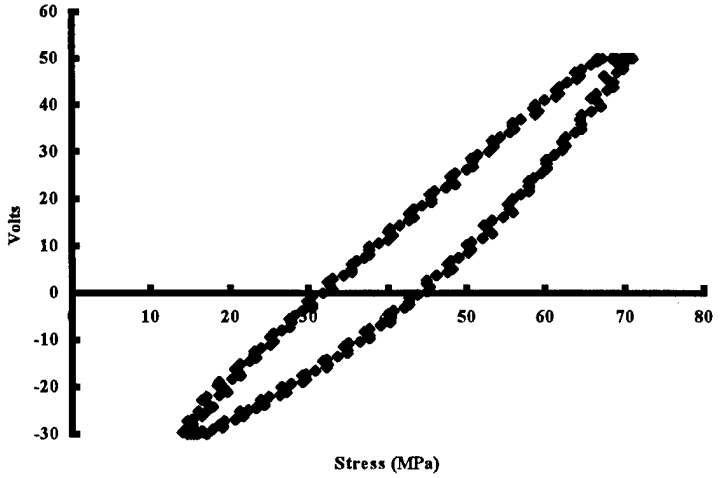

Figure 73. Stress vs Voltage Loop - Cycle 6, $\sigma = 75MPa$ (After Repoling)

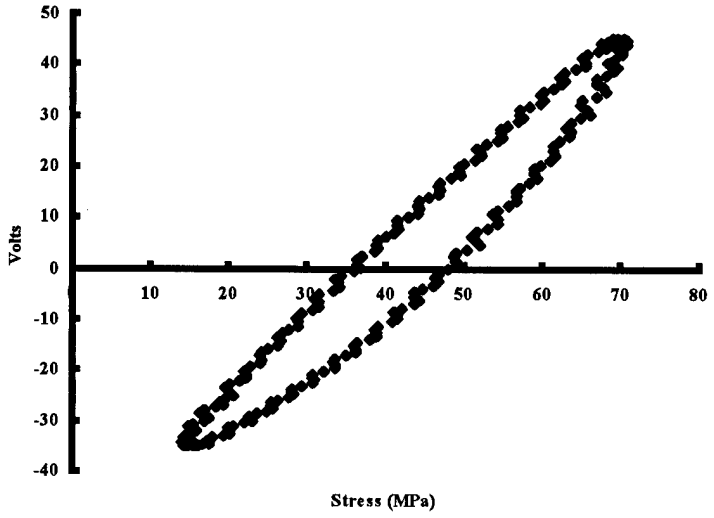

Figure 74. Stress vs Voltage Loop - Cycle 11, $\sigma = 75MPa$ (After Repoling)

Bibliography

[1] ACX. General Specifications: *Model QP15N.* Active Control eXperts, Inc., 1995.

[2] D. Brei. Piezoelectrics I and II, ME 599, Smart Materials and Structures Class Notes, University of Michigan, 1996.

[3] D. Brei. Smart Structures. Technical Report F33615-94-C-5804, University of Michigan, 1996.

[4] J. M. Coleman. Fatigue behavior of a quasi-isotropic graphite/epoxy laminate embedded with a piezoelectric sensor. MS thesis, AFIT, 1997.

[5] B. Culshaw. *Smart Structures and Materials.* Artech House, Inc., 685 Canton Street, Norwood, MA 02062, 1996.

[6] I. M. Daniel. and O. Ishai. *Engineering Mechanics of Composite Materials.* Oxford University Press, 200 Madison Avenue, New York, New York 10016, 1994.

[7] S. B. Dosedel. Influence of embedded optical fibers on compressive strength of advanced composites. MS thesis, AFIT, 1993.

[8] S. Green. Aspects of compression in aerospace composites-future requirement. Technical report, AGARD, 1991.

[9] J. P. Hansen and A.J. Vizzini. Fatigue response of a host structure with interlaced embedded devices. In *38th AIAA/ASME/ASCE/AHS/ASC Structures, Structural Dynamics and Materials Conference,* pages AIAA 97-1346, 1801 Alexander Bell Drive, Suite 500, Reston, VA, 20191, 1997. AIAA.

[10] Hercules. *Hercules Carbon Prepreg Tape AS43501-6 Product Data Sheet.* Hercules Advanced Materials and Systems Company, 1991.

[11] J. H. Jacobs. Synthesis and processing of intelligent cost effective structures (SPICES). Technical Report MDA972-93-2-0010, McDonnel Douglas Aerospace, 1996.

[12] K. L. Reifsnider. E. G. Henneke. W. W. Stinchcomb. and J. C. Duke. Damage mechanics and NDE of composite laminates, In *Mechanics of Composite Materials,* Recent Advances, Z. Hashin and C. T. Herakovich, eds., New York, pages 399-420, 1983. Pergamon Press

[13] R. Y. Kim. Fatigue strength of composite structures, University of Dayton Research Institute. 1986.

[14] C. S. Lynch. The effect of uniaxial stress on the electro-mechanical response of 8/65/35 PLZT, 1995. Department of Mechanical Engineering, University of California, Santa Barbara, CA, 93106. Submitted to the Acta Metallurgica et Materialia.

[15] C. S. Lynch. Electro-mechanical constitutive behavior of various compositions of PZT and PLZT, 1995. Department of Mechanical Engineering, University of California, Santa Barbara, CA, 93106. Submitted to the 1995 North Amercian of Conference on Smart Structures and Materials.

[16] D. R. Shukla. and A. J. Vizzini. Interlacing for improved performance of laminates with embedded devices. In *Smart Materials and Structures 5,* pages 225-229, Printed in the UK, 1996. AIAA.

[17] D. A. Singh. and A. J. Vizzini. Structural integrity of composite laminates with interlaced actuators. In *Smart Materials and Structures 3,* pages 71-79. Printed in the UK, 1994. AIAA.

[18] P. N. Sreeram. and N. G. Naganathan. Hysteresis prediction for piezoceramic actuator systems using Preisach models, Volume 2189, pages14-21, SPIE, 1994.

[19] C. T. Sun. and L. Z. Jiang. Fatigue behavior of piezoelectric ceramics. Volume 3040, pages129-135, SPIE, 1997.

[20] R. Talreja. Damage mechanisms and fatigue-life diagrams. A378, pages 461-475, Proc. Royal Soceity, 1981.

Vita

Major Tse-Lin Hsu was born 25 November 1967 in Tao-Yuan, Taiwan, Republic of China. He graduated from Tse-Hsiu High School, Taipei county, Taiwan in 1985. He then attended the Chung-Chang Institute of Technology (CCIT) from 1985 through 1989 and graduated with a Bachelor of Science Degree in Mechanical Engineering. He was commissioned in the Army and was assigned to the Chung-Shan Institute of Science and Technology (CSIST) in June of 1989. In CSIST, he was serviced in the Missile & Rocket Systems Research Division as a staff officer for seven years. During the time in CSIST, he received a medal for his excellent performance. He entered the School of Engineering, Air Force Institute of Technology, in September of 1996.

REPORT DOCUMENTATION PAGE	Form Approved OMB No. 0704-0188

1. AGENCY USE ONLY *(Leave blank)*	2. REPORT DATE	3. REPORT TYPE AND DATES COVERED
	September 1998	Master's Thesis

4. TITLE AND SUBTITLE
Electro-Mechanical Fatigue Behavior of a Quasi-Isotropic Laminate with an Embedded Piezoelectric Actuator

5. FUNDING NUMBERS

6. AUTHOR(S)
Tse-Lin Hsu, Major, ROCA

7. PERFORMING ORGANIZATION NAME(S) AND ADDRESS(ES)
Air Force Institute of Technology
2750 P Street
WPAFB

8. PERFORMING ORGANIZATION REPORT NUMBER
AFIT/GAE/ENY/98S-02

9. SPONSORING/MONITORING AGENCY NAME(S) AND ADDRESS(ES)
Major Brian Sanders
AFOSR
110 Duncan Avenue, Suite B
Bolling AFB, DC 20332-001

10. SPONSORING/MONITORING AGENCY REPORT NUMBER

11. SUPPLEMENTARY NOTES
Advisor : Dr. Shankar Mall
Tel : (937) 255-3636 ext 4587; E-mail : small@afit.af.mil

12a. DISTRIBUTION AVAILABILITY STATEMENT
Approved for public release; distribution unlimited

12b. DISTRIBUTION CODE
A

13. ABSTRACT *(Maximum 200 words)*

This study primarily investigated the electro-mechanical fatigue behavior of the embedded piezoelectric actuators in graphite/epoxy laminate with a lay-up of $[0|\pm45|90]s$. A secondary focus was the investigation of the mechanical fatigue effects of the $[0|0|\pm45|0|0|90]s$ laminate with embedded PZT under tensile loading. All the fatigue tests were conducted with a triangular loading waveform which had a frequency of 10 Hz and with $R=0.1$. In the electro-mechanical testing, the embedded actuator was excited by a -10 V to -100 V or a 10 V to 100 V voltage input, which resulted in either in-phase or out-of-phase electrically induced strain waveform with respect to the mechanical loading or strain. It was found that the embedded PZTs performed very well during the out-of-phase electro-mechanical and low stress fatigue conditions when the applied strain was within the operating range of PZT. Beyond the upper strain limit, the voltage output of the PZT was primarily influenced by the mechanical fatigue loading. Results from the high stress fatigue tests showed that the embedded piezoelectric actuators did not have significant effect on the tensile strength of the laminates.

14. SUBJECT TERMS
Graphite/epoxy Composite, Out-of-Phase, In-Phase, Fatigue, Quasi-Isotropic, Smart Materials, Piezoelectric, Embedded Actuators

15. NUMBER OF PAGES
131

16. PRICE CODE

17. SECURITY CLASSIFICATION OF REPORT	18. SECURITY CLASSIFICATION OF THIS PAGE	19. SECURITY CLASSIFICATION OF ABSTRACT	20. LIMITATION OF ABSTRACT
Unclassified	Unclassified	Unclassified	UL